Non-linear interoperability and optimal energy management study for energy storage systems used in residential AC nanogrids

by

Andres C Salazar Llinas

(Under the Direction of Javad Mohammadpour-Velni)

Abstract

Residential energy storage (RES) installations have exponentially increased over the last years in the United States. The cluster of residential battery storage plus solar is also known as distributed nanogrids. Although fundamentally similar to conventional large-scale microgrids, residential nanogrids offer the possibility of a widely distributed energy generation and, at the same time, allow the end-user to be ready against externalities that could cause the electric system suspension for weeks or months. Output power and energy storage scalability, battery prognosis, and optimal energy management are among the main challenges these systems face. In most cases, the implementation of control and monitoring strategies at the power converter and energy management level addresses the challenges mentioned above. This research aims to study non-linear control schemes at different hierarchical levels of the energy storage systems (ESS) for the realization of AC residential nanogrids. This dissertation develops a time-varying phasor model for multiple ESS connected in parallel. The model considers the use of non-linear droop control and virtual impedance scheme in the power converters of the ESS. Contraction theory is then employed to analyze the stability of two systems connected in parallel. We also propose a non-intrusive method to estimate lithium-ion battery modules' internal impedance used in residential ESS. Such an approach considers the non-linear intrinsic power transfer characteristic in the DC/AC conversion process for single-phase systems. Such assessment also allows us to develop a non-linear control law for the DC/DC power converter using feedback linearization analysis. Finally, we formulate a non-linear optimization problem for the energy management of islanded residential nanogrids using stochastic dynamic programming. We corroborate and validate the proposed methods and control schemes using numerical analysis and experimental results throughout the dissertation.

INDEX WORDS: [Energy Storage, Nanogrids, Microgrids, Non-linear systems, Time-Varying phasor, Contraction theory, Battery impedance, Feedback linearization, Non-linear optimization, Markov process, Stochastic dynamic programming]

Non-linear interoperability and optimal energy management study for energy storage systems used in residential AC nanogrids

by

Andres C Salazar Llinas

M.S., University of Puerto Rico, 2011

A Dissertation Submitted to the Graduate Faculty of the
University of Georgia in Partial Fulfillment of the Requirements for the Degree

Doctor of Philosophy

Athens, Georgia

2021

Non-linear interoperability and optimal energy management study for energy storage systems used in residential AC nanogrids

by

Andres C Salazar Llinas

Major Professor: Javad Mohammadpour-Velni

Committee: Jin Ye

Wenzhan Song

Antonio Ginart

Electronic Version Approved:

Ron Walcott

Dean of the Graduate School

The University of Georgia

May 2021

Dedication

In memory of Lourdes Daza.

Acknowledgments

I want to thank to: God, for being the primary force that moves my life. My wife Awilda, for her support and comprehension. My son Adrian, who gave me another reason to fight for my dreams. My parents Nora and Jose, for their tenacity and and unconditional love. My brother Luis, for encouraging me always to continue and persevere. All my friends and family who had made possible my road until here.

Special thanks to my advisor Dr Javad Mohammadpour-Velni, for giving me the opportunity to work in his group. His guidance and support has been invaluable. My company sonnen for providing me the space and financial support to work on this research, especially to Carlos Restrepo, CTO sonnen Inc and Hermann Schweizer, CTO sonnen GmbH. All my team members especially Dr Alberto Berzoy for believing and supporting me on part of this research. And finally to the members of my committee, Dr Jin Ye, Dr Wenzhan Song and Dr Antonio Ginart. I highly appreciate their time and interest on this work.

Contents

List of Figures

List of Tables

Chapter 1

AC Residential Nanogrids

The ecosystem of distributed generation is generally divided into two main types, microgrids (MGs) and nanogrids (NGs) (Werth et al., 2015). MGs, which constitute various types of large-scale distributed energy resources (DERs) and energy storage systems (ESS) units connected to the mains, can supply power to load demands generally in the order of megawatts. NGs are typically composed of a single type of renewable energy systems (RES) such as photo-voltaic (PV) systems, an energy storage system (ESS), and a fuel/gas generator, with or without the capability to connect to the utility. Residential NGs are typically designed to serve a single building where maximum power levels are not greater than $10kW$. In case of a grid service interruption, the grid-tied inverter stops the power generation, and the RES, ESS, and the fuel generator form an autonomous NG.

This chapter will introduce the reader to the concepts of residential nanogrids, especially AC nanogrids, when they work as autonomous NGs or, as it is commonly known, island operation. It will also present the main challenges these systems face and the primary motivations for the proposed work.

1.1 ESS and Renewable role on Distributed Energy Generation

Centralized energy generation and distribution have been the electrical power system's status quo for more than 100 years. A typical example of a classic power system is shown in Fig. 1.1. Under this scheme, power generation plants (typically fossil fuel-based) generate electricity in locations that are, in most cases, far from the end consumer. Multiple high power plans are interconnected at the transmission level, and electricity normally flows in one direction, from generation to commercial, industrial, and residential loads. In par-

ticular, the electricity flowing through the distribution network is unidirectional (Q.-C. Zhong & Tomas, n.d.).

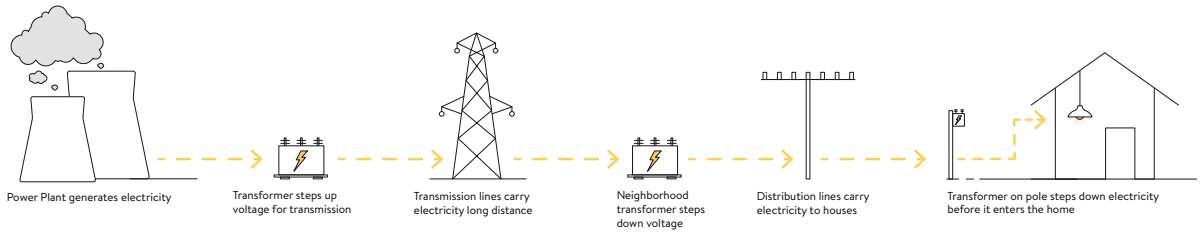

Figure 1.1: Typical Centralized Generation Power System

In the last two decades, there has been a strong interest in diversifying the energy generation portfolio by reexamining the role of renewable energy from the environmental point of view and the economic aspect. The focus on renewables has gained momentum recently. Such renewed focus, backed by the rapid development of more efficient and affordable technology, has created the right conditions for the industry to establish itself solidly (Administration, 2020). Therefore, alternative energy sources make it possible to change the power flow's typical unidirectionality, allowing power generation from the distribution system even at the residential level as it is shown in Fig.1.2. The creation and widespread implementation of microgrids (MGs), has helped in the evolution and modernization of the power system. Microgrids are small-scale power networks that are used to supply local loads in small geographical areas, facilitating the integration of renewable energy generators and the scalable addition of new generation systems and loads. Microgrids facilitate the reliable integration of renewable energy resources such as wind, solar generation, and fuel cells through distributed generators (DGs). The microgrid operates on the idea of autonomous subsystems composed of small local areas with dedicated control systems that provide guaranteed power quality support to the distribution grid. The microgrid concept potentially enables high DGs penetration without redesigning or re-engineering the distribution system itself (Bidram et al., 2017).

The acceptance of renewables into the generation mix has not been seamless and straightforward. In many instances, solar and wind generation are conceptually different from more conventional means of energy generation. For example, solar and wind plants are typically more distributed in nature than other plants, and their production performance is affected by the weather. Thus, the need to manage energy for practical use and stability has been an ongoing concern (Restrepo et al., 2015).

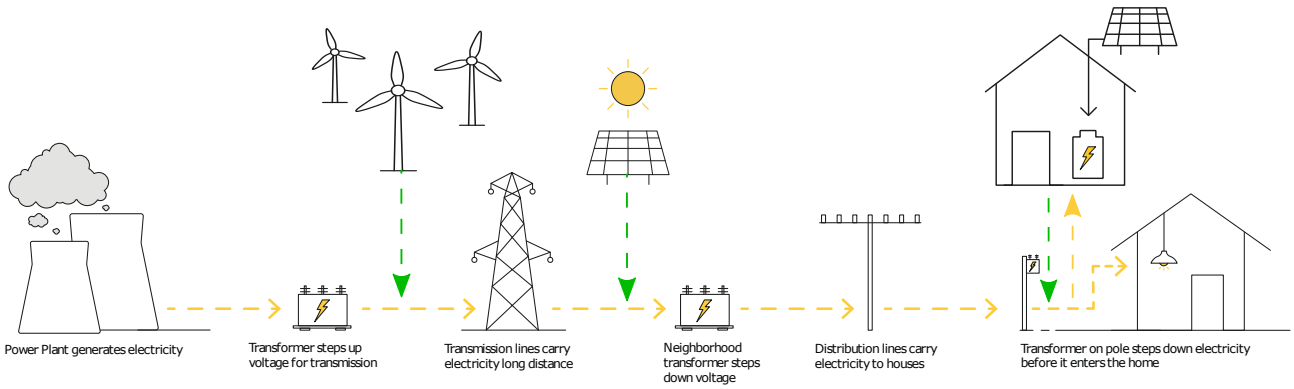

Figure 1.2: Distributed Generation Power System

The planning and forecasting of solar and wind production can be highly complicated, and, in some instances, it is not accurate enough. The susceptibility of solar and wind power generation to weather patterns in conjunction with expected demand can lead to solutions that may not be efficient and compliant to all applications. The use of energy storage together with photovoltaic (PV) and wind power generation offers a the ability to reduce the impact of variability in power generation significantly. Batteries played a principal role in the evolution of energy storage. Significant research effort has resulted in a more sophisticated knowledge of battery chemistry, which has consequently given a rapid reduction in cost while addressing major concerns about reliability and stability.

Such declining costs of battery storage technologies have stimulated interest in combining PV with batteries to provide dispatchable energy and reliable capacity—particularly as the U.S. utility storage market has begun moving away from short-term power regulation and longer-term temporal shifting of renewable generation. The significant power interruptions caused by natural disasters such as hurricanes, tornadoes, fires, among others, have also propelled the need to improve the reliability and resiliency of U.S. electric systems. The integration of renewable generation and battery storage offers a way to cost-effectively diversify and fortified the nation's energy portfolio (Fu. et al., 2018).

Distributed energy generation from homes and in neighborhood locations comes naturally as a reaction to the demand and low cost of the systems. Residential energy storage (RES) installations have dramatically increased in the U.S. over the last 3 years, going from less than 5MWh deployments in 2016 to a record of 40MWh in 2019 (see Fig. 1.3) (Mackenzie, 2020). And it is projected to go over 17 GW peak of battery storage capacity in 2050 (Administration, 2020). The cluster of residential battery storage plus solar is also known as distributed nanogrids. Although fundamentally similar to conventional large-scale microgrids,

residential nanogrids offer the possibility of a widely distributed energy generation and, at the same time, allow the end-user to be ready against externalities that could cause the electric system suspension for weeks or months. Besides, residential nanogrids support the PV self-consumption while reducing household electrical demand charges. It provides several grid-level benefits such as voltage and frequency regulation, deferred infrastructure investment, and resource adequacy (Ardani et al., 2016).

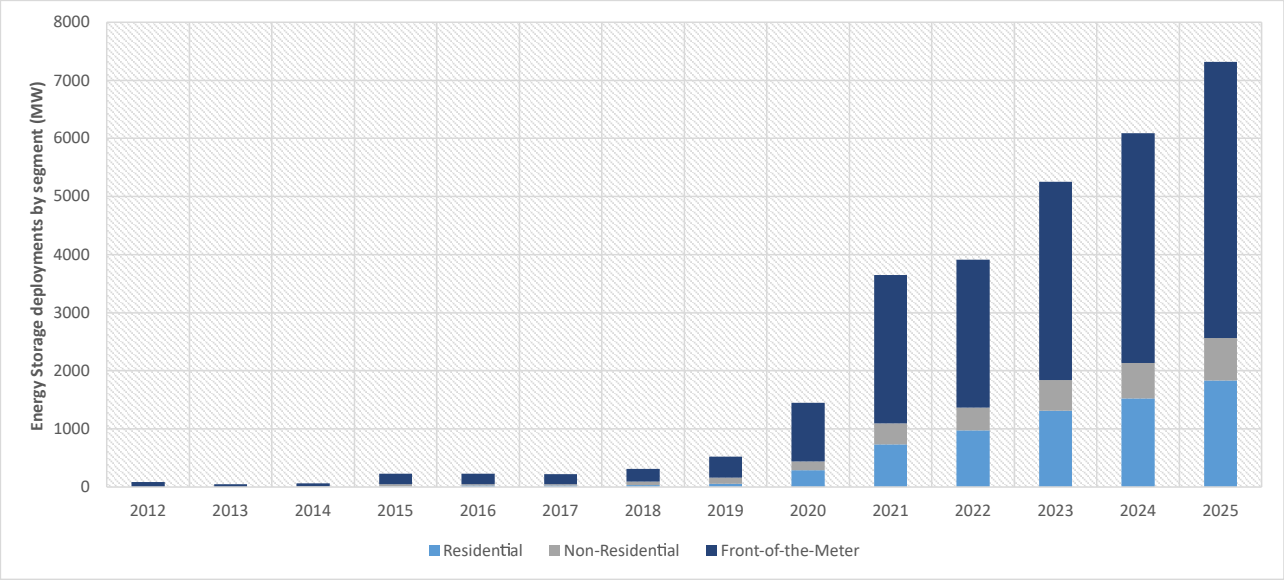

Figure 1.3: U.S. energy storage annual deployment forecast, 2012-2025E(MW). Adapted from (Mackenzie, 2020).

1.2 The Concept of Nanogrids

(Nordman et al., 2012) defines a nanogrid as a single domain for voltage, price, reliability, quality, and administration. The main components of a nanogrid are a controller, load, storage, and gateways. Figure 2.4 shows a scheme represent ion for a nanogrid. Although energy storage is optional, the addition of such an element provides the nanogrid with stability and continuous operation; it does, however, add complexity.

- Loads in a nanogrid could be or not (is not necessary) to be controlled in such a way that its power level could be either curtailed or reduced. For instance, LED lights can be dimmed out to reduce power consumption, or intelligent breakers can be used to restrict the power consumption from a specific load. Under this scenario, the nanogrid is known to be managed. If loads can not be controllable, then the nanogrid is unmanaged, i.e., there is no communication between loads and controller (Nordman & Christensen, 2013).

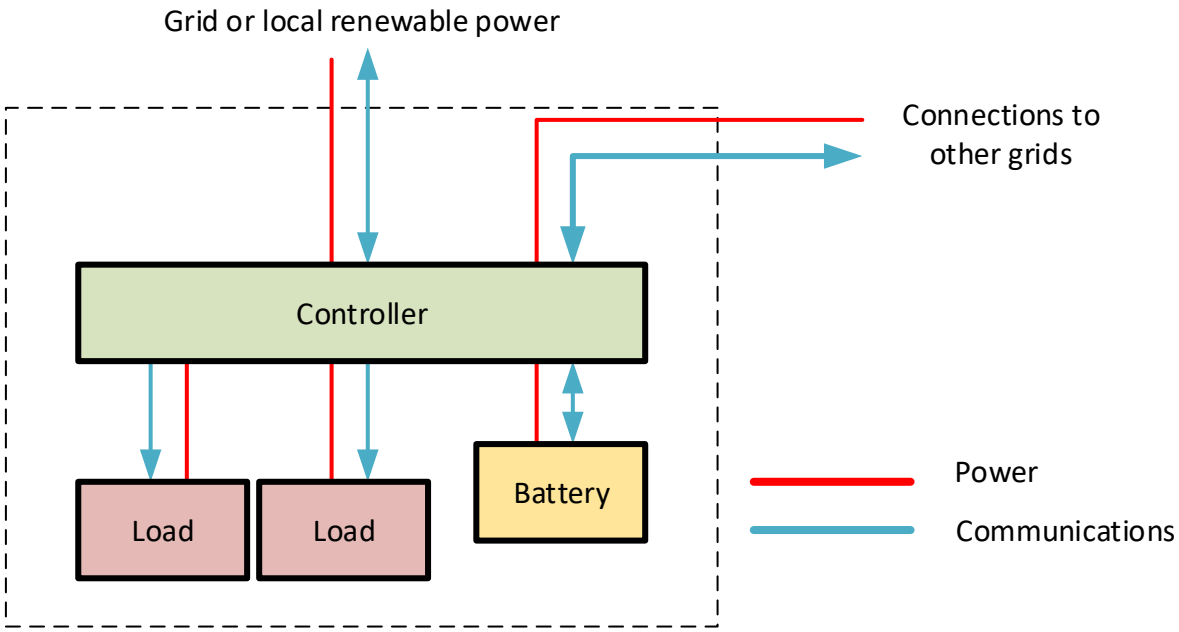

Figure 1.4: Main components in a nanogrid. Adapted from (Nordman et al., 2012)

- The controller of a nanogrid can manage the level of power supplied to the loads, negotiate with other grids through the gateways, manage internal energy storage. Different hierarchies operate e inside the controller, going from the gateway controller to the communication, loads, and other nanogrids or the grid.

- Gateways are generally two ways devices in which power processing and communication take place. Power processing can be seen as the energy transformation between the energy power source and the loads and energy storage element. For instance, power converters represent a way to process the energy and allow the power flow between other sources and loads. On the other hand, the communication gateway plays the role of providing the end-user with information about the nanogrid status and the communication link between multiple controllers facilitating the implementation of interconnected nanogrids.

- The energy stored in the battery element is controlled depending on the load needs and nanogrid operation. The controller manages the storage element and has no independent decision-making and no power connection with the other entity.

Residential AC nanogrids areas are, as indicated in Fig. 1.2, located at the low voltage distribution level. In the U.S., such voltage corresponds to 240V Line to Line, with a split-phase characteristic at the connection point due to the residential transformer component. All the loads connected to the nanogrid are AC loads typically connected to the 120V line or 240V line with power levels oscillating between 4KW to 20KW maximum. Typically, the renewable energy source used in AC residential nanogrids is a PV system. When the PV system is added through a DC/DC hybrid inverter, the AC nanogrid is DC coupled. When The PV system uses a DC/AC solar inverter, the nanogrid is AC coupled. Fig. 1.5 shows the difference between both types. The energy storage element is generally a battery. The battery output is connected to the AC connection point through a DC/AC converter (inverter), which controls the battery's charge and discharge according to the mode of operation. Depending on the nanogrid design, multiple ESS can be connected in parallel to increase the energy storage capacity and output power capabilities. Finally, another optional component of AC nanogrids is backup generators, normally fossil fuel generators, which are used in off-grid operation mode.

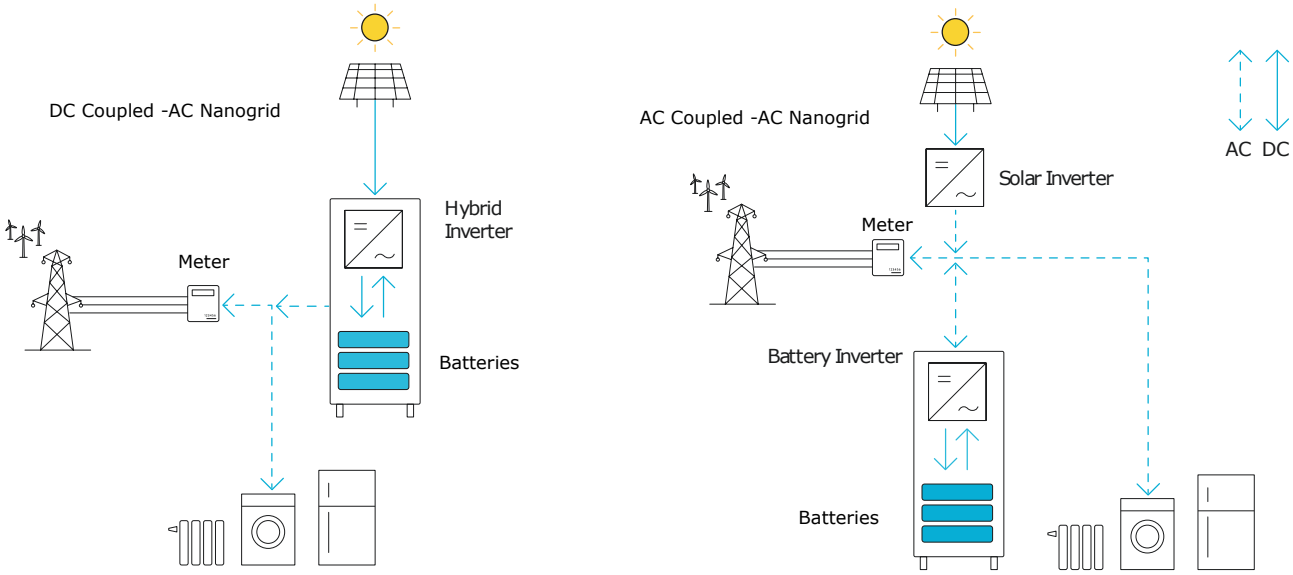

Figure 1.5: AC Nanogrids. DC coupled vs AC Coupled.

Modes of operation

- Grid-tied. It is also called on-grid because it is necessary to be connected to the main grid or to a voltage source to operate. The PV system generates energy injected into the loads directly, and the energy surplus is fed back to the grid. When a battery is used in the nanogrids, the controller is able to calculate the excess of energy and decide if such can be used to charge the batteries. Suppose the load demand is higher than the PV energy available at a particular moment,i.e. cloudy day. In that

case, the controller decides whether to provide the rest of the energy demand either from the grid or the batteries.

- Off-grid. It is also called island mode or stand-alone nanogrids. Under this operation, batteries are not an option and are necessary to keep the nanogrid running. In this case, the system acts in a more autonomous way providing the load with the demanded energy from the batteries and PV as well as charging the batteries whenever PV energy is available. Depending on the controller complexity, and whether or not it is a managed nanogrid, optimization goals such as load shedding, PV energy optimization, and or fuel consumption optimization (in case of generator utilization) are set. Typically islanded nanogrids are designed to cover power outage situations in a grid-tied system or for rural area operations where power system distribution is not available.

Importance of Islanded Nanogrids

Residential nanogrids are crucial for the modernization of the electrical power system. As it was mentioned before, allowing the incorporation of renewable is only possible by increasing the use of distributed residential nanogrid, which could allow more robustness for the power system in the aggregation of smart grids and the consolidation of a modern power system. They do, however, represent a solution for populations for whom power is vital for their survival. Hurricanes and storms are catastrophic events for the power system. Different parts of the country are affected by such devastating scenarios. In most cases, users have to withstand without energy access for days and months (O'Neill-Carrillo & Irizarry-Rivera, 2019). The United States Department of Energy found that an average household in the United States goes without power for 8 hours a year. This number varies widely among individual states: households in Florida lose power supply on average for 40 hours, whereas those in Washington, D.C. lose power supply for about 2 hours. These power outages occur for various reasons. Although storms and hurricanes account for the vast majority of these outages, power network attacks are also a risk to consider. The resilience of a system can be defined as its ability to prepare, predict, sustain and recover from an outage (Chatterji & Bazilian, 2020). In other words implementation of AC residential nanogrids could help to improve the power system resiliency. On the other hand, the world faces a global problem of lack of electrification in rural areas where approximately 1.2 billion people live without electric energy access. Different nanogrids used in rural areas have shown the applicability to provide local communities in third-world countries with basic energy coverage. Increasing the implementation of

stand-alone nanogrids in rural areas could help developing nations fulfill other basic needs such as potable water through the water pump and food providing electricity for working irrigation systems (Sood, 2020).

1.3 Main Challenges of Residential AC Nanogrids

Some of the challenges associated to the adoption of residential nanogrids are :

- Battery capacity and optimization. In a residential nanogrid, the capacity for energy storage is defined by the household size. Optimizing energy consumption patterns, as well as dispatching models based on renewable energy availability, is essential to guarantee system resiliency. In some cases, such optimization can be achieved by scheduling load consumption or by load curtailment; whereas, in other instances, optimization in the use of renewable energy resources can also be conceived. The latter implies a stochastic model over the non-deterministic energy generation profile.

- Synchronization and stable operation while off-grid. Synchronous operation during stand alone performance is critical for increasing system capacity, reliability and resiliency. Stand alone systems are defined as such systems where no utility interconnection is possible. For instance remote rural areas or locations where natural disasters have occurred and the electric supply could be compromised. Parallel and synchronous operation of inverters in nanogrids tries to cope with power capacity and system reliability increase goals, especially for ESS, where multiple systems can be parallelized to combine and increase the energy storage capacity and output power capabilities. It is well known that parallel inverters suffer from stability problems when sharing the load power among them.

- Efficiency and reliability. Components of the nanogrid systems have limited life cycles, and manufacturers of such systems only guaranteed the operability of such components up to 20 years. In the case of battery storage nanogrids, reliability plays an important role when it comes to the life span of PV panels, battery modules or battery cells, and power electronic converters.

The work summarized in this document looks toward the analysis of non-linear control structures used in the power and energy control in residential AC nanogrids systems. This study was motivated by the challenges associated with the nanogrids' power and energy capacity scalability, batteries prognosis analysis, and optimal energy management, particularly for islanded systems. Chapter 2 proposes using a non-linear droop control structure that aims to alter conventional linear droops for the benefit and performance of the active and

reactive power sharing of multiple inverters connected in parallel in an islanded nanogrid. Challenges over the system stability are presented when reactive power-sharing is required. Chapter 3 presents the analysis of the power transfer in residential energy storage systems. A novel method for the online estimation of the battery impedance based on that analysis is proposed. A non-linear control law for the DC/DC converter used in these systems is studied. Finally, Chapter 4 shows the study of a non-linear optimization problem for the energy management of autonomous stand-alone residential nanogrids.

Among the main contributions of this dissertation, the following are the most relevant:

- Development of a non-linear model using time-varying phasor analysis for the electrical behavior of multiples inverters connected in parallel in stand-alone residential nanogrid.
- Mathematical tool to evaluate the contraction region of two single-phase inverters connected in parallel sharing reactive power and using a non-linear droop control with virtual impedance.
- A development of an online non-perturbing method to estimate the internal impedance of battery modules in energy storage systems used in residential AC nanogrids
- Formulation of a non-linear control law based on feedback linearization analysis for DC/DC converters used in residential energy storage systems.
- Formulation of a non-linear optimization problem for the energy management of an autonomous residential nanogrid considering the PV energy generation's as a stochastic process.

Chapter 2

Island Operation of AC Nanogrids

A partial content of this chapter has been published at APEC 2019.[1]

Full content of this chapter was submitted to the IEEE Transactions on Energy Conversion.

2.1 Parallel Operation of Inverters

Typically, while residential ESS are connected to the grid, the inverter has to follow the grid reference, therefore acting as a current source. During off-grid operation (back-up mode), at least one ESS inverter act as grid forming, and other components connected to the residential nanogrid, i.e., PV inverters and other ESS inverters, have to follow this reference. The disadvantages of having inverters still following a voltage reference in a nanogrid, can vary from slow re-connection to limited capabilities for responding to fast load transient and different load dynamics.

In order to overcome the aforementioned limitations, it is desired that additional ESS in the nanogrid operate also as voltage sources and harmonically synchronize with other ESS in the nanogrid. Under this parallel operation mode, the biggest challenge of the ESS is to guarantee load sharing among different units connected in parallel (Q. Zhong, 2013).

Recent advances in control of ESS have facilitated their autonomous parallel operation, avoiding communication links between the inverters in the microgrid. The advantages of such inverters configurations include: improved reliability and no constraint on the location of the inverters or ESS units (Guerrero et al., 2005). To achieve this parallel operation, the conventional droop method is often adopted, which is based on

[1] A. Berzoy, A. Salazar, F. Khalizheli, C. Restrepo and J. M. Velni, "Non-linear Droop Control of Parallel Split-phase Inverters for Residential Nanogrids," 2019 IEEE Applied Power Electronics Conference and Exposition (APEC), Anaheim, CA, USA, 2019, pp. 1150-1156, doi: 10.1109/APEC.2019.8721932.

a well-known concept in large-scale power systems that consists of linearly drooping the frequency/voltage of AC generator when its output active/reactive power increases.

It is also known that parallel operation of inverters suffer from stability problems when sharing the load power among them. One of the main challenges in the implementation of droop controllers is the reactive power sharing mismatch. Realizing accurate reactive power sharing is hard to achieve due to the voltage differences at the inverter's output terminals caused by unequal line impedance or inverters' different ratings. The stability of conventional droops can be compromised under several load and line conditions, as well as droop parameters. Virtual impedance and nonlinear droop have been proposed in the literature to improve system stability while enhancing active and reactive power sharing (Berzoy et al., 2019), (Moslemi & Mohammadpour, 2015). In order to cope with the issues associated with the droop control, different approaches have been proposed in the literature (Guerrero et al., 2011), (Li & Kao, 2009). For instance, to improve the active damping of the low-frequency power-sharing modes and the reactive power compensation, a modified droop function is employed in (Hamzeh et al., 2013). The idea of nonlinear droop was first introduced in (Simpson-Porco et al., 2017), (Simpson-Porco et al., 2013). In (Simpson-Porco et al., 2013), a nonlinear stability analysis of the frequency-droop controller was performed. In (Simpson-Porco et al., 2017), a nonlinear stability analysis of the reactive power-sharing was conducted. In neither of those two works, authors focus on a nonlinear droop equation to reach the desired transient and steady state performance. References (Bidram et al., 2012), (Q. Zhong, 2013) proposed modified droop control methods focusing on specific drawbacks of the original droop techniques without considering power losses.

Modeling the dynamic behavior of parallel inverters in residential nanogrids can be achieved by different techniques. Dynamic phasor or time-varying phasor (tvp) theory and small-signal analysis are typically employed for this purpose (Mariani & Vasca, 2013). Traditional phasor analysis has been used for decades for transient analysis of power systems under the quasi-stationary assumption; that is, the transients are assumed to be sufficiently slow so that they can be approximated to be stationary. It has been proven that the efficient and fast transient representation of time-varying phasor can be used for the formulation of differential equations in RLC networks while the resulting system in the phasor domain is consistent with the original system stability properties (Peng et al., 2020) (Venkatasubramanian, 1994).

The main contributions of this paper can be summarized as follows:

- A time-varying phasor model of N inverters connected in parallel for stand-alone operation in residential nanogrids is developed and corroborated by comparing against a power electronics switching simulation and experimental results.
- The developed model is used to study the closed-loop stability of a nonlinear droop control with virtual impedance using nonlinear contraction theory.
- The stability analysis results demonstrate the criteria for local exponential convergence for any trajectory contained in a ball with constant radius centered at the system equilibrium point.
- Validations through simulation studies and hardware experiments are performed, using single-phase inverters which are part of a commercially available residential ESS.

2.2 General Definitions

This section provides preliminaries on fundamental droop control and concept of virtual impedance for droop control and finally introduces time-varying phasor notation.

2.2.1 Droop Control

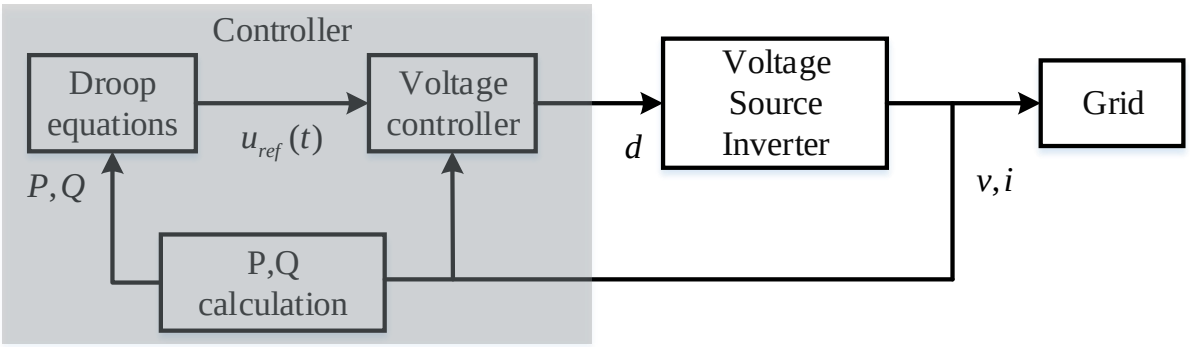

Figure 2.1: Simplified block diagram for a droop-based controller.

A basic representation of the droop control scheme is depicted in Fig. 2.1. The voltage controller goal is to guarantee that the sinusoidal voltage reference is tracked. The reference voltage signal is calculated using (2.1), where $U(t)$ and $\omega(t)$ are the instantaneous RMS voltage and frequency values. These variables are obtained

using the droop equations and are related to the output power of the inverter.

$$u_{ref}(t) = \sqrt{2}\, U(t)\, \cos\left(\int_0^t \omega(\tau) d\tau\right). \tag{2.1}$$

The droop equations come form the power flow control theory analysis. Fig 2.2 shows the equivalent circuit of an inverter connected to an AC bus. The complex power drawn by the bus can be calculated as in (2.2).

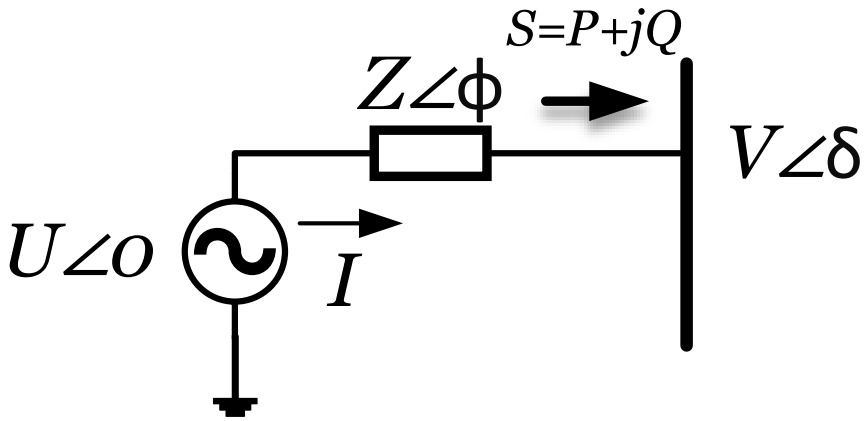

Figure 2.2: One-line diagram of an inverter connected to an AC bus.

$$S = P + jQ, \tag{2.2}$$

where P and Q are active and reactive power respectively, which are obtained using equations 2.3 and 2.4

$$P = \frac{U^2 \cos(\phi) - U\,V\,\cos(\phi - \delta)}{Z}, \tag{2.3}$$

$$Q = \frac{U^2 \sin(\phi) - U\,V\,\sin(\phi - \delta)}{Z}. \tag{2.4}$$

Assuming that the inverter's output impedance is mainly inductive(i.e. $Z = jX$) (Guerrero et al., 2005) and a small phase difference between U and V (i.e., $\sin(\delta) \approx \delta$ and $\cos(\delta) \approx 1$, the expressions for active and reactive power can be approximated by equations (2.5) and (2.6)

$$P \approx \frac{U\,V\,\delta}{X}, \tag{2.5}$$

$$Q \approx \frac{U\,(U - V)}{X}. \tag{2.6}$$

Therefore, there exists a strong correlation between the active power P and the power angle δ, while the reactive power Q is strongly dependent on the voltage amplitude difference $U - V$. Inverter's controllers can adopt droop equations for the frequency and voltage amplitude to mimic AC generator's inertia. The voltage amplitude and frequency references can be defined as functions $\boldsymbol{\Omega}$ and $\boldsymbol{E}$, respectively, with $\boldsymbol{\Omega} : p \rightarrow \omega$ and $\boldsymbol{E} : q \rightarrow U$. Generally, $\boldsymbol{\Omega}$ and $\boldsymbol{E}$ are linear functions of the form

$$\boldsymbol{\Omega}(p) = \bar{\omega} - m\,p, \quad \boldsymbol{E}(q) = \bar{U} - n\,q, \tag{2.7}$$

Although classical droop control theory has focused on linear droop relations, it is also possible to use nonlinear functions, e.g., polynomial representations of degree D as follows

$$\boldsymbol{\Omega}(p) = \sum_{\rho=0}^{D} a_\rho p^\rho, \quad \boldsymbol{E}(q) = \sum_{\rho=0}^{D} b_\rho q^\rho. \tag{2.8}$$

2.2.2 Virtual Impedance concept

In order to improve the stability of the system, reduce the impact of circulating currents and share linear and nonlinear loads, one solution is to introduce a virtual impedance into the system by an additional control loop of the form

$$u_{ref} = u_{droop} - Z_v\,i, \tag{2.9}$$

where u_{droop} is the voltage reference delivered by the droop equations, Z_v is the virtual output impedance and i is the inverter output current. Fig. 2.3 shows a modified representation for a droop scheme with the virtual impedance loop in it. Basically, the voltage drop introduced by the virtual impedance loop increases inverter output impedance and therefore increases the impedance between the inverter and the common connection point. This will result in reducing circulating currents in the system (Matas et al., 2010).

2.2.3 Time Varying Phasor Notation

Consider a modulated signal of the form

$$y(t) = \sqrt{2}\,Y(t)\,\cos\Big(\omega\,t + \delta_y(t)\Big). \tag{2.10}$$

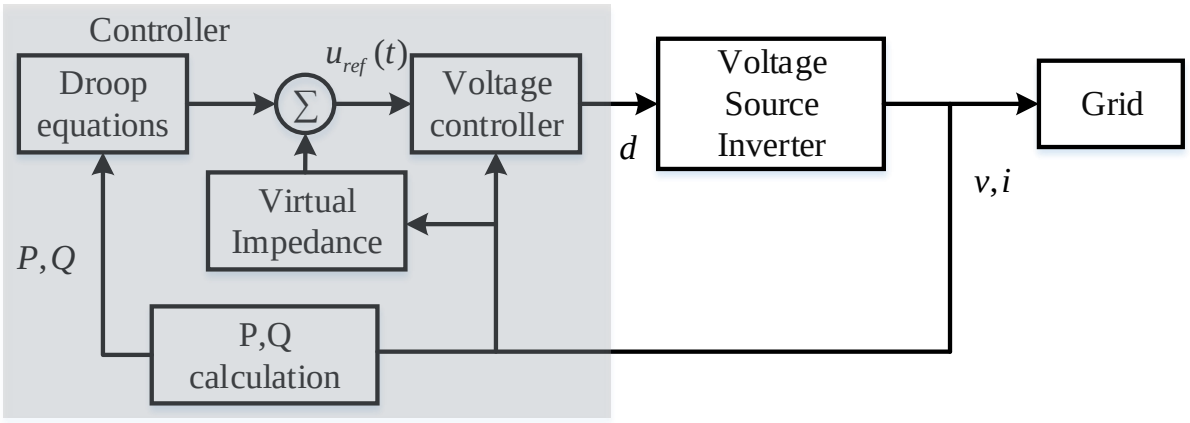

Figure 2.3: Simplified block diagram for a droop based controller with virtual impedance.

Mathematically, by phasor representation, time-varying phasor definition is given by (2.11), where $\mathcal{P}$ is the phasor transformation operator,

$$\mathcal{P}(y(t)) := \hat{y}(t) = \sqrt{2}\, Y(t) e^{j\delta_y(t)}. \tag{2.11}$$

The relation between the original signal $y(t)$ and the time-varying phasor $\hat{y}(t)$ is given by

$$y(t) := \mathcal{R}e(\hat{y}(t)\, e^{j\omega t}) = \sqrt{2}\, \mathcal{R}e(Y(t)\, e^{j\omega t + \delta_y(t)}). \tag{2.12}$$

If y is a sinusoidal signal with constant magnitude and constant frequency, $\hat{y}$ is not time dependent and coincides with classical definition of phasors. However, it is a dynamic phasor when Y and δ are time-varying.

A feature for the time-varying phasor transformation comes when the time derivative operation is considered.

Property 1 :

$$\mathcal{P}(\frac{dy(t)}{dt}) = \frac{d\mathcal{P}(y(t))}{dt} + j\,\omega\,\mathcal{P}(y(t)). \tag{2.13}$$

This property can be demonstrated by using rule chain on (2.12).

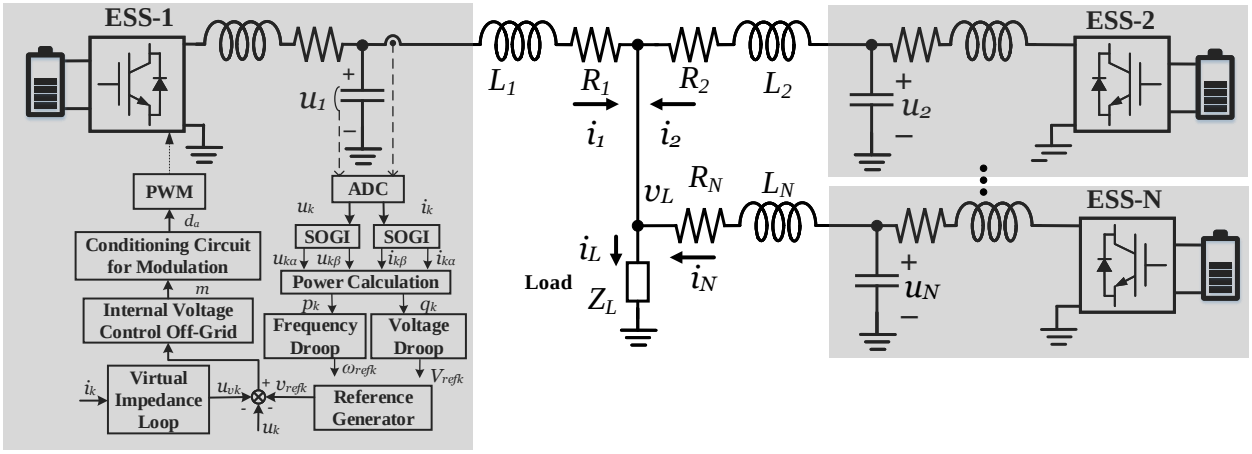

Figure 2.4: Circuit Scheme of N-Parallel ESS.

2.3 Time-varying Phasor Model for Inverters Connected in Parallel

The analyzed system that is shown in Fig. 2.4 consists of N inverters connected in parallel to a single point of connection (SPC) and an impedance Z_L as load. The subscript k represents the ESS number ($k = 1, ..., N$). The line series impedance for each output of the inverters is modeled by a resistance R_k and an inductance L_k. The output voltage of each inverter is denoted by $u_k(t)$ and the output current by $i_k(t)$.

Definition 2.3.1 *Let the output voltage of each inverter connected in parallel be represented by the modulated signal*

$$u_k(t) = \sqrt{2}U_k(t)cos(\theta_k(t)).$$

Then,

$$\hat{u}_k(t) = \sqrt{2}\mathcal{R}e(\hat{u}_k(t)e^{j\theta_k(t)}) = U_k(t) \tag{2.14}$$

Definition 2.3.2 *Let the output current of each inverter connected in parallel be represented by the modulated signal*

$$i_k(t) = \sqrt{2}I_k(t)cos(\theta_k(t) + \phi_k(t)).$$

Then,

$$\hat{i}_k(t) = \sqrt{2}\mathcal{R}e(\hat{i}_k(t)e^{j\theta_k(t)}) = I_k(t)e^{j\phi_k(t)}. \tag{2.15}$$

Definition 2.3.3 *Let the angle difference δ_k between each inverter and the load voltage angle θ_L be*

$$\delta_k(t) = \theta_k(t) - \theta_L(t).$$

Definition 2.3.4 *Let the load voltage be represented by the modulated signal*

$$v_L(t) = \sqrt{2}V_L(t)cos(\theta_L(t)) = \sqrt{2}\mathcal{R}e(\hat{v}_L(t)e^{j\theta_L(t)}).$$

Then,

$$\hat{v}_L(t) = V_L(t)$$

The load current $i_L(t)$ is given by :

$$i_L(t) = i_1(t) + i_2(t) + \cdots + i_N(t), \tag{2.16}$$

where N is the total number of inverters in the nanogrid.

According to 2.11, 2.12 and 2.15, the time dynamic phsaor equivalent for expression 2.16 is given by

$$i_L(t) = \sqrt{2}\mathcal{R}e(\hat{i}_1(t)e^{j\theta_1(t)} + \hat{i}_2(t)e^{j\theta_2(t)} + \cdots \hat{i}(t)_N e^{j\theta_N(t)}). \tag{2.17}$$

The first derivative of $i_L(t)$ with respect to t can be obtained by applying the derivative operator on 2.17

$$\begin{aligned}\frac{di_L(t)}{dt} = \sqrt{2}\mathcal{R}e\Big(&\frac{d\hat{i}_1(t)}{dt}e^{j\theta_1(t)} + j\frac{d\theta_1(t)}{dt}\hat{i}_1(t)e^{j\theta_1(t)} \\ &+ \frac{d\hat{i}_2(t)}{dt}e^{j\theta_2(t)} + j\frac{d\theta_2(t)}{dt}\hat{i}_2(t)e^{j\theta_2(t)} + \cdots \\ &+ \frac{d\hat{i}_N(t)}{dt}e^{j\theta_N(t)} + j\frac{d\theta_N(t)}{dt}\hat{i}_N(t)e^{j\theta_N(t)}\Big).\end{aligned} \tag{2.18}$$

For a load impedance defined as $Z_L = R_L + j\omega L_L$ Load voltage can be modeled as

$$v_L(t) = R_L i_L(t) + L_L\frac{di_L(t)}{dt}. \tag{2.19}$$

Substituting (2.16) and (2.18) into (2.19) and using definitions 2.3.3, 2.3.4, then the load voltage can be expressed as :

$$\sqrt{2}\ \mathcal{R}e(\hat{v}_L(t)e^{j\theta_L(t)}) \quad = \quad \sqrt{2}\ \mathcal{R}e\Big(\big(\sum_{k=1}^{N}(R_L\hat{i}_k(t)e^{j\delta_k(t)} + L_L\Big(\frac{d\hat{i}_k(t)}{dt} + j\frac{d\theta_k(t)}{dt}\hat{i}_k(t)\Big)e^{j\delta_k(t)}\big)e^{j\theta_L(t)}\Big) \quad (2.20)$$

which is Equivalent to

$$\hat{v}_L(t) = \sum_{k=1}^{N} R_L\hat{i}_k(t)e^{j\delta_k(t)} + L_L\Big(\frac{d\hat{i}_k(t)}{dt} + j\frac{d\theta_k(t)}{dt}\hat{i}_k(t)\Big)e^{j\delta_k(t)}. \quad (2.21)$$

Also, the analysis of each inverter's output circuit gives

$$u_k(t) - R_k i_k(t) - L_k\frac{di_k(t)}{dt} - v_L(t) = 0, \quad (2.22)$$

$$\sqrt{2}\,\mathcal{R}e(\hat{u}_k(t)e^{j\theta_k(t)}) - R_k\,\sqrt{2}\,\mathcal{R}e(\hat{i}_k(t)e^{j\theta_k(t)}) - L_k\,\sqrt{2}\,\mathcal{R}e\Big(\frac{d\hat{i}_k(t)}{dt}e^{j\theta_k(t)} + j\frac{d\theta_k(t)}{dt}\hat{i}_k(t)e^{j\theta_k(t)}\Big) - \sqrt{2}\,\mathcal{R}e(\hat{v}_L(t)e^{j\theta_k(t)}e^{-j\delta_k(t)}) = 0. \quad (2.23)$$

$$\sqrt{2}\mathcal{R}e\Big(\hat{u}_k(t) - R_k\hat{i}_k(t) - L_k\Big(\frac{d\hat{i}_k(t)}{dt} + j\frac{d\theta_k(t)}{dt}\hat{i}_k(t)\Big) - \hat{v}_L(t)e^{-j\delta_k(t)}\Big)e^{j\theta_k(t)} \quad = \quad 0. \quad (2.24)$$

which is Equivalent to

$$\hat{u}_k(t) - R_k\hat{i}_k(t) - L_k\Big(\frac{d\hat{i}_k(t)}{dt} + j\frac{d\theta_k(t)}{dt}\hat{i}_k(t)\Big) - \hat{v}_L(t)e^{-j\delta_k(t)} = 0. \quad (2.25)$$

Substituting (2.21) into (2.25),

$$\hat{u}_k(t) - \Big(R_{kL} + jL_{kL}\frac{d\theta_k(t)}{dt}\Big)\hat{i}_k(t) - L_{kL}\frac{d\hat{i}_k(t)}{dt} - \sum_{\varsigma=1,\forall\varsigma\neq k}^{N}\Big((R_L + jL_L\frac{d\theta_\varsigma(t)}{dt})\hat{i}_\varsigma(t) + L_L\frac{d\hat{i}_\varsigma(t)}{dt}\Big)e^{j\theta_{\varsigma k}(t)} = 0, \quad (2.26)$$

where

$$R_{kL} = R_k + R_L,$$

$$L_{kL} = L_k + L_L,$$

$$\theta_{\varsigma k}(t) = \theta_\varsigma(t) - \theta_k(t).$$

Equations (2.26) and (2.25) summarize the tvp model in open loop for N ESS connected in parallel to a single series inductive-resistive load.

2.3.1 Analysis for two inverters connected in parallel

To analyze the behavior of $N = 2$ systems connected in parallel to an inductive-resistive load, the model described by equation (2.26) is used.

$$\hat{u}_1(t) - \bar{Z}_{I_1}(t)\hat{i}_1(t) - Z_{I_2}(t)\hat{i}_2(t)e^{j(\theta_2(t)-\theta_1(t))} - L_{1L}\frac{d\hat{i}_1(t)}{dt} - L_L\frac{d\hat{i}_2(t)}{dt}e^{j(\theta_2(t)-\theta_1(t))} = 0. \quad (2.27)$$

$$\hat{u}_2(t) - \bar{Z}_{I_2}(t)\hat{i}_2(t) - Z_{I_1}(t)\hat{i}_1(t)e^{-j(\theta_2(t)-\theta_1(t))} - L_{2L}\frac{d\hat{i}_2(t)}{dt} - L_L\frac{d\hat{i}_1(t)}{dt}e^{-j(\theta_2(t)-\theta_1(t))} = 0. \quad (2.28)$$

where

$$
\begin{aligned}
\bar{Z}_{I_1}(t) &= R_{1L} + jL_{1L}\frac{d\theta_1(t)}{dt},\\
Z_{I_2}(t) &= R_L + jL_L\frac{d\theta_2(t)}{dt},\\
\bar{Z}_{I_2}(t) &= R_{2L} + jL_{2L}\frac{d\theta_2(t)}{dt},\\
Z_{I_1}(t) &= R_L + jL_L\frac{d\theta_1(t)}{dt}.
\end{aligned}
\tag{2.29}
$$

Then, (2.27) and (2.28) can be solved for $\frac{d\hat{i}_1}{dt}$ and $\frac{d\hat{i}_2}{dt}$.

$$
\begin{aligned}
\frac{d\hat{i}_1(t)}{dt} = \frac{1}{L_o}\Big((Z_{I_1}(t)L_L - \bar{Z}_{I_1}L_{2L})\hat{i}_1(t)\\
+ (\bar{Z}_{I_2}(t)L_L - Z_{I_2}(t)L_{2L})\hat{i}_2(t)e^{j\theta_{21}(t)}\\
- L_L U_2(t)e^{j\theta_{21}(t)} + L_{2L}U_1(t)\Big).
\end{aligned}
\tag{2.30}
$$

$$
\begin{aligned}
\frac{d\hat{i}_2}{dt} = \frac{1}{L_o}\Big((Z_{I_1}(t)L_{1L} - \bar{Z}_{I_1}(t)L_L)\hat{i}_1(t)e^{-j\theta_{21}(t)}\\
+ (\bar{Z}_{I_2}(t)L_{1L} - Z_{I_2}(t)L_L)\hat{i}_2(t)\\
- L_L U_1(t)e^{-j(\theta_{21}(t))} + L_{1L}U_2(t)\Big),
\end{aligned}
\tag{2.31}
$$

where

$$
\begin{aligned}
L_o &= L_{1L}L_{2L} - L_L^2,\\
\theta_{21}(t) &= \theta_2(t) - \theta_1(t).
\end{aligned}
$$

The model is completed by defining $\frac{d\theta_1}{dt}$ and $\frac{d\theta_2}{dt}$,

$$
\boxed{\frac{d\theta_1}{dt} = f_{\omega_1}(\cdot)} \tag{2.32}
$$

$$
\boxed{\frac{d\theta_2}{dt} = f_{\omega_2}(\cdot)} \tag{2.33}
$$

where $f_{\omega_k}(\cdot)$ is a smooth function.

We can also introduce the dynamic phasor notation for $\hat{i}_k(t)$ as a dynamic complex vector

$$\hat{i}_k(t) = I_{k_{re}}(t) + jI_{k_{im}}(t), \tag{2.34}$$

where

$$I_{k_{re}}(t) = \mathcal{R}e(\hat{i}_k),$$

$$I_{k_{im}}(t) = \mathcal{I}m(\hat{i}_k).$$

Where *re* and *im* can be conceived as operators, giving the real and the imaginary parts of a complex vector respectively.

In the same manner, the load current can also be represented as dynamic complex vector notation

$$\hat{i}_L(t) = I_{L_{re}}(t) + jI_{L_{im}}(t), \tag{2.35}$$

where

$$I_{L_{re}}(t) = I_{1_{re}}(t) + I_{2_{re}}(t),$$

$$I_{L_{im}}(t) = I_{1_{im}}(t) + I_{2_{im}}(t).$$

The time-varying phase for the load current is given by

$$\phi_L(t) = \arctan\left(\frac{I_{L_{im}}(t)}{I_{L_{re}}(t)}\right). \tag{2.36}$$

And therefore the tvp notation for the load current $\hat{i}_L(t)$ can be expressed as

$$\hat{i}_L(t) = I_L(t)e^{-j\phi_L(t)}, \tag{2.37}$$

where $I_L(t)$ is the time-varying RMS load current.

Model General Form The time-varying phasor states can also be expressed in terms of its real and imaginary components. To facilitate the mathematical development and to avoid the use of additional sub-indices to represent the imaginary and real operators, the model can be expressed in a general form as $\dot{\boldsymbol{\zeta}} = \hat{\boldsymbol{f}}(\zeta) + \hat{\boldsymbol{g}}(\zeta)u$.

Therefore by using the system in (2.30) and (2.31) and using the states names in (2.38), the full state time-varying system can be obtained by (2.39).

$$\begin{bmatrix} \zeta_1 \\ \zeta_2 \\ \zeta_3 \\ \zeta_4 \\ \zeta_5 \\ \zeta_6 \end{bmatrix} = \begin{bmatrix} \mathcal{R}e(\hat{i_1}) \\ \mathcal{I}m(\hat{i_1}) \\ \mathcal{R}e(\hat{i_2}) \\ \mathcal{I}m(\hat{i_2}) \\ f_{\omega_1}(\cdot) \\ f_{\omega_2}(\cdot) \end{bmatrix} \tag{2.38}$$

$$\begin{aligned}
\dot{\zeta_1} &= -\alpha_1\zeta_1 + \dot{\zeta_5}\zeta_2 + \alpha_2\cos(\zeta_5-\zeta_6)\zeta_3 + \alpha_2\sin(\zeta_5-\zeta_6)\zeta_4 + \frac{L_{2L}}{L_o}U_1 - \frac{L_L}{L_o}\cos(\zeta_5-\zeta_6)U_2,\\
\dot{\zeta_2} &= -\dot{\zeta_5}\zeta_1 - \alpha_1\zeta_2 - \alpha_2\sin(\zeta_5-\zeta_6)\zeta_3 + \alpha_2\cos(\zeta_5-\zeta_6)\zeta_4 + \frac{L_L}{L_o}\sin(\zeta_5-\zeta_6)U_2,\\
\dot{\zeta_3} &= \beta_2\cos(\zeta_5-\zeta_6)\zeta_1 - \beta_2\sin(\zeta_5-\zeta_6)\zeta_2 - \beta_1\zeta_3 + \dot{\zeta_6}\zeta_4 - \frac{L_L}{L_o}\cos(\zeta_5-\zeta_6)U_1 + \frac{L_{1L}}{L_o}U_2,\\
\dot{\zeta_4} &= \beta_2\sin(\zeta_5-\zeta_6)\zeta_1 + \beta_2\cos(\zeta_5-\zeta_6)\zeta_2 - \dot{\zeta_6}\zeta_3 - \beta_1\zeta_4 - \frac{L_L}{L_o}\sin(\zeta_5-\zeta_6)U_1,\\
\dot{\zeta_5} &= f_{\omega_1}(\cdot),\\
\dot{\zeta_6} &= f_{\omega_2}(\cdot).
\end{aligned} \tag{2.39}$$

where

$$\alpha_1 = (L_{2L}(R_1+R_L) - L_LR_L)/L_o,$$

$$\alpha_2 = (L_L(R_2+R_L) - L_{2L}R_L)/L_o,$$

$$\beta_1 = (L_{1L}(R_2+R_L) - L_LR_L)/L_o,$$

$$\beta_2 = (L_L(R_1+R_L) - L_{1L}R_L)/L_o.$$

Assuming small signal variation between the systems' phases,i.e. $\theta_1 \approx \theta_2$ the open-loop model of the system is then approximated by

$$
\begin{aligned}
\dot{\zeta}_1 &= -\alpha_1\zeta_1 + \dot{\zeta}_5\zeta_2 + \alpha_2\zeta_3 + \alpha_2(\zeta_5 - \zeta_6)\zeta_4 + \frac{L_{2L}}{L_o}U_1 - \frac{L_L}{L_o}U_2,\\
\dot{\zeta}_2 &= -\dot{\zeta}_5\zeta_1 - \alpha_1\zeta_2 - \alpha_2(\zeta_5 - \zeta_6)\zeta_3 + \alpha_2\zeta_4 + \frac{L_L}{L_o}U_2(\zeta_5 - \zeta_6),\\
\dot{\zeta}_3 &= \beta_2\zeta_1 - \beta_2(\zeta_5 - \zeta_6)\zeta_2 - \beta_1\zeta_3 + \dot{\zeta}_6\zeta_4 - \frac{L_L}{L_o}U_1 + \frac{L_{1L}}{L_o}U_2,\\
\dot{\zeta}_4 &= \beta_2(\zeta_5 - \zeta_6)\zeta_1 + \beta_2\zeta_2 - \dot{\zeta}_6\zeta_3 - \beta_1\zeta_4 - \frac{L_L}{L_o}U_1(\zeta_5 - \zeta_6),\\
\dot{\zeta}_5 &= f_{\omega_1}(\cdot),\\
\dot{\zeta}_6 &= f_{\omega_2}(\cdot).
\end{aligned}
\tag{2.40}
$$

2.3.2 Closed Loop Model

In this section it will be shown how the developed model in (2.40) can be used to study the closed loop stability of the system with different droop control structures including the virtual impedance concept.

Each inverter output reference voltage can be calculated by using (2.41)

$$
U_k(t) = \bar{U}_k + n_k(\bar{Q}_k - q_k(t)), \tag{2.41}
$$

where p_k is defined by 2.42 and q_k is defined by 2.43.

$$
p_k(t) = \mathcal{R}e(U_k\hat{i}^*_{g_k}) = U_k(t)\mathcal{R}e(\hat{i}_k(t)). \tag{2.42}
$$

$$
q_k(t) = \mathcal{I}m(U_k\hat{i}^*_{g_k}) = -U_k(t)\mathcal{I}m(\hat{i}_k(t)). \tag{2.43}
$$

Substituting (2.42) and (2.43) into (2.41), the expression in (2.44) for the closed loop output voltage reference is obtained. Such expression will be used in the following sections to develop the closed loop time-varying model for three different cases. Case I Linear droop. Case II, Non linear droop. Case III Non-linear droop with virtual impedance.

$$
U_k(t) = \frac{\bar{U}_k + n_k\,\bar{Q}_k}{1 - n_k\,\mathcal{I}m(\hat{i}_k(t))} \tag{2.44}
$$

Case I. Linear Droop Relation

The classical linear droop functions are of the general form

$$\frac{d\theta_k}{dt} = \bar{\omega}_k + m_k(\bar{P}_k - p_k(t)). \tag{2.45}$$

Substituting (2.42) into (2.45), the following expression in time-varying phasor notation is obtained,

$$\frac{d\theta_k}{dt} = \bar{\omega}_k + m_k(\bar{P}_k - U_k(t)\mathcal{R}e(\hat{i}_{g_k}(t))). \tag{2.46}$$

Assuming small angle variation, the closed loop model can be deduced by substituting (2.46) into (2.40).

$$\begin{aligned}
\dot{\zeta}_1 &= -\alpha_1\zeta_1 + (\bar{\omega}_1 + m_1\bar{P}_1)\zeta_2 + \alpha_2\zeta_3 + \alpha_2(\zeta_5 - \zeta_6)\zeta_4 + (\frac{L_{2L}}{L_o} - m_1\zeta_1\zeta_2)U_1 - \frac{L_L}{L_o}U_2,\\
\dot{\zeta}_2 &= -(\bar{\omega}_1 + m_1\bar{P}_1)\zeta_1 - \alpha_1\zeta_2 - \alpha_2(\zeta_5 - \zeta_6)\zeta_3 + \alpha_2\zeta_4 + m_1\zeta_1^2U_1 + \frac{L_L}{L_o}U_2(\zeta_5 - \zeta_6),\\
\dot{\zeta}_3 &= \beta_2\zeta_1 - \beta_2(\zeta_5 - \zeta_6)\zeta_2 - \beta_1\zeta_3 + (\bar{\omega}_2 + m_2\bar{P}_2)\zeta_4 - \frac{L_L}{L_o}U_1 + (\frac{L_{1L}}{L_o} - m_2\zeta_3\zeta_4)U_2,\\
\dot{\zeta}_4 &= \beta_2(\zeta_5 - \zeta_6)\zeta_1 + \beta_2\zeta_2 - (\bar{\omega}_2 + m_2\bar{P}_2)\zeta_3 - \beta_1\zeta_4 - \frac{L_L}{L_o}U_1(\zeta_5 - \zeta_6) + m_2\zeta_3^2U_2,\\
\dot{\zeta}_5 &= \bar{\omega}_1 + m_1(\bar{P}_1 - U_1\zeta_1),\\
\dot{\zeta}_6 &= \bar{\omega}_2 + m_2(\bar{P}_2 - U_2\zeta_3).
\end{aligned} \tag{2.47}$$

The closed loop model is completed by substituting (2.44) into (2.47).

$$
\begin{aligned}
\dot{\zeta}_1 &= -\alpha_1\zeta_1 + (\bar{\omega}_1 + m_1\bar{P}_1)\zeta_2 + \alpha_2\zeta_3 + \alpha_2(\zeta_5 - \zeta_6)\zeta_4 + \\
&\quad (\frac{L_{2L}}{L_o} - m_1\zeta_1\zeta_2)(\frac{\bar{U}_1 + n_1\bar{Q}_1}{1 - n_1\zeta_2}) - \frac{L_L}{L_o}(\frac{\bar{U}_2 + n_2\bar{Q}_2}{1 - n_2\zeta_4}), \\
\dot{\zeta}_2 &= -(\bar{\omega}_1 + m_1\bar{P}_1)\zeta_1 - \alpha_1\zeta_2 - \alpha_2(\zeta_5 - \zeta_6)\zeta_3 + \alpha_2\zeta_4 + \\
&\quad m_1\zeta_1^2(\frac{\bar{U}_1 + n_1\bar{Q}_1}{1 - n_1\zeta_2}) + \frac{L_L}{L_o}(\zeta_5 - \zeta_6)(\frac{\bar{U}_2 + n_2\bar{Q}_2}{1 - n_2\zeta_4}), \\
\dot{\zeta}_3 &= \beta_2\zeta_1 - \beta_2(\zeta_5 - \zeta_6)\zeta_2 - \beta_1\zeta_3 + (\bar{\omega}_2 + m_2\bar{P}_2)\zeta_4 - \\
&\quad \frac{L_L}{L_o}(\frac{\bar{U}_1 + n_1\bar{Q}_1}{1 - n_1\zeta_2}) + (\frac{L_{1L}}{L_o} - m_2\zeta_3\zeta_4)(\frac{\bar{U}_2 + n_2\bar{Q}_2}{1 - n_2\zeta_4}), \\
\dot{\zeta}_4 &= \beta_2(\zeta_5 - \zeta_6)\zeta_1 + \beta_2\zeta_2 - (\bar{\omega}_2 + m_2\bar{P}_2)\zeta_3 - \beta_1\zeta_4 - \\
&\quad \frac{L_L}{L_o}(\zeta_5 - \zeta_6)(\frac{\bar{U}_1 + n_1\bar{Q}_1}{1 - n_1\zeta_2}) + m_2\zeta_3^2(\frac{\bar{U}_2 + n_2\bar{Q}_2}{1 - n_2\zeta_4}), \\
\dot{\zeta}_5 &= \bar{\omega}_1 + m_1(\bar{P}_1 - (\frac{\bar{U}_1 + n_1\bar{Q}_1}{1 - n_1\zeta_2})\zeta_1), \\
\dot{\zeta}_6 &= \bar{\omega}_2 + m_2(\bar{P}_2 - (\frac{\bar{U}_2 + n_2\bar{Q}_2}{1 - n_2\zeta_4})\zeta_3).
\end{aligned}
\tag{2.48}
$$

Case II. Non-linear Droop

In this section, a new family of functions for the frequency droop is introduced. Equation (2.49) represents the general form of this function for each inverter. This function is based on the work presented in (Berzoy et al., 2019), where the performance of the nonlinear droop controllers was compared against commonly known linear droop functions. The superiority of this type of nonlinear functions, when it comes to power sharing capabilities, was demonstrated through simulations in (Berzoy et al., 2019).

$$
\frac{d\theta_k}{dt} = \bar{\omega}_k + G_{P_k}\tanh\left(m_k(\bar{P}_k - p_k(t))\right). \tag{2.49}
$$

where positive scalar G_{P_k} can be used to set the frequency variation allowed.

The closed loop system model using small angle approximation, is defined by substituting (2.49) into the model (2.40).

$$
\begin{aligned}
\dot{\zeta}_1 &= -\alpha_1\zeta_1 + \Big(\bar{\omega}_1 + G_{P_1}\tanh\left(\Theta_1(\zeta_1,\zeta_2)\right)\Big)\zeta_2 + \alpha_2\zeta_3 + \alpha_2(\zeta_5-\zeta_6)\zeta_4 \\
&\quad + \frac{L_{2L}}{L_o}\Big(\frac{\bar{U}_1 + n_1\bar{Q}_1}{1-n_1\zeta_2}\Big) - \frac{L_L}{L_o}\Big(\frac{\bar{U}_2 + n_2\bar{Q}_2}{1-n_2\zeta_4}\Big), \\
\dot{\zeta}_2 &= -\Big(\bar{\omega}_1 + G_{P_1}\tanh\left(\Theta_1(\zeta_1,\zeta_2)\right)\Big)\zeta_1 - \alpha_1\zeta_2 - \alpha_2(\zeta_5-\zeta_6)\zeta_3 + \alpha_2\zeta_4 \\
&\quad + \frac{L_L}{L_o}(\zeta_5-\zeta_6)\Big(\frac{\bar{U}_2 + n_2\bar{Q}_2}{1-n_2\zeta_4}\Big), \\
\dot{\zeta}_3 &= \beta_2\zeta_1 - \beta_2(\zeta_5-\zeta_6)\zeta_2 - \beta_1\zeta_3 + \Big(\bar{\omega}_2 + G_{P_2}\tanh\left(\Theta_2(\zeta_3,\zeta_4)\right)\Big)\zeta_4 \\
&\quad - \frac{L_L}{L_o}\Big(\frac{\bar{U}_1 + n_1\bar{Q}_1}{1-n_1\zeta_2}\Big) + \frac{L_{1L}}{L_o}\Big(\frac{\bar{U}_2 + n_2\bar{Q}_2}{1-n_2\zeta_4}\Big), \\
\dot{\zeta}_4 &= \beta_2(\zeta_5-\zeta_6)\zeta_1 + \beta_2\zeta_2 - \beta_1\zeta_4 - \Big(\bar{\omega}_2 + G_{P_2}\tanh\left(\Theta_2(\zeta_3,\zeta_4)\right)\Big)\zeta_3 \\
&\quad - \frac{L_L}{L_o}(\zeta_5-\zeta_6)\Big(\frac{\bar{U}_1 + n_1\bar{Q}_1}{1-n_1\zeta_2}\Big), \\
\dot{\zeta}_5 &= \bar{\omega}_1 + G_{P_1}\tanh\left(\Theta_1(\zeta_1,\zeta_2)\right), \\
\dot{\zeta}_6 &= \bar{\omega}_2 + G_{P_2}\tanh\left(\Theta_2(\zeta_3,\zeta_4)\right).
\end{aligned}
\tag{2.50}
$$

Where,

$$
\Theta_1(\zeta_1,\zeta_2) = m_1\big(\bar{P}_1 - \big(\tfrac{\bar{U}_1+n_1\bar{Q}_1}{1-n_1\zeta_2}\big)\zeta_1\big),
$$

$$
\Theta_2(\zeta_3,\zeta_4) = m_2\big(\bar{P}_2 - \big(\tfrac{\bar{U}_2+n_2\bar{Q}_2}{1-n_2\zeta_4}\big)\zeta_3\big).
$$

Case III. Non-linear Droop with Virtual Impedance

In section 2.2.2, the concept of virtual impedance was introduced. Fig. 2.3 shows how the virtual impedance produces voltage drop in the reference voltage with respect to the droop voltage. The virtual impedance (Z_v) analyzed in this chapter is assumed to have a resistive component (R_v) and a reactive component ($\omega_o L_v$).

$$
Z_v = R_v + j\omega_o Lv. \tag{2.51}
$$

In a single phase inverter, the virtual impedance is introduced by decomposing the inverter's output current ($i_k(t)$) into an in-phase and quadrature components as it is shown by Fig. 2.5. In a real implementation, the decomposition is made thorough a Second Order Integrator (SOGI). Such filter structure introduces a delay; however, for the present analysis the delay is not considered.

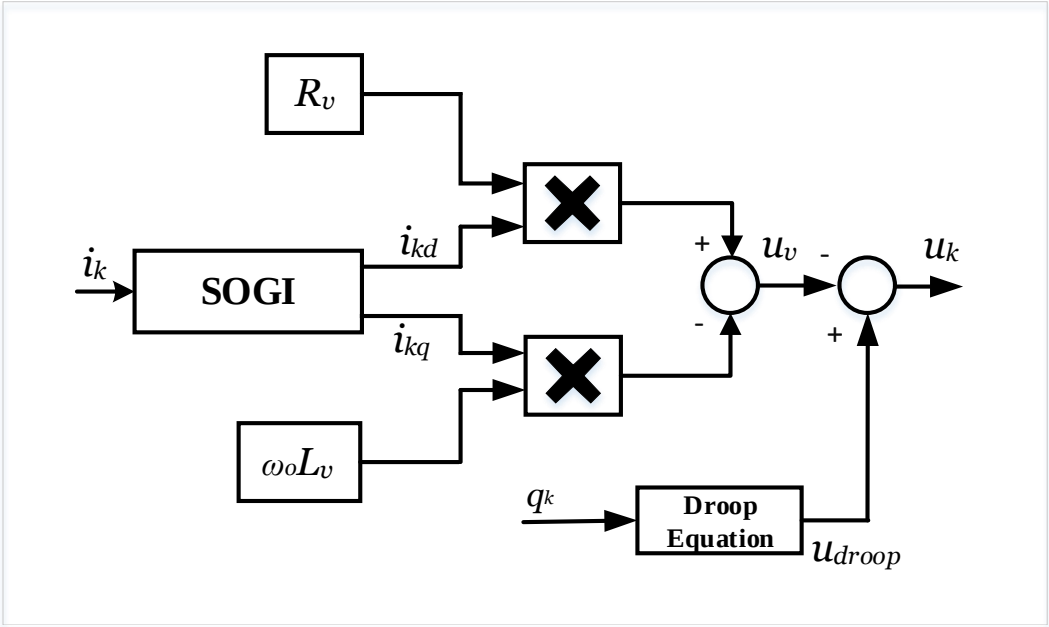

Figure 2.5: Virtual Impedance implementation in a control loop.

The in-phase (i_{k_d}) and quadrature (i_{k_q} components are defined by equations (2.52) and (2.53).

$$i_{k_d}(t) = \sqrt{2} I_k(t) \cos(\omega t + \phi_k(t)), \tag{2.52}$$

$$i_{k_q}(t) = \sqrt{2} I_k(t) \cos\left(\omega t + \phi_k(t) - \frac{\pi}{2}\right). \tag{2.53}$$

Therefore, the virtual voltage (U_{v_k}) is defined by equation 2.54

$$U_{v_k}(t) = \sqrt{2} I_k(t) R_{v_k} \cos(\omega t + \phi_k(t)) - \sqrt{2} I_k(t) \omega_o L_{v_k} \cos\left(\omega t + \phi_k(t) - \frac{\pi}{2}\right). \tag{2.54}$$

Which can be also expressed as

$$U_{v_k}(t) = \sqrt{2} \mathcal{R}e\left((I_k(t) R_{v_k} e^{j\phi_k(t)} - I_k(t) \omega_o L_{v_k} e^{j(\phi_k(t) - \frac{\pi}{2})}) e^{j\omega t}\right). \tag{2.55}$$

Applying the dynamic phasor definition, the dynamic phasor representation is given by equation 2.56.

$$\hat{u}_{v_k}(t) = (R_v + j\omega_o L_v) I_k(t) e^{j\phi_k(t)}. \tag{2.56}$$

Substituting definition 2.15 into equation 2.56 expression 2.57 is obtained,

$$\hat{u}_{v_k}(t) = (R_v + j\omega_o L_v)\hat{i}_{k_t}(t). \tag{2.57}$$

where the real and imaginary part of the dynamic phasor can be obtained as

$$\mathcal{R}e(\hat{u}_{v_k}(t)) = R_{v_k}\mathcal{R}e(\hat{i}_{k_t}(t)) - \omega_o L_{v_k}\mathcal{I}m(\hat{i}_{k_t}(t)), \tag{2.58}$$

$$\mathcal{I}m(\hat{u}_{v_k}(t)) = \omega_o L_{v_k}\mathcal{R}e(\hat{i}_{k_t}(t)) + R_{v_k}\mathcal{I}m(\hat{i}_{k_t}(t)). \tag{2.59}$$

In this case, the output voltage $\hat{u}_k(t)$ is modified in function of the virtual voltage $\hat{u}_{v_k}(t)$ and droop voltage $\hat{u}_{droop}(t)$ as

$$\hat{u}_k(t) = \hat{u}_{droop}(t) - \hat{u}_{v_k}(t). \tag{2.60}$$

where the dynamic phasor representation of the droop voltage is given by

$$\hat{u}_{droop}(t) = U_{droop}(t)e^{j\alpha(t)}. \tag{2.61}$$

And from equation 2.43 the magnitude of the dynamic phasor is obtained by

$$U_{droop}(t) = \bar{U}_k + n_k(\bar{Q}_k + \mathcal{I}m(\hat{i}_k(t))U_k(t)). \tag{2.62}$$

According to the model definition 2.3.1, the output voltage phase is assumed zero. And therefore

$$\mathcal{I}m(\hat{u}_{droop}(t)) - \mathcal{I}m(\hat{u}_{v_k}(t)) = 0 \tag{2.63}$$

and consequently

$$U_k(t) = \mathcal{R}e(\hat{u}_{droop}(t)) - \mathcal{R}e(\hat{u}_{v_k}(t)). \tag{2.64}$$

The magnitude of the droop voltage can also be expressed in terms of the real part of $\hat{u}_{droop}(t)$ and the imaginary part of $\hat{u}_{v_k}(t)$.

$$U_{droop}(t) = ((\mathcal{R}e(\hat{u}_{droop}(t)))^2 + (\mathcal{I}m(\hat{u}_{v_k}(t)))^2)^{\frac{1}{2}}. \tag{2.65}$$

Therefore, by solving (2.65) for $\mathcal{R}e(\hat{u}_{droop}(t))$ and substituting (2.62) into (2.64), the expression for $U_k(t)$ in terms of the model state variables is as follows,

$$U_k(t) = \frac{D_k + (D_k^2 - (\mathcal{R}e(\hat{u}_{v_k}(t))^2 + \mathcal{I}m(\hat{u}_{v_k}(t))^2 - \bar{U}_k^2)\Xi_k)^{\frac{1}{2}}}{\Xi_k}, \tag{2.66}$$

where

$$\Xi_k = 1 - n_k^2 \mathcal{I}m(\hat{i}_k(t))^2,$$

$$D_k = \bar{U}_k n_k \mathcal{I}m(\hat{i}_k(t)) - \mathcal{R}e(\hat{u}_{v_k}(t)),$$

$$\bar{Q}_k = 0.$$

Using voltage and frequency relations found in (2.66) and (2.49) into the open-loop system described in (2.40), the dynamic system equations for two inverters connected in parallel using nonlinear frequency droop and virtual impedance can be represented by (2.67).

$$\begin{aligned}
\dot{\zeta}_1 &= -\alpha_1\zeta_1 + \Big(\bar{\omega_1} + G_{P_1}\tanh\left(m_1(\bar{P}_1 - U_1\zeta_1)\right)\Big)\zeta_2 + \alpha_2\zeta_3 + \alpha_2(\zeta_5 - \zeta_6)\zeta_4 + \frac{L_{2L}}{L_o}U_1 - \frac{L_L}{L_o}U_2,\\
\dot{\zeta}_2 &= -\Big(\bar{\omega_1} + G_{P_1}\tanh\left(m_1(\bar{P}_1 - U_1\zeta_1)\right)\Big)\zeta_1 - \alpha_1\zeta_2 - \alpha_2(\zeta_5 - \zeta_6)\zeta_3 + \alpha_2\zeta_4 + \frac{L_L}{L_o}(\zeta_5 - \zeta_6)U_2,\\
\dot{\zeta}_3 &= \beta_2\zeta_1 - \beta_2(\zeta_5 - \zeta_6)\zeta_2 - \beta_1\zeta_3 + \Big(\bar{\omega_2} + G_{P_2}\tanh\left(m_2(\bar{P}_2 - U_2\zeta_3)\right)\Big)\zeta_4 - \frac{L_L}{L_o}U_1 + \frac{L_{1L}}{L_o}U_2,\\
\dot{\zeta}_4 &= \beta_2(\zeta_5 - \zeta_6)\zeta_1 + \beta_2\zeta_2 - \beta_1\zeta_4 - \Big(\bar{\omega_2} + G_{P_2}\tanh\left(m_2(\bar{P}_2 - U_2\zeta_3)\right)\Big)\zeta_3 - \frac{L_L}{L_o}(\zeta_5 - \zeta_6)U_1,\\
\dot{\zeta}_5 &= \bar{\omega_1} + G_{P_1}\tanh\left(m_1(\bar{P}_1 - U_1\zeta_1)\right),\\
\dot{\zeta}_6 &= \bar{\omega_2} + G_{P_2}\tanh\left(m_2(\bar{P}_2 - U_2\zeta_3)\right).
\end{aligned} \tag{2.67}$$

where,

$$U_1 = \frac{\zeta_2 L_{U_1} - \zeta_1 R_{v_1} + ((\zeta_2 L_{U_1} - \zeta_1 R_{v_1})^2 - (Z_{v_1}^2(\zeta_1^2 + \zeta_2^2) - \bar{U}_1^2)(1 - (n_1\zeta_2)^2))^{\frac{1}{2}}}{1 - (n_1\zeta_2)^2},$$

$$U_2 = \frac{\zeta_4 L_{U_2} - \zeta_3 R_{v_2} + ((\zeta_4 L_{U_2} - \zeta_3 R_{v_2})^2 - (Z_{v_2}^2(\zeta_3^2 + \zeta_4^2) - \bar{U}_2^2)(1 - (n_1\zeta_2)^2))^{\frac{1}{2}}}{1 - (n_1\zeta_2)^2}.$$

$$L_{U_1} = \bar{U}_1 n_1 + \omega_o L_{v_1},$$

$$Z_{v_1}^2 = R_{v_1}^2 + (\omega_o L_{v_1})^2,$$

$$L_{U_2} = \bar{U}_2 n_2 + \omega_o L_{v_2},$$

$$Z_{v_2}^2 = R_{v_2}^2 + (\omega_o L_{v_2})^2.$$

2.3.3 Stability analysis using contraction theory

Definition 2.3.5 *Given the system equations* $\frac{d\boldsymbol{x}}{dt} = f(\boldsymbol{x})$*, a region of the state space is called a contraction region if the Jacobian is uniformly negative definite in that region.*

In other words, the contraction region C is approximated by the matrix inequality

$$C \triangleq \left\{ \boldsymbol{x} \in \mathbb{R}^n : \frac{1}{2}\left(\frac{\partial f(x)}{\partial x} + \frac{\partial f(x)^T}{\partial x} \right) \leq -\beta I \right\},$$

where $\beta > 0$ and I is the identity matrix.

More generally, by convention, all matrix inequalities will refer to the symmetric parts of the square matrices involved. Therefore, the above expression can be rewritten as

$$C \triangleq \left\{ \boldsymbol{x} \in \mathbb{R}^n : \frac{\partial f(\boldsymbol{x})}{\partial \boldsymbol{x}} \leq -\beta I \right\}.$$

The implications of a contraction region are analyzed for more general nonlinear systems in (LOHMILLER & SLOTINE, 1998) where Theorem 1 (see below) is presented. Basically, the existence of contraction region is necessary to guarantee exponential convergence between any two given trajectories contained in a ball in the contraction region. If the trajectory for which the ball is centered to is an equilibrium point, then the contraction region represents an estimate of the domain of attraction, and therefore, any trajectory starting at an initial condition around the equilibrium will converge to equilibrium point, but not necessarily exponentially.

Theorem 1 *Given the system model* $\frac{d\boldsymbol{x}}{dt} = f(\boldsymbol{x})$*, any trajectory, which starts in a ball of constant radius centered about a given trajectory and contained at all times within a contraction region, remains in that ball and converges exponentially to the trajectory.*

Theorem 2 *Consider the system described by (2.67) with predominant inductive load, i.e., $X_L \gg R_L$. The reduced-order model of the system can be described by $\frac{d\boldsymbol{x}}{dt} = f(\boldsymbol{x})$, where $\boldsymbol{x} \in \mathbb{R}^2$ and x_1, x_2 represent the real and imaginary states for the dynamic current vector, respectively. An approximation of the contraction region for any trajectory centered at $x_1 = 0$ and with the use of a resistive virtual impedance, i.e., $Z_v = R_v$, is defined by the following subset*

$$C \triangleq \{x_2 \in \mathbb{R},\ \forall\, x_1 = 0,\ \frac{-\bar{U}}{R_{v_k}} < x_2 \leq 0 :\ R_{v_k} + \Lambda(x_2) > 0\}, \tag{2.68}$$

where

$$\Lambda(x_2) = 2\,R_k + 2\pi\,\kappa\,G_P\,(L_k + 2\,L_L)\,x_2\,(\bar{U}^2 - R_{v_k}^2 x_2^2)^{\frac{1}{2}}.$$

Proof: We assume that both inverters under analysis have identical parameters in terms of the line impedance and droop gains, even further, both droop gain parameters m_k and n_k are equal to κ, where $\kappa > 0$. We can say then without the loss of generality that perfect synchronization is achieved and

$$\zeta_5 = \zeta_6, \tag{2.69}$$

$$\zeta_1 = \zeta_3 = x_1, \tag{2.70}$$

$$\zeta_2 = \zeta_4 = x_2. \tag{2.71}$$

Substituting the equalities above into (2.67), the reduced-order model is obtained in the general form $\frac{d\boldsymbol{x}}{dt} = f(\boldsymbol{x})$, where $f(\boldsymbol{x})$ is given by

$$f(\boldsymbol{x}) = \begin{bmatrix} \alpha\,x_1 + (\bar{\omega} + 2\pi\,G_P \tanh(\kappa(\bar{P} - \mathcal{U}\,x_1)))x_2 + \frac{\mathcal{U}}{L_k + 2L_L} \\ -(\bar{\omega} + 2\pi\,G_P \tanh(\kappa(\bar{P} - \mathcal{U}\,x_1)))x_1 + \alpha\,x_2. \end{bmatrix} \tag{2.72}$$

where

$$\mathcal{U} = \frac{x_2\,\kappa\,\bar{U}_k - x_1\,R_{v_k} + (\Upsilon_k(x_1, x_2))^{\frac{1}{2}}}{1 - (\kappa\,x_2)^2},$$

$$\Upsilon_k(x_1, x_2) = (x_2\,\kappa\,\bar{U}_k - x_1\,R_{v_k})^2 - (R_{v_k}^2\,(x_1^2 + x_2^2) - \bar{U}_k^2)(1 - (\kappa x_2)^2),$$

$$\alpha = -\frac{R_K + 2R_L}{L_k + 2L_L}.$$

In order to simplify the analysis, the droop parameters $\bar{P}$ and $\bar{Q}$ are assumed to be zero, which means that the initial conditions for frequency and voltage at the origin are $\bar{\omega}$ and $\bar{U}$, respectively. Since $X_L \gg R_L$, we can

also say, without the loss of generality, that $R_L = 0$ and therefore $\alpha \approx \frac{-R_K}{L_k+2L_L}$ and the trajectory is centered at $x_1 = 0$.

The Jacobian matrix $\boldsymbol{J}$ is obtained from the system in (2.72) and the aforementioned assumptions are used in the result.

$$\boldsymbol{J} = \begin{bmatrix} \alpha + \frac{L_k\left(R_{v_k} + \frac{R_{v_k}\,\bar{U}\,\kappa\,x_2}{\sigma_2}\right)}{L_o\,\sigma_3} + \sigma_1 & \bar{\omega} - \frac{L_k\left(\bar{U}\,\kappa + \frac{x_2\,{R_{v_k}}^2\,(\kappa^2\,{x_2}^2+\sigma_3)}{\sigma_2}\right)}{L_o\,\sigma_3} + \sigma_5 \\ -\bar{\omega} & \alpha \end{bmatrix}$$

where

$$\sigma_2 = \sqrt{\bar{U}^2\,\kappa^2\,{x_2}^2 - \sigma_3\,\sigma_4},$$

$$\sigma_3 = \kappa^2\,{x_2}^2 - 1,$$

$$\sigma_4 = \bar{U}^2 - {R_{v_k}}^2\,{x_2}^2,$$

$$\sigma_5 = \frac{2\,L_k\,\kappa^2\,x_2\,\sigma_1}{L_o\,{\sigma_3}^2}.$$

$$\sigma_1 = \frac{2\,\pi\,G_P\,\kappa\,x_2\,(\sigma_2+\bar{U}\,\kappa\,x_2)}{\sigma_3}$$

By using definition 2.3.5, the contraction region can be obtained by evaluating the eigenvalues (λ) of the Jacobian of the system $\boldsymbol{J}$ in (2.72) as

$$\lambda = \begin{bmatrix} \frac{\Psi(x_2)+\sqrt{\Gamma(x_2)}}{2\,L_k\,(L_k+2\,L_L)\,(\kappa^2\,x_2^2-1)\,(R_{v_k}^2\,x_2^2(\kappa^2\,x_2^2-1)+\bar{U}^2)^{\frac{1}{2}}} \\ \frac{\Psi(x_2)-\sqrt{\Gamma(x_2)}}{2\,L_k\,(L_k+2\,L_L)\,(\kappa^2\,x_2^2-1)\,(R_{v_k}^2\,x_2^2(\kappa^2\,x_2^2-1)+\bar{U}^2)^{\frac{1}{2}}} \end{bmatrix}, \tag{2.73}$$

where

$$\Psi(x_2) = L_k\,R_{v_k}\,\bar{U}\,\kappa\,x_2 + 2\,\pi\,G_P\,L_k\,(L_k+2\,L_L)\,\kappa\,x_2\,\varrho^2 + \varrho L_k(\,R_{v_k} + 2\,R_k(1-\kappa^2\,x_2^2) + 2\,\pi\,G_P\,(L_k+2\,L_L)\,\bar{U}\,\kappa^2\,x_2^2), \tag{2.74}$$

and

$$\varrho = (R_{v_k}^2\,x_2^2(\kappa^2\,x_2^2-1) + \bar{U}^2)^{\frac{1}{2}}.$$

For small κ, we can say, without the loss of generality, that

$$(\kappa^2\,x_2^2 - 1) < 0, \tag{2.75}$$

and therefore

$$\varrho \in \mathbb{R} \iff x_2 < \frac{\bar{U}}{R_{v_k}}. \tag{2.76}$$

The same condition holds for $\Gamma : \mathbb{R} \to \mathbb{C} \iff x_2 < \frac{\bar{U}}{R_{v_k}}$. Thus, the only condition for the Jacobian $\boldsymbol{J}$ to be positive definite is given by

$$\Psi(x_2) > 0. \tag{2.77}$$

Using conditions in (2.76) and (2.75), the function $\Psi(x_2)$ can be approximated as

$$\Psi(x_2) \approx (\bar{U}^2 - R_{v_k}^2\, x_2^2)\Big(\frac{L_k R_{v_k} + 2R_k L_k}{(\bar{U}^2 - R_{v_k}^2\, x_2^2)^{\frac{1}{2}}} + 2\pi\, G_P \kappa\, L_k\, (L_k + 2\, L_L)\, x_2\Big). \tag{2.78}$$

Therefore, according to the condition in (2.76), $\Psi(x_2) > 0$ if the following holds true

$$R_{v_k} + 2R_k + 2\pi\, G_P \kappa\, (L_k + 2\, L_L)\, x_2\, (\bar{U}^2 - R_{v_k}^2\, x_2^2)^{\frac{1}{2}} > 0. \blacksquare \tag{2.79}$$

The results presented in Theorem 2 show that it is possible to design a virtual impedance with only a resistive component that could guarantee exponential convergence in systems with predominantly inductive loads. Theorem 2 shows that by using a virtual impedance, the contraction region could be expanded, as well as the ball radius inside of the region allowing a more relaxed convergence condition. At the same time, it is important to mention that according to (2.64) and (2.58), there should not be any voltage drop in the output voltage other than the voltage reference provided by the droop equation. This means that under reactive loads conditions, having virtual impedance with mostly resistive component guarantees not only exponential convergence and system stability, but also proper voltage regulation in the system; this is desired in a residential nanogrid operation, where voltage sags and swells are more noticeable and critical for the end user.

2.4 Numerical Analysis and Validation

In this section, two sets of results are presented. The first results correspond to the comparison of the closed-loop model developed in (2.67) against experimental and simulation results. The second set of results show the analysis and validation of the contraction region theorem presented in Theorem 2. In the latter, a specific

load condition is studied and an analysis over different values of R_{v_k} is presented. Experimental results validate the numerical analysis.

2.4.1 Experimental Setup

The experiments were performed using the setup illustrated in Fig. 2.6. It consisted of two Energy Storage Systems (ESS), ESS-1 and ESS-2. Each ESS consisted of a set of Li-Ion batteries and a single-phase inverter. The AC output of each system is connected to common connection in a breaker box where they are connected to an Inductive/Resistive load (RL load). The computers were used to provide the synchronization commands for initialization and the whole system operates as an islanded nanogrid. A Yokogawa DL850E ScopeCorder was used to record the output currents, voltages, active and reactive powers.

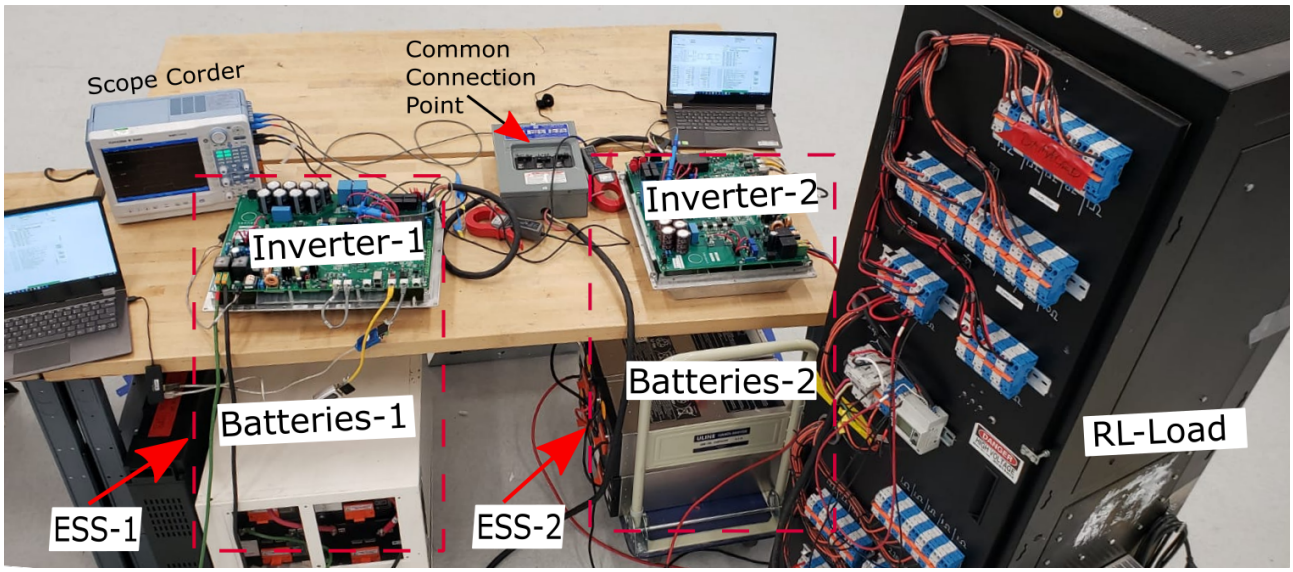

Figure 2.6: Experimental setup used in this study with the components labeled.

The systems parameters used for the numerical analysis in the next sections are shown in Table 2.1.

Table 2.1: System parameters

Parameter	Value	Parameter	Value
L_k	50 μH	R_k	10 $m\Omega$
$\bar{U}_k$	125 V	$\bar{\omega}_k$	376.99 rad/s
n_k	5e-4	m_k	5e-4
$\bar{P}_k$	0	$\bar{Q}_k$	0
G_P	0.2	ω_o	376.99 rad/s

2.4.2 Closed-loop Model Validation

The results obtained from the time-varying phasor closed loop model developed in this paper and presented in (2.67) are compared against real-time hardware and simulation results. The experimental results were obtained through the set-up presented in section 2.4.1. The simulation results were obtained using a Simulink model (full switching-model) which considers the switching operation of the inverters, as well as the dynamic behavior of the DC link capacitors and batteries.

Fig. 2.7 shows the system behavior when the virtual impedance parameters are set to $R_{v_k} = 0.5\ \Omega$ and $L_{v_k} = 4\ mH$. Output current (i_1) of inverter-1 is captured on the ScopeCorder channel 2 ($CH2$) and the output voltage (u_1) on channel 1 ($CH1$). The two inverters are synchronized at the beginning of the test, and then a load of $R_L = 1.5\Omega, L_L = 16.75mH$ is connected and disconnected 3.5 seconds later. The bottom plot is the zoomed area during the load connection moment. In this case, the current demanded by the inductive load is properly shared by the two inverters while there is a voltage sag from $176V_{pk}$ to $155V_{pk}$, around $20V$. The output voltage and output current dynamic is simulated using the closed-loop tvp model. Fig. 2.8 and Fig. 2.8 show the results of the tvp model compared against the full switching model and the real hardware results. Output voltage and output current are compared as well as the output active and reactive powers for inverter-1. The obtained results show how the proposed closed loop tvp model is able to produce results very close to the Simulink full-switching model, not only the steady steady state response, but also the transient response. Due to the ScopeCorder resolution, there is a small difference between the real hardware and the simulated transient behavior (not only for the tvp model, but also for the full-switching model), however, the steady behavior matches very closely for the three presented cases. With a root mean square error (RMSE) of 0.29 when compared against experimental results and 0.0783, when it is compared against the full switching model simulation.

Additional results are presented in Fig. 2.10 and 2.11, where the virtual impedance parameters are set to $R_{v_k} = 1\ \Omega$ and $L_{v_k} = 0$. Fig. 2.10 shows the output current and output voltage captured by an oscilloscope. It can be seen that in this case, despite having the same load conditions, the voltage remains almost constant or with minimal output voltage variation during the transient. This behavior supports the theoretical analysis obtained in (2.56) and (2.57) and the benefit of using only resistive virtual impedance with predominantly reactive loads. Additionally, Fig. 2.11 shows comparison of the output active power and reactive power among the three cases, tvp model, switching model and real hardware test. It can be observed how close the tvp model results are to the output of the full switching model during the transient and steady-state operation.

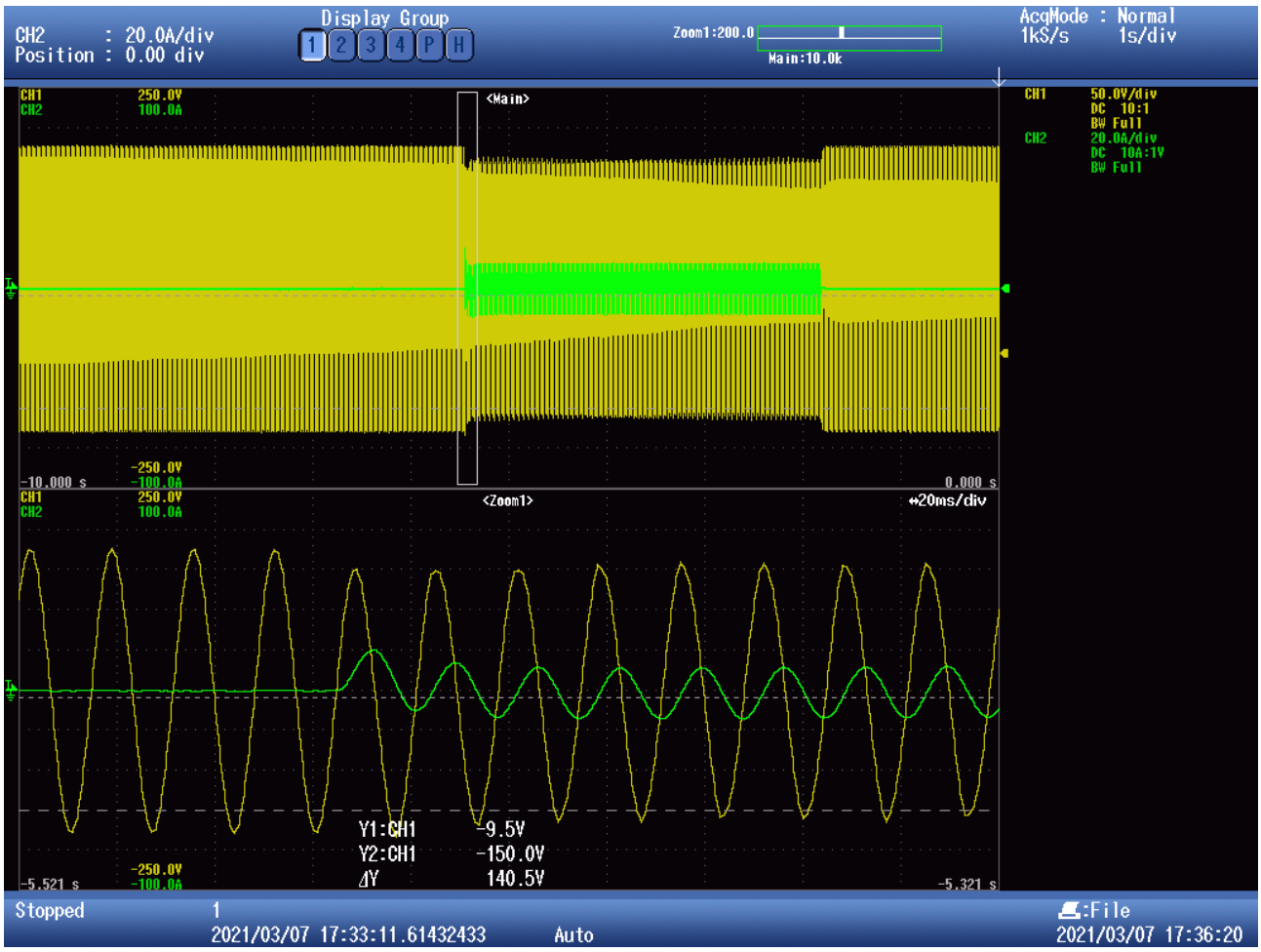

Figure 2.7: Inverter-1 system response. $R_{v_k} = 0.5\ \Omega$ and $L_{v_k} = 4\ mH$. Load transient of $L_L = 16.5\ mH$ and $R_L = 1.5\ \Omega$. $CH1$ Output voltage, u_1. $CH2$, Output Current, i_1.

Although there is a difference between the experimental results and the tvp model during the transient, which can be due to the scope-corder resolution used during the test, the steady-state values are very close for the three cases, and the plots suggest an exponential convergence for the three cases.

2.4.3 Examining the Contraction Regions Using Numerical Analysis and Experimental Validation

To validate the results obtained by Theorem 2, an analysis over the approximation of the contraction region for different values of R_{v_k} under no load conditions was performed. Such condition is introduced as a high load impedance parameter in the model. The approximated contraction regions for different trajectories close to the origin are depicted in Fig. 2.12. It can be observed that higher values of R_{v_k} expand the region. On the other side, lower values of R_{v_k} make the region smaller and therefore exponential convergence can

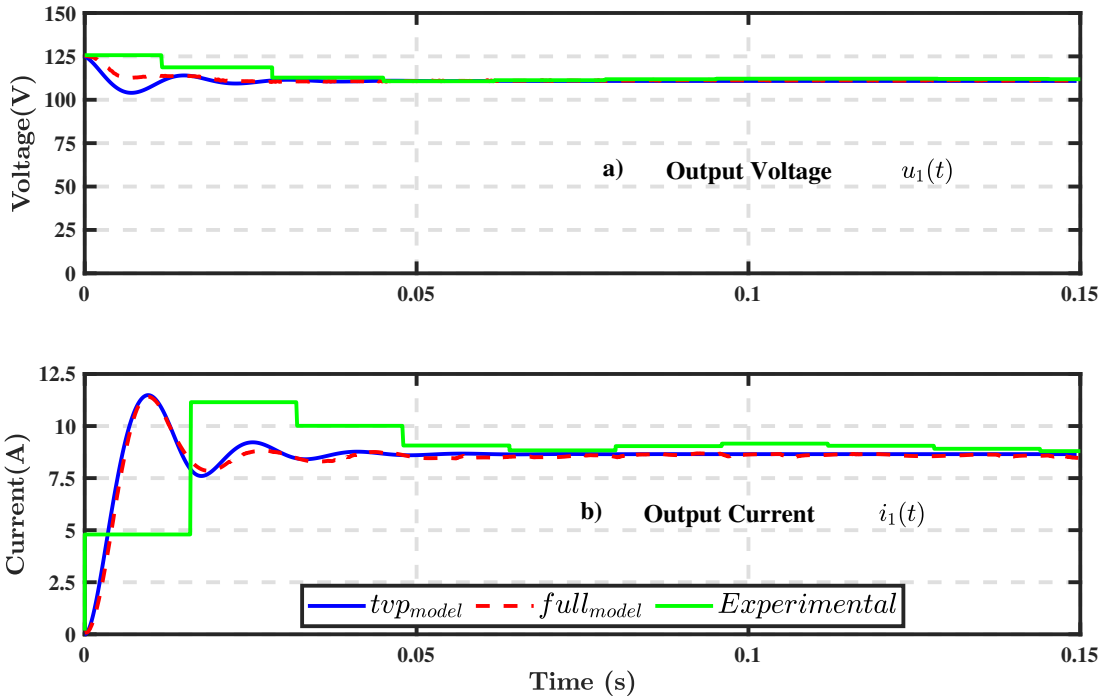

Figure 2.8: Comparison of tvp model, full switching model and real hardware results. $R_{v_k} = 0.5\ \Omega$ and $L_{v_k} = 4\ mH$. Load transient of $L_L = 16.5\ mH$ and $R_L = 1.5\ \Omega$. a) Time-varying RMS Output voltage, U_1. b) Time-varying RMS Output current, I_1.

only be guaranteed for trajectories that are in close vicinity to the origin. Thus, the larger the values of R_{v_k} are, the stronger criterion for exponential convergence for any trajectory will be.

The validation of the numerical analysis is confirmed through experimental results, which are presented in Fig. 2.13. Fig. 2.13-*a* shows the current response for $R_{v_k} = 0.5$. Here, the current signal oscillates around the equilibrium point because the exponential convergence criterion is limited to trajectories that are very close to o or to the origin. On the other hand, Fig. 2.13-*b* shows results after the virtual impedance increases to a very high value $R_{v_k} \gg 1$. Here, the convergence is not only exponential but also has a faster convergence rate due to a stronger stability criterion given by the expanded contraction region. Fig. 2.13-*c* shows an intermediate result for $R_{v_k} = 1$. Exponential convergence to the system equilibrium point is achieved but with a slower rate.

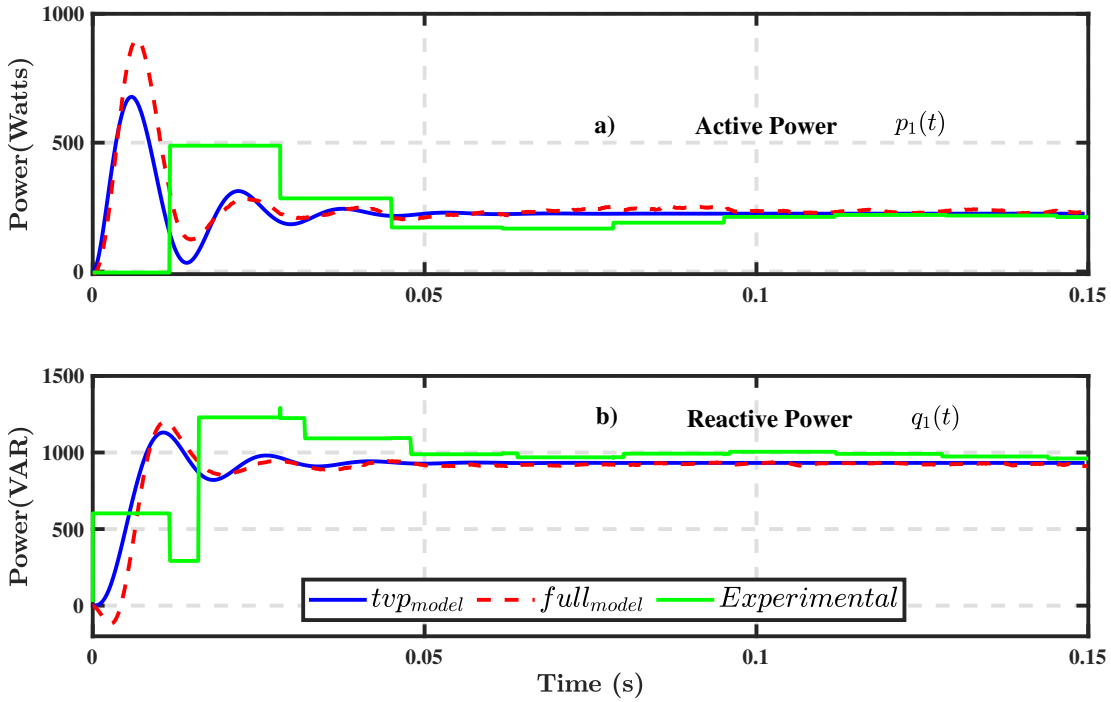

Figure 2.9: Comparison of tvp model, full switching model and real hardware results. $R_{v_k} = 0.5\ \Omega$ and $L_{v_k} = 4\ mH$. Load transient of $L_L = 16.5\ mH$ and $R_L = 1.5\ \Omega$. a) Active power, p_1. b) Reactive power, q_1.

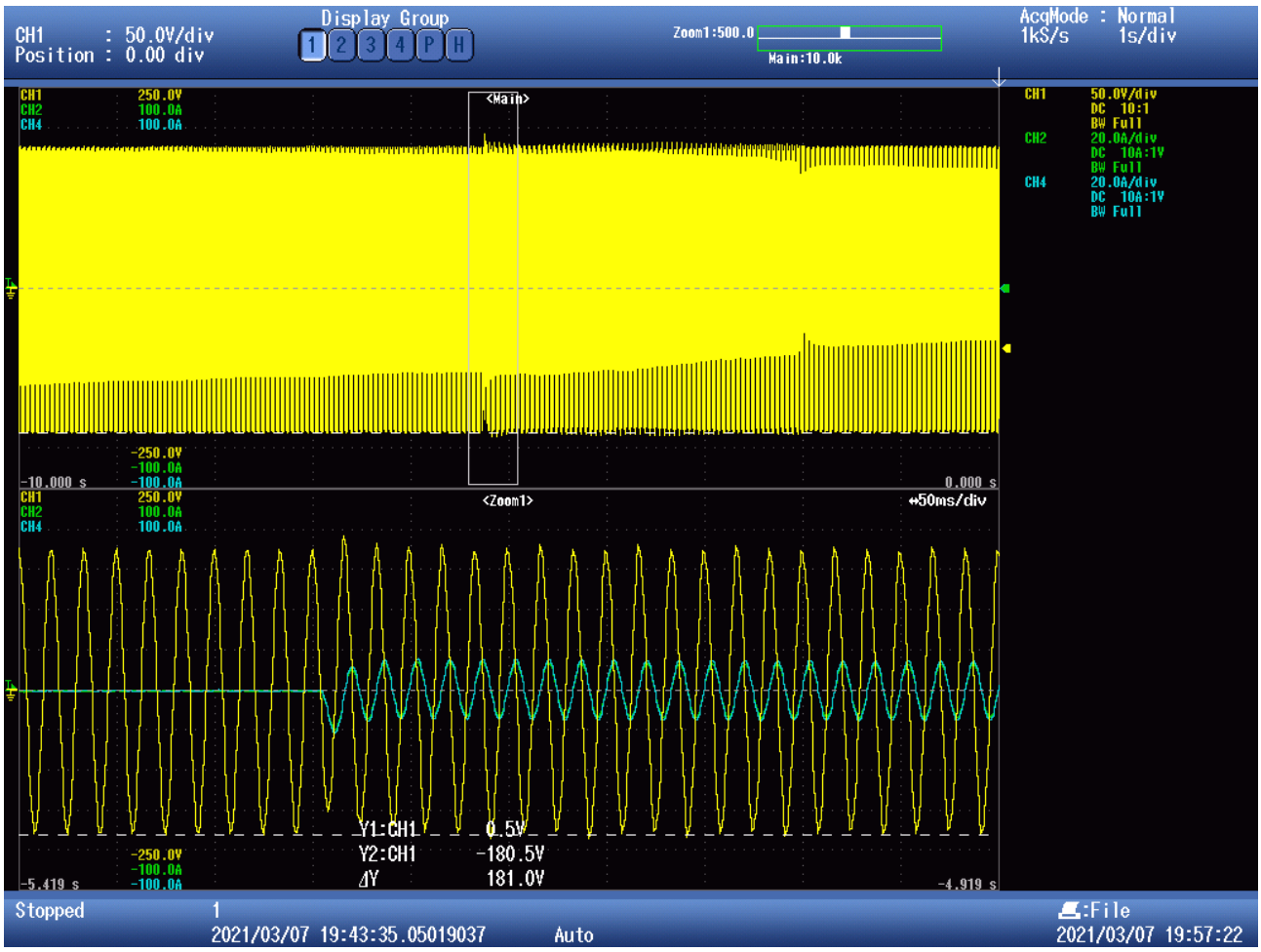

Figure 2.10: Inverter-1 system response. $R_{v_k} = 1\ \Omega$ and $L_{v_k} = 0$. Load transient of $L_L = 14.9\ mH$ and $R_L = 0.5\ \Omega$. $CH1$ Output voltage, u_1. $CH2$, Output Current, i_1.

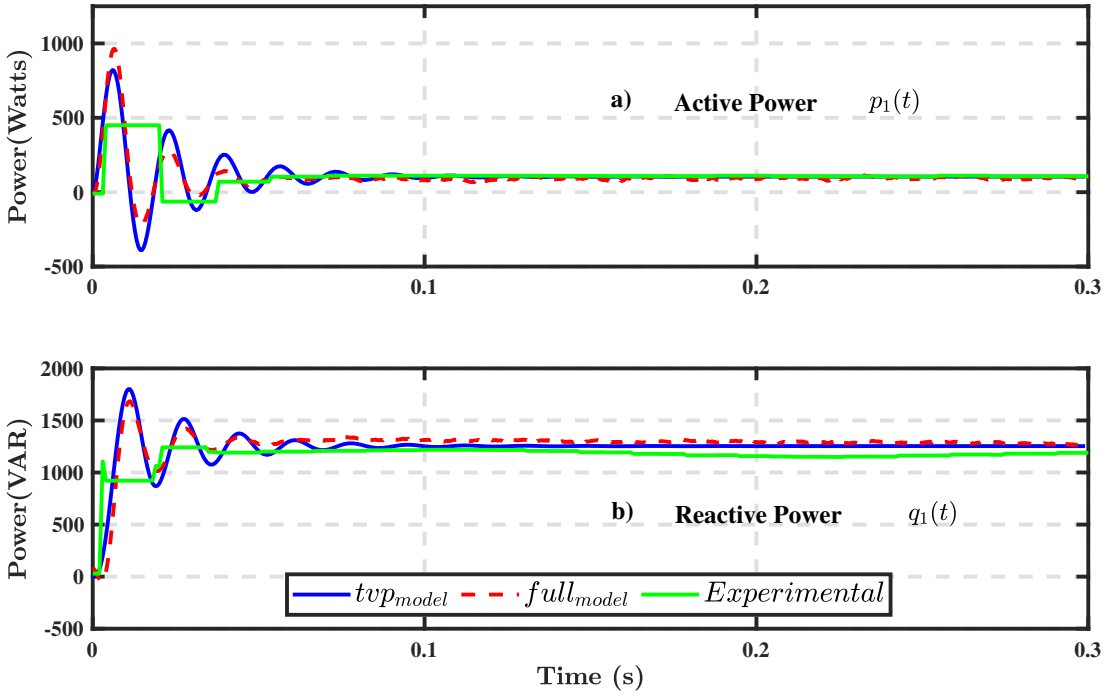

Figure 2.11: Comparison of tvp model, full switching model and real hardware results. $R_{v_k} = 0.5\ \Omega$ and $L_{v_k} = 0\ mH$. Load transient of $L_L = 14.9\ mH$ and $R_L = 0.5\ \Omega$. a) Active power, p_1. b) Reactive power, q_1.

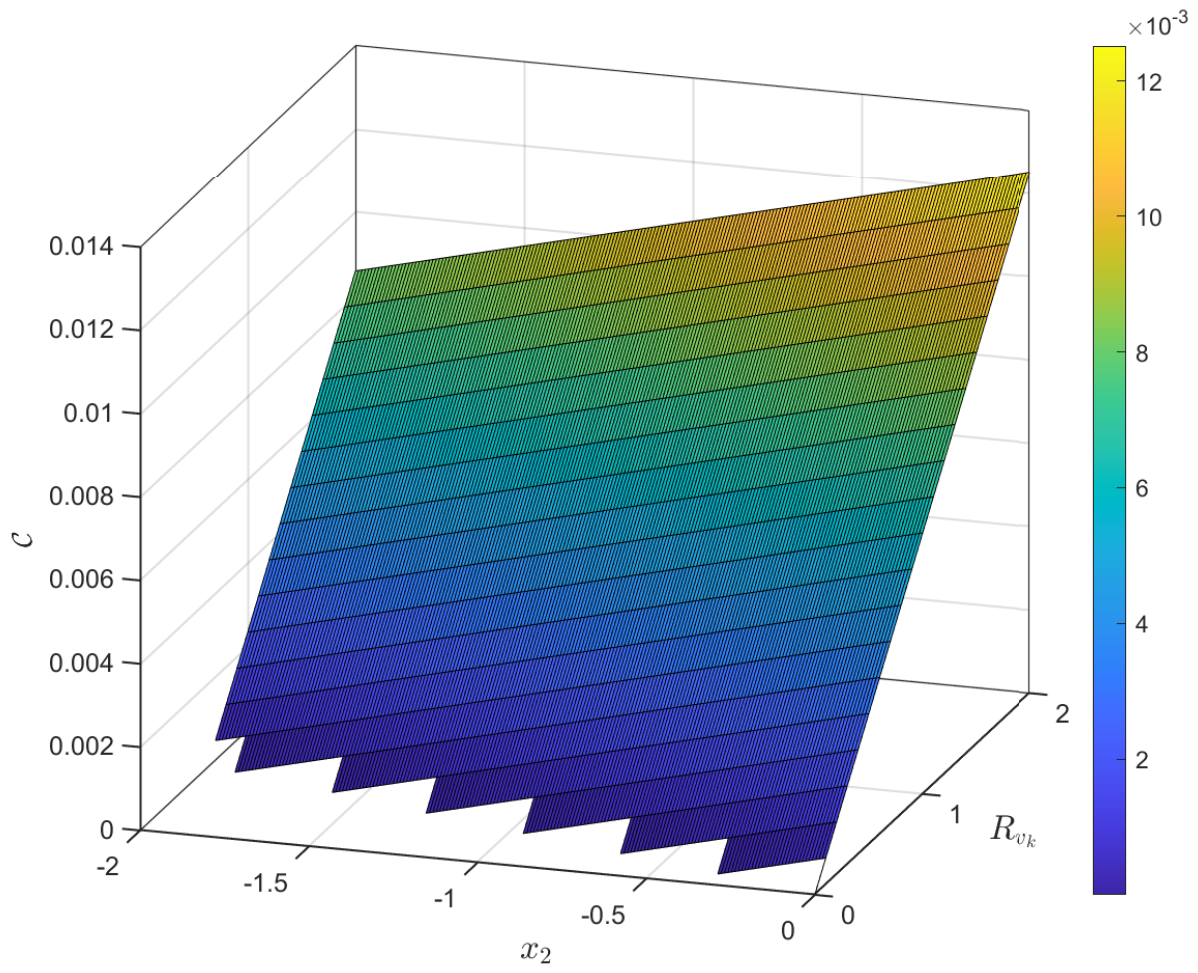

Figure 2.12: Approximated contraction regions for different values of R_{v_k}.

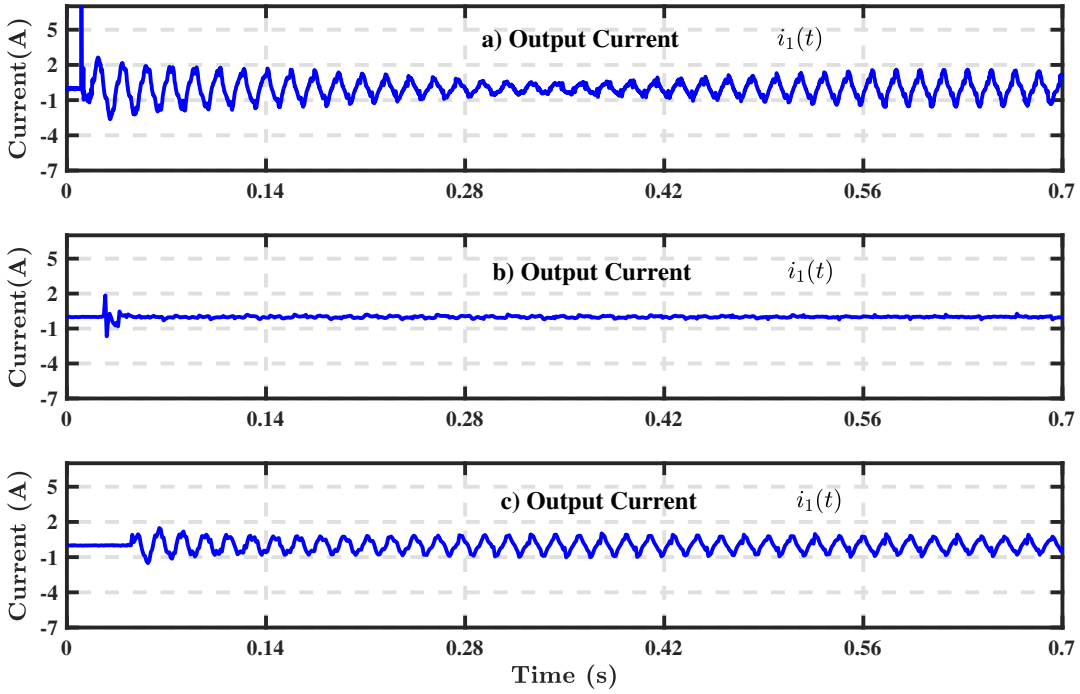

Figure 2.13: Hardware experimental results showing output current for different values of R_{v_k}: *a*) $R_{v_k} = 0.5$, *b*) $R_{v_k} \gg 1$, *c*) $R_{v_k} = 1$.

Chapter 3

Battery Storage in AC residential nanogrids

A partial content of this chapter has been published at ECCE 2017 [1], ECCE 2019 [2], and in the book Fault Diagnosis for Robust Inverter Power Drives, 2018 [3].

3.1 Battery Storage

3.1.1 Batteries Principle of Operation

In the last decade, the high penetration of renewable energy sources and the accelerated demand for Electric Vehicles (EVs) has resulted in the batteries to play a critical role in the worldwide energy future.

The chemical energy contained in batteries active materials is converted into electrical energy through an electrochemical oxidation-reduction (redox) reaction. This type of reaction involves the transfer of electrons from one material to another through an electrical circuit.

The operating principle of a single cell (the basic building block of a battery) is visualized in Fig. 3.1. Here, two electrodes (anode and cathode) are submerged in an electrolyte component, which provides the medium for the transfer of charge. During the electrochemical reaction, the anode is oxidized while it is giving

[1] A. Salazar, C. Restrepo, Y. Gao, J. M. Velni and A. Ginart, "An online LiFePO4 battery impedance estimation method for grid-tied residential energy storage systems," 2017 IEEE Energy Conversion Congress and Exposition (ECCE), Cincinnati, OH, USA, 2017, pp. 980-986, doi: 10.1109/ECCE.2017.8095892. Copyright ©2017, IEEE

[2] A. Salazar, A. Berzoy and J. M. Velni, "Nonlinear Control Design for Bidirectional Synchronous Buck-Boost Converters used in Residential Battery Storage Systems," 2019 IEEE Energy Conversion Congress and Exposition (ECCE), Baltimore, MD, USA, 2019, pp. 2485-2490, doi: 10.1109/ECCE.2019.8912221. Copyright ©2019, IEEE

[3] Llinas, Andres Salazar; Ginart, Antonio; Velni, Javad Mohammadpour: 'Battery storage' (Power and Energy, 2018), 'Fault Diagnosis for Robust Inverter Power Drives', Chap. 7, pp. 253-270, DOI: 10.1049/PBPO120E_ch7

up electrons to the external circuit; meanwhile, the cathode is reduced while accepting electrons from the external circuit. Depending on the type of electrolyte and cathode, the process can be reversible or not. Non-rechargeable batteries are known as primary batteries, whereas rechargeable batteries are called secondary batteries.

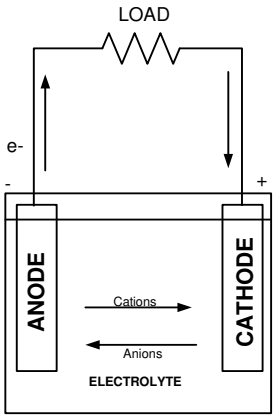

Figure 3.1: Basic operation of a single battery cell during discharge. Reproduced with permission from (Salazar et al., 2018).

The general advantages of primary batteries are good shelf life, high energy density at low to moderate discharge rates, and low maintenance (Batteries et al., 2004). Secondary batteries are characterized (in addition to their ability to be recharged) by high power density, high discharge rate, flat discharge curves, and good low-temperature performance (Batteries et al., 2004). Secondary batteries can also be classified by the type of chemistry they use. Among the most common one are:

- Lead-acid batteries: This was the first battery type that could be recharged by passing a reverse current through it. The lead-acid battery uses lead dioxide (PbO_2) as the active material of the positive electrode, and metallic lead (Pb) in a high-surface-area porous structure as the negative active material. The electrolyte is a sulfuric acid solution:

$$\mathrm{Pb + PbO_2 + 2\,H_2SO_4} \xrightarrow{\text{discharge}} \mathrm{2\,PbSO_4 + 2\,H_2O}$$
$$\mathrm{Pb + PbO_2 + 2\,H_2SO_4} \xleftarrow{\text{charge}} \mathrm{2\,PbSO_4 + 2\,H_2O}$$

  Lead-acid batteries can be found in Energy Storage Systems (ESSs), emergency power systems, and electric and hybrid vehicles. They are also used in combustion engine vehicles' lighting and engine ignition circuits.

- Nickel-cadmium batteries: This is the most popular type of alkaline secondary batteries. The charge/discharge mechanism in the alkaline electrolyte involves only the transport of oxygen or hydroxyl ions from one

electrode to the other; hence, the concentration of the electrolyte does not change during charge and discharge. Nickel-cadmium (NiCd) batteries are found in different design forms and sizes, such as sealed pocket plate and vented pocket plate. The reactions of charge and discharge can be illustrated by the following simplified equations:

$$2\,NiOOH + 2\,H_2O + Cd \xrightarrow{\text{discharge}} 2\,Ni(OH)_2 + Cd(OH)_2$$
$$2\,NiOOH + 2\,H_2O + Cd \xleftarrow{\text{charge}} 2\,Ni(OH)_2 + Cd(OH)_2$$

The main application of NiCd is with cordless electronic tools. It is also used in applications, such as aircraft engine starting, as well as communications and electronics equipment.

- Lithium-ion batteries: These are the most popular type of secondary batteries nowadays. Lithium-ion (Li-ion) batteries are comprised of cells that employ lithium intercalation compounds as the positive and negative materials. The positive electrode material is typically a metal oxide with a layered structure, such as lithium cobalt oxide ($LiCoO_2$), or a material with a tunneled structure, such as lithium manganese oxide ($LiMn_2O_4$), on a current collector of aluminum foil. The negative electrode material is typically a graphitic carbon, also a layered material, on a copper current collector. In the charge/discharge process, lithium ions are inserted or extracted from interstitial space between atomic layers within the active materials.

  Applications for Lithium-ion batteries range from commercial electronics, such as cell phones and laptops, to Electric Vehicles (EVs) and Energy Storage Systems (ESSs).

This chapter focuses on lithium-ion batteries. It also covers relevant aspects of this technology, focusing on the Impedance Measurement as a diagnostic tool mechanism for detecting aging on this type of batteries. Furthermore, we divide such mechanisms into online and offline methods based on their means of operation during the service time of the battery.

Important Parameters of Batteries

- Capacity. This measures the amount of charge that the battery can deliver at the rated voltage. It is measured in Ampere hours (Ah). The Energy Capacity relates the capacity to the battery voltage, and it is measured in Watt-hours (Wh).

- C-Rate. This is a measure of the rate of the battery's discharge relative to its capacity. It is defined as the multiple of the current over the discharge current that the battery can sustain over one hour. The C-rate of 1 for a 10 Ah battery corresponds to a discharge current of 10 A over 1 hour.
- SoC. This measures the percentage of the battery capacity available for charging or discharging.
- Power. This describes the capability of the battery for charge or discharge at a specific current level. There are two parameters to describe power: (1) Power Density: Power per volume, and (2) Specific Power: Power per weight. Depending on the application, one of these might be more important than the other. For example, for a cell phone, the power density is more important, whereas for an electric vehicle, specific power has more value.
- Cycle Lifetime Aging. It is defined as the number of charging and discharging cycles after which the battery capacity drops below 80% of the nominal value.
- Calendar Life Aging. Calendar aging comprises all aging processes that lead to a degradation of a battery cell independent of charge-discharge cycling.

3.1.2 Li-ion Batteries

Lithium-ion cells are composed of four components: a positive electrode, a negative electrode, an electrolyte, and a separator in between them. The positive electrode is made of a metal oxide material (such as lithium cobalt oxide LiCoO2), a material with a tunneled structure (such as lithium manganese oxide LiMn2O4), or a material with an olivine structure (such as lithium iron phosphate LiFePO4). The negative electrode is built up of carbon (graphite), and the electrolyte varies depending on the type of battery technology. The separator prevents physical contact between the anode and the cathode, while facilitating ion transport in the cell (Wakihara et al., 1998), (Pistoia, 2013). Throughout the charge process of the battery, the lithium positive electrode pulls out some of its lithium ions, which move through the electrolyte to reach the negative electrode and remain there. When the cell is discharging, the lithium ions move back across the electrolyte to the positive electrode, producing the energy required by the load connected to the battery. In both cases electrons flow in the opposite direction from the ions around the outer circuits. Electrons do not flow through the electrolyte, which behaves as an insulating barrier for them. The flows of ions (through the electrolyte) and electrons (around the external circuit, in the opposite direction) are interconnected processes, and if either one of them stops, the other also stops. If ions stop moving through the electrolyte because the

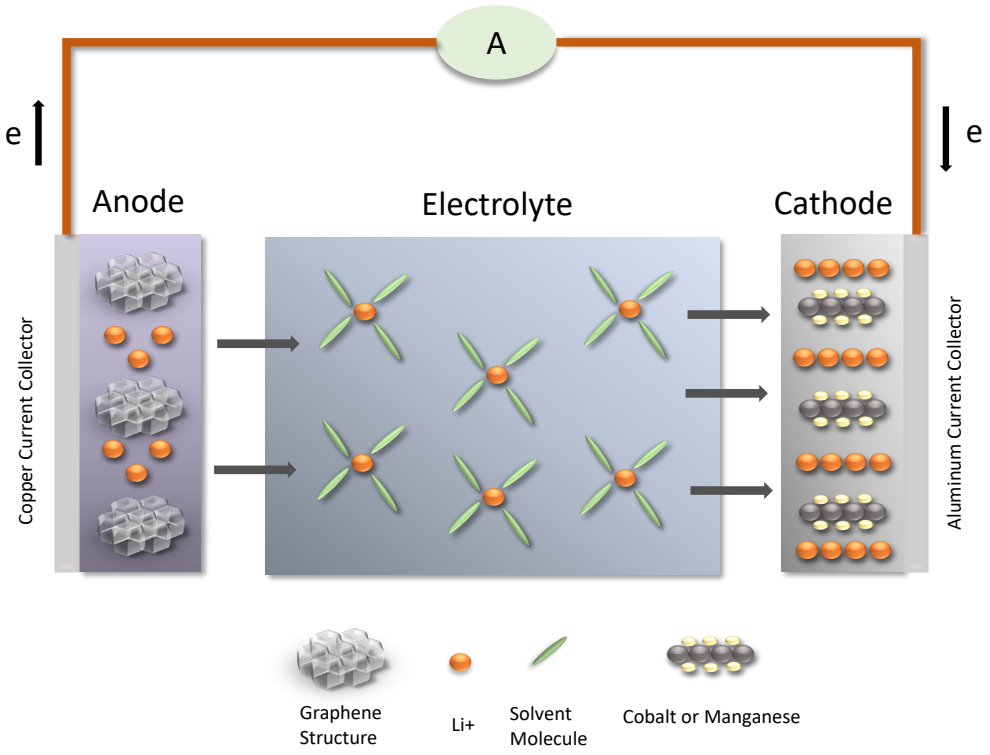

Figure 3.2: Discharging process of a lithium-ion cell (Adapted from (Wakihara et al., 1998)). Reproduced with permission from (Salazar et al., 2018).

battery completely discharges, then the electrons cannot move through the outer circuit either, so the power is lost. Furthermore, at no-load conditions, the electron flow stops and consequently the flow of ions also stops, forcing the battery to stop discharging. (Fujisawa, 1989)

Evolution of Cathodes Technologies: It took around 30 years to reach the basis of what we know today as commercial rechargeable high-energy density Li-ion batteries. The research of different compounds and materials to improve the efficiency and power density of the cell started in early 70s, when Matsushita introduced a lithium-carbon monofluoride (Li-CFx) primary cell. In 1975 Sanyo was the first company to commercialize lithium-manganese dioxide cells (Li-Mn2). It was a not rechargeable cell but was able to produce a voltage of 3.5 V. The basic usage of these cells was for cameras and memory backup applications. In the following years great efforts were made to convert lithium cells into rechargeable cells with high energy density. Different materials were studied, without achieving any competitive advantage, except by the Polyacene (PAS) battery, for which the main use was in the production of coin cells for memory backups (Wakihara et al.,

1998). Between 1973 and 1976, Whittingham at Exxon developed a novel material for the cathode based on a titanium disulfide cathode and started the principle of lithium-ion rechargeable batteries, which he called Intercalation compounds. Exxon commercialized this first rechargeable battery with a lithium-aluminum anode, but its low-voltage profile (only around 2 V) made it insufficient for many applications (Pistoia, 2013). In 1980, Goodenough developed the Li-Cobalt Oxide as a cathode material at Oxford. This new compound offered a higher energy density than lithium-ion cells (Wakihara et al., 1998). The applications and market were not foreseen at that time, and it was only in 1991 when Sony, using the developments made by Yoshino (Fujisawa, 1989), started the commercialization of the first rechargeable $LiCoO_2$ battery. The cell was based on the Goodenough discovery but with the addition of a carbonized material in the anode. Another cathode structure was developed in 1983 at Oxford within the Goodenough research group. Later, Thackeray developed the structure called spinel and used a compound based on manganese dioxide MnO_2 (Thackeray et al., 1983). This new compound would offer price advantages over the cobalt compound; however, its lower capacity and stability issues gave priority to $LiCoO_2$, enabling the latter to take over the market. In 1997, Goodenough, this time with the Univ. of Texas at Austin, developed a new material for the cathode: Li-ion Iron Phosphate ($LiFePO_4$). This material gave the cell better stability, flattening the discharge characteristic profile and bringing the following advantages (Padhi, 1997):

- High output performance with standard discharge for 2 to 5C and continuous discharge high current capacity of up to 10C and the instantaneous discharge pulse up to 20C.
- Good performance is observed at high temperatures from 65 to 95 degree Centigrade keeping the battery in good safe condition.
- It shows excellent life cycles as after 6000 cycles also it shows discharge capacity to be above 80%. [10]
- It gets quickly charged with much less time compared to other batteries.
- It is an environmental-friendly battery which does not produce any waste.

Although the advances in new materials for anode and cathode are being made in different laboratories around the world, commercially speaking, $LiCoO_2$ and $LiFePO_4$ are the leading technologies for EV and grid energy storage systems.

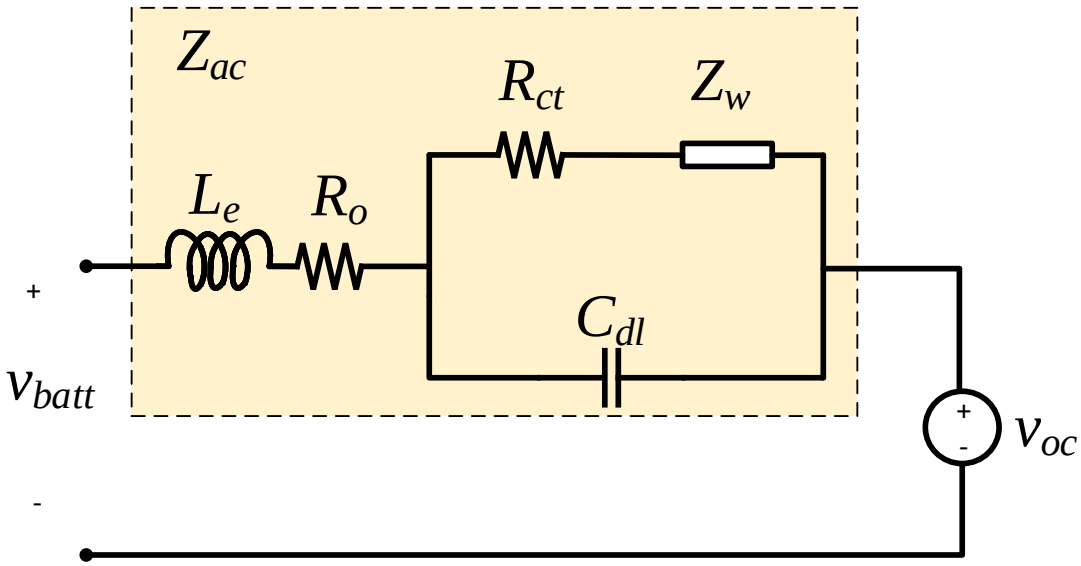

Figure 3.3: Li-ion cell electrical circuit representation. Reproduced with permission from (Salazar et al., 2018)

3.1.3 Electrical Model of Li-ion Batteries

Fig. 3.3 illustrates a suitable AC impedance model for a battery, with specific characteristics parameters for Li-ion. The components of this circuit are as follows: (1) parasitic inductor L_e; (2) ohmic resistance R_o; (3) charge transfer resistance R_{ct}; (4) double-layer capacitor C_{dl} as a result of activation polarization; and (5) Warburg impedance Z_w as a result of concentration polarization (Cho et al., 2016). The battery AC impedance Z_{ac} can then be expressed as follows:

$$Z_{ac}(\omega) = jL_e\omega + R_o + (R_{ct} + Z_w)\|\frac{1}{jC_{dl}\omega}. \tag{3.1}$$

A Nyquist plot for the battery impedance is shown in Fig. 3.4. Normally, this plot is obtained by an Electrochemical Impedance Spectroscopy (EIS) analysis, measuring the phase displacement between current and voltage when an oscillatory current, at different frequencies, is injected into the battery. The parameters in (3.1) can be estimated by different techniques as described in (Stroe, Swierczynski, Stan, et al., 2014) and (Tang et al., 2011). In the middle frequencies, the effect of the Warburg impedance and the inductance component are not that evident; hence, for injected currents with frequencies in that range, the AC impedance can be modeled as:

$$Z_{ac}(\omega) = R_o + (R_{ct}\|\frac{1}{jC_{dl}\omega}). \tag{3.2}$$

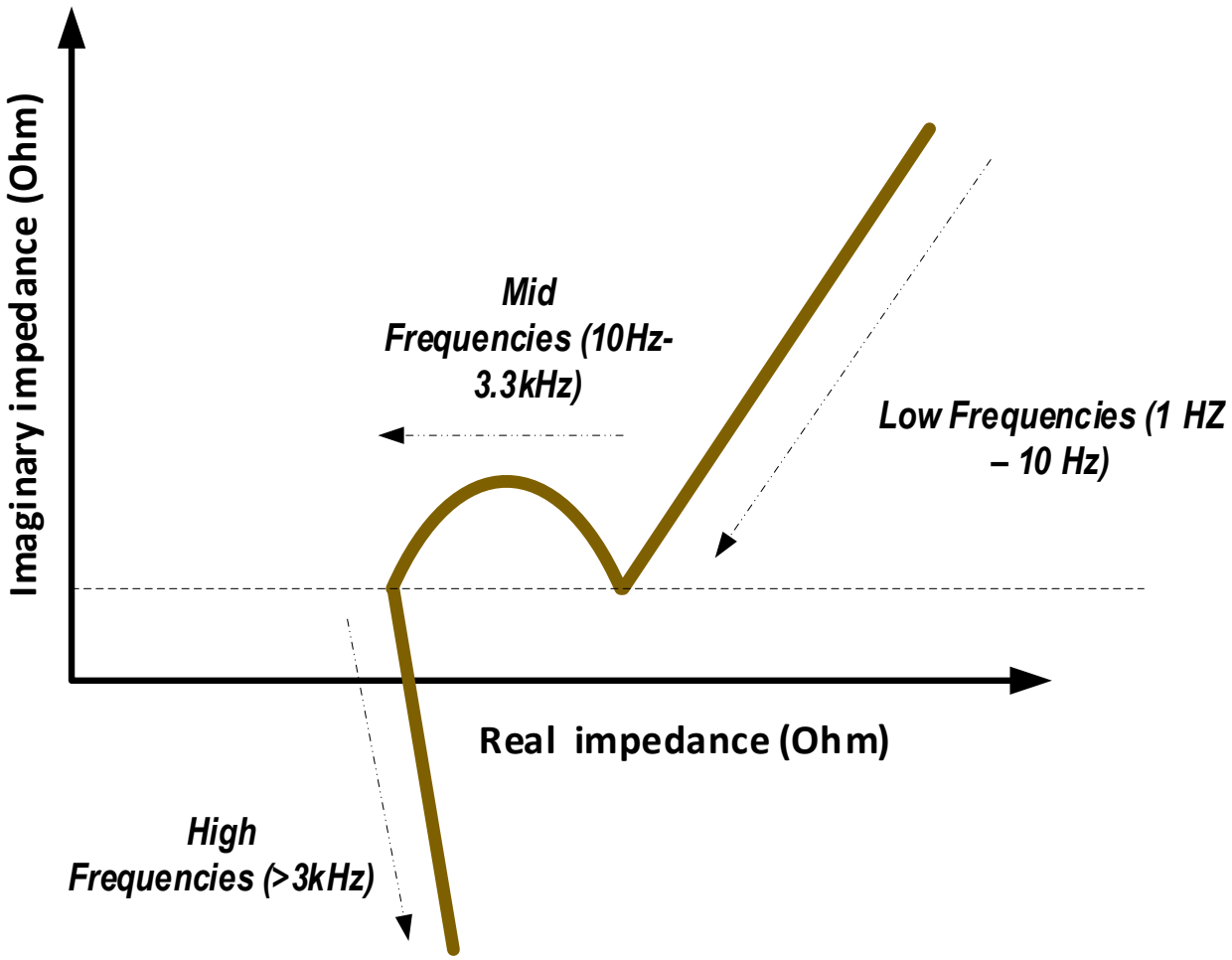

Figure 3.4: Nyquist plot representation for the AC-battery impedance. Reproduced with permission from (Salazar et al., 2018)

3.1.4 Aging of Li-Ion Batteries

We distinguish between two types of aging happening in a battery: cycle aging, occurring mainly due to regular battery operation, and calendar aging, occurring even if the battery is not under operation. Some of the consequences of aging in Lithium-ion batteries are described below.

Corrosion in the copper collector may lead to contact loss and hence to an increase in the contact resistance. At the same time, the anode will start changing its morphological structure due to cycle aging. Due to high charging/discharging currents in combination with low temperatures, the Li+ ions cannot intercalate fast enough into the anode material, and lithium deposits are formed on the graphite surface. The growth of these deposits and the formation of dendrites can destroy the separator, leading to thermal runaway in the cell. Over the cycle life of the battery, formation of a solid-electrolyte interphase (SEI) occurs typically

at the negative electrode during recharging. Initially, SEI formation protects the electrode against solvent decomposition at large negative voltage, but over time it leads to a gradual decrease in capacity as the SEI layer thickens. Above a certain threshold, films become resistive, which is considered an aging effect. On the other hand, decomposition of the SEI can result in lithium corrosion and thus in irreversible energy loss. Especially at high temperatures (≥60 degree Celsius), the SEI layer begins to decompose, causing the anode's passivation to fail. Similarly to the anode, the current collector suffers from corrosion; furthermore, changes in the cathode morphology and decomposition of the binder are some of the effects resulting from cycle aging of the cell (Schlasza et al., 2014).

The quantification of the current battery life is described by the state of health (SOH). This factor can be studied from two different points of view: first, by comparing the actual capacity of the battery to the capacity of a new battery and expressing this in a percentage. Normally, when the capacity decreases to 80% of the manufacturer's rated capacity, the battery is considered to be at the end of its operational life. Second point of view is achieved by means of measuring the internal resistance. An increase of the internal resistance resulting from aging effects in the cell leads to a reduction of the battery's power capabilities.

Method for Detection of Aging in Batteries using Impedance Measurement

It has been shown in previous studies that the real (or ohmic) part of the battery increases with the increase of battery life cycles (Stroe, Swierczynski, Stan, et al., 2014), (Micea & Ungurean, 2011). Fig. 3.5 shows a typical Nyquist plot of a Li-ion battery at the beginning of and end of its life. This illustrates that it is possible to examine the battery lifetime by measuring the battery impedance.

There exist different ways to measure the battery impedance in order to determine the SOH. The majority of those methods are based on the measure of voltage and current in the battery and the calculation of the battery impedance as

$$Z(\omega) = \frac{V(\omega)}{I(\omega)}. \tag{3.3}$$

We can distinguish between two methodologies for measuring the battery impedance. Offline methods are based on a parameter estimation of the battery packs or cells while they are not operational. The measurement occurs after the battery is neither charging nor discharging, and the parameters are fitted using the battery electrical model. On the other hand, online methods are used while the battery is operating, meaning that non-interruption of the charge/discharge process is needed. These methods are more suitable for implementation as part of the Battery Management System (BMS) algorithms. The aging is then detected by comparing

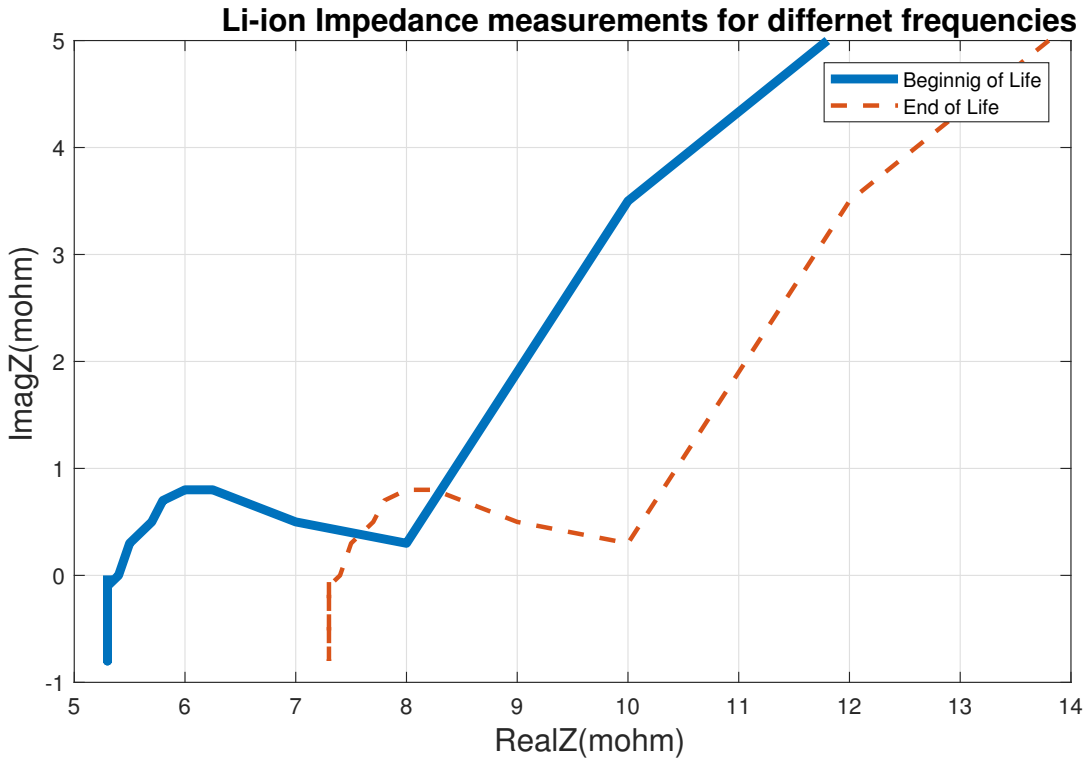

Figure 3.5: AC-battery impedance before and after aging. Reproduced with permission from (Salazar et al., 2018)

the baseline impedance measurement at the beginning of the battery life against the obtained impedance calculation, as shown in (3.4), where R_{eol} is the resistance at the end of life, R_{bol} is the resistance at the beginning of life and R is the measured resistance.

$$SOH_R = \frac{R_{eol} - R}{R_{eol} - R_{bol}}. \tag{3.4}$$

Online Measurement Methods

Online methods are characterized by exploiting the characteristics of the systems in which the batteries are used. These methods are mainly applicable and suitable for EV applications or ESS applications in which online prognosis of the batteries is used for determining levels of system maintenance.

Quasi-Electrochemical Impedance Spectroscopy (QEIS): QEIS is a novel alternative to the EIS. In QEIS, high-frequency oscillations occurring in the battery current, and voltage during acceleration and regenerative braking in EVs, are exploited to perform the impedance measurement across the frequency spectrum. Contrary to EIS, QEIS does not perform a periodical current or voltage perturbation. The method

instead uses the real current and voltage values of the module during an in-use load cycling scenario as input data in order to calculate an impedance spectrum, or so-called QEIS, which could be fitted to an equivalent electrical circuit model (Mingant et al., 2016):

$$Z(\omega) = \frac{V(\omega)}{I(\omega)} = \frac{\frac{2}{T}V(\omega) * I(\omega)}{\frac{2}{T}I(\omega) * I(\omega)} = \frac{\psi_{IV}(\omega)}{\psi_I(\omega)}, \tag{3.5}$$

where ψ denotes the power spectral density (PSD).

Motor Control Excitation: This method is also suitable for EV applications. It uses an excitation current generated by a motor controller. To mitigate the presence of noise in the measurement signals, a statistical correlation approach is used. The excitation in the current signal comes from variations in either the main traction current to the driver or the controller response. Authors in (Howey et al., 2014) demonstrate the capability of this method by obtaining the impedance measurement in the presence of noise in the measurement signals and then applying a QEIS for calculating the impedance spectrum.

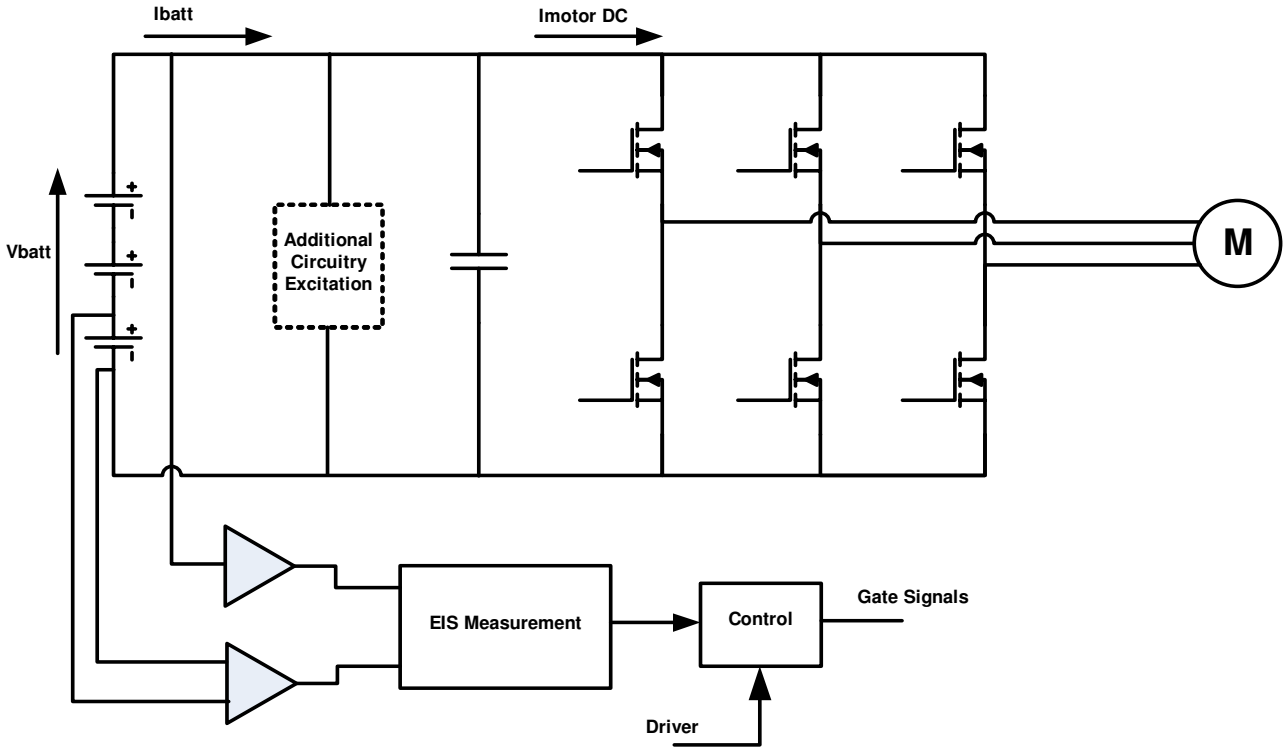

Figure 3.6: Battery impedance using motor control excitation. Adapted from (Howey et al., 2014). Reproduced with permission from (Salazar et al., 2018)

Duty Cycle Perturbation in DC/DC Converter: This battery impedance measurement is performed during system operation. In this method, instead of injecting the AC signal through an external generator,

the duty-cycle value of the DC/DC power converter, which is used to interface the battery with the load, is sinusoidal perturbed at a given frequency around its steady-state DC value (the duty-cycle value needed to achieve a desired output voltage). This duty-cycle perturbation results in sinusoidal variations of the battery voltage and the battery current around their corresponding steady-state DC values as

$$d(t) = D_{dc} + D_{ac}\sin\left(\omega_p t\right), \tag{3.6}$$

where ω_p is the perturbation signal frequency. The sinusoidal ripple of the battery voltage and the battery current are then measured and used to determine the AC impedance of the battery at the perturbation frequency. The proposed method can be either continuously or periodically performed without interrupting the normal operation of the battery system and the power converter. Fig. 3.7 and Fig. 3.8 show respectively the circuit and waveforms presented in (Huang & Qahouq, 2014) (Qahouq, 2016) to demonstrate the efficiency of the method.

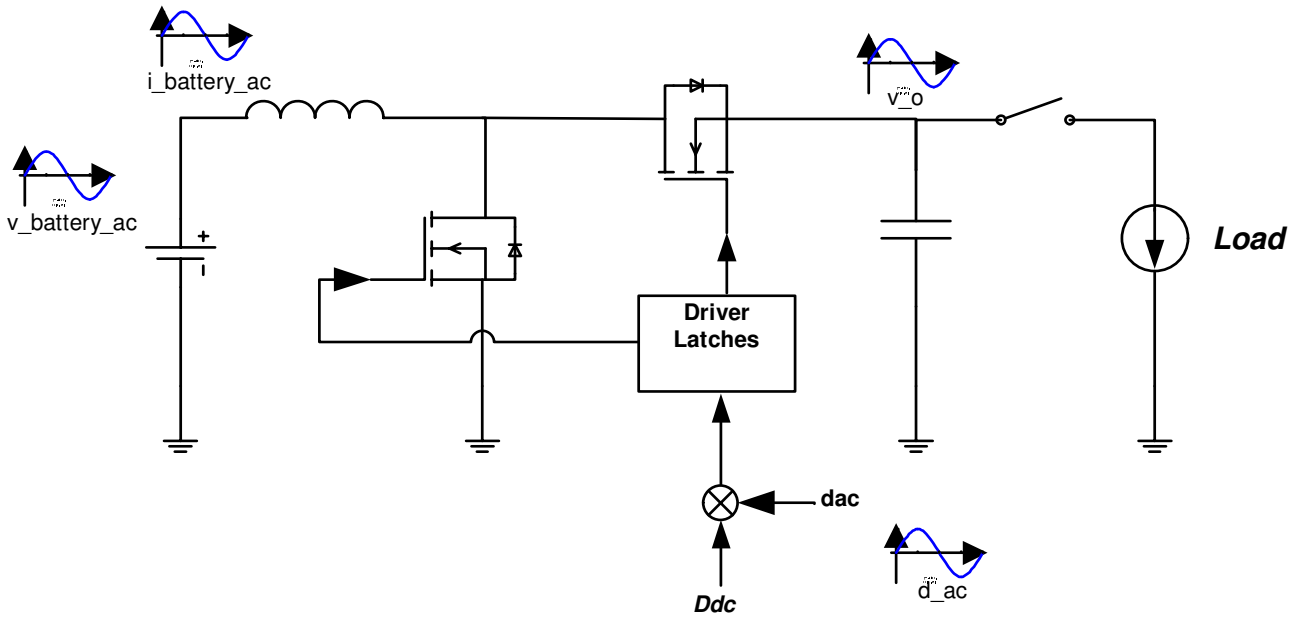

Figure 3.7: Duty cycle perturbation in DC converters. Adapted from (Huang & Qahouq, 2014). Reproduced with permission from (Salazar et al., 2018)

3.2 Residential Bi-directional Inverters and Control Schemes

Grid-tied battery storage systems (BSS) consist of a rechargeable energy source module, a grid-tied inverter and a charge controller. The latter controls the charge and discharge of the battery while protecting the battery electro-chemistry, whereas the inverter serves as the interface between the batteries and mains for the

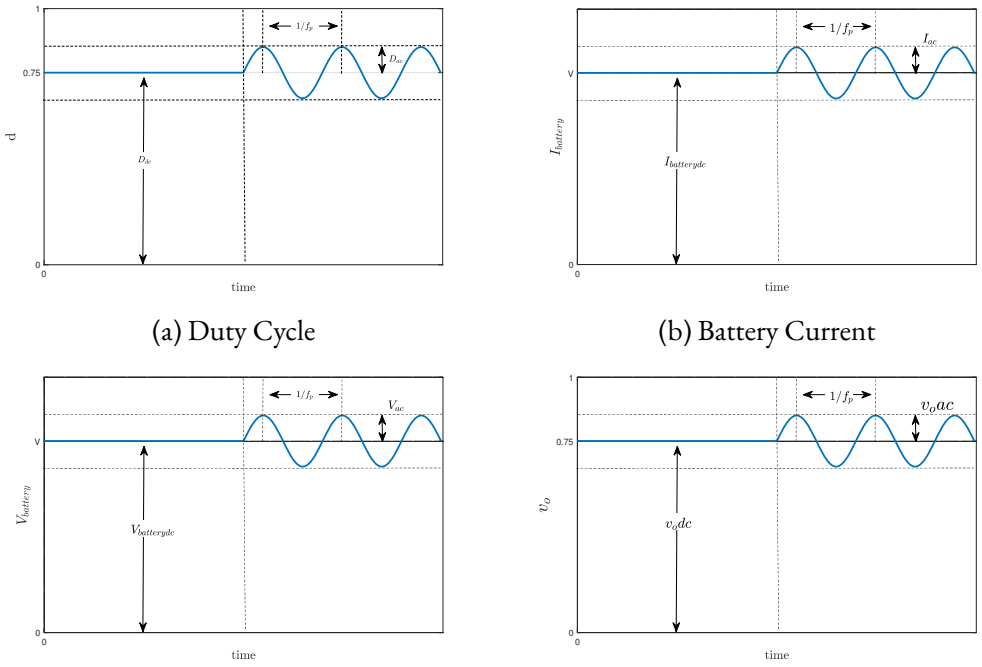

(a) Duty Cycle

(b) Battery Current

(c) Battery Voltage

(d) Output Voltage

Figure 3.8: Battery impedance measurement using duty-cycle perturbation. Adapted from (Huang & Qahouq, 2014). Reproduced with permission from (Salazar et al., 2018)

power transfer. Generally, a residential battery storage system faces challenges associated with single-phase systems, such as a pseudo-pulsating power transfer, in addition to those related with bidirectional capabilities and ancillary services. Also, the U.S. split-phase power system has created a need for inverters capable of supporting two phase unbalanced loads with center tap grounded operation. Moreover, the BSS typically offers the advantage to work on back-up mode in situations where the national grid is absent (Berzoy et al., 2019). Latest advancements in semiconductor technology have allowed the use of transformer-less inverters for these systems. Commercially available transformer-less inverters utilize bidirectional dc/dc converters for avoiding the use of battery modules in series and the separation of the control activities (Ginart et al., 2016). The former reason establishes a cost-effective system while the latter decreases the system complexity.

The most common type of control scheme for bidirectional dc/dc converters is based on proportional-integral (PI) controllers, which allow to track an output voltage reference in the presence of load disturbances. However, the system operation for charging or discharging the batteries varies unpredictably which results in highly nonlinear characteristics (Wang et al., 2014). Therefore, the use of nonlinear control schemes has been exploited to overcome the underlying challenges and improve the system performance. In (Wang et al., 2014), a time delay control (TDC) is implemented for a lithium-ion battery applications, when linear dc loads are

considered. In (Fadil et al., 2012), a back-stepping design technique is used to optimally control the voltage of a boost converter for photovoltaic (PV) applications. A back-stepping design technique is also used in Abouloifa and Giri, 2004 for regulating the output current for a buck-boost ac/dc converter while correcting the power factor at the ac connection point. Sliding mode control is applied in (Benadero et al., 2015) for a bidirectional dc/dc power converter to control the dc bus voltage in a dc microgrid, considering a constant power load. It is noted that the results presented in (Abouloifa & Giri, 2004; Benadero et al., 2015; Fadil et al., 2012) are merely based on circuit simulations.

Feedback linearization (FBL)-based control approaches have been employed in different mechanical and electrical systems. Several publications show its applicability in power converters. In (Solsona et al., 2015), the authors formulate a feedback controller based on FBL combined with a feed-forward strategy to control a dc/dc buck converter. The authors in (Mahmud et al., 2014) propose a controller using partial FBL and guarantee the robustness of this control scheme by considering structured uncertainties within a renewable energy system (RES). In (Perez et al., 2018), a dynamic FBL control strategy is proposed to regulate the voltage on the dc bus for a dc microgrid. The work in (Zheng & Shuai, 2012) proposes the use of FBL for controlling the output voltage of a boost converter connected to a resistive load, and simulation results are shown and compared against other nonlinear control design techniques such as passivity-based control. Finally, in (Callegaro et al., 2018), a nonlinear controller is designed for PV modules integrated with dc/dc converters.

3.3 Online Battery Impedance Estimation

Non-perturbing Method for Residential ESS: The most recent online method for estimating a Li-ion battery AC impedance at twice the fundamental grid frequency has been proposed by the authors of this chapter. The proposed method presented in (Salazar et al., 2017) does not require perturbing the power electronics control of the inverter used in AC nano-grid applications interacting with the AC power grid through single-phase inverters. This method differentiates from those found in the literature, because those methods focus only on EVs and other DC applications in which no interaction with AC sources is required. Furthermore, the above methods involve the use of a perturbation in the power electronics duty cycle, and hence require modifying the closed-loop control of the power converters. A single-phase power system experiences a pulsating power transfer between the batteries and the AC source, which can be computed

based on the energy conservation principle as

$$p_{DC}(t) = i_{DC}(t)\, v_{DC}(t) = \eta\, i(t)\, v(t) = p_{AC}(t). \tag{3.7}$$

Assuming that the efficiency η and the power factor are equal to one, the instantaneous values for the current and voltage are obtained from (3.8), where $\omega_0 = 2\pi f_0$ and f_0 is the fundamental frequency of the power grid (Ginart et al., 2016):

$$v_{DC}\, i_{DC} = \sqrt{2} V_{RMS} \sin(\omega_0 t)\, \sqrt{2} I_{RMS} \sin(\omega_0 t) = 2 V_{RMS} I_{RMS} \sin^2(\omega t). \tag{3.8}$$

As a result, the battery DC current should have a quadratic sine form as

$$i_{DC}(t) = \frac{2 V_{RMS} I_{RMS} \sin^2(\omega_0 t)}{v_{DC}}. \tag{3.9}$$

A plot of $I_{DC}(t)$ is shown in Fig. 3.10. Assuming no losses in the power conversion process, the battery DC current can be rewritten as

$$i_{DC}(t) = 2 I_{DC} \sin^2(\omega_0 t). \tag{3.10}$$

This leads to the conclusion that the current waveform flowing through the battery in a DC/AC energy conversion process is alternating at twice the frequency of the fundamental grid frequency, and hence

$$i_{DC}(t) = I_{DC}(1 + \cos(2\omega_0 t)) = I_{DC} + \hat{I}_{batt}(t), \tag{3.11}$$

where $\hat{I}_{batt}(t)$ is the AC component of the battery current. Fig. 3.11 depicts the actual measurement of the battery current and voltage during the DC/AC power conversion that demonstrates the quadratic sine wave form of the current and also its influence over the DC voltage, where a ripple oscillation with the same frequency of the current is present. It is clear then that both measurements have a DC component and AC components.

The following equation is employed to represent the transfer function of the AC battery impedance derived from (3.2):

$$Z_{ac}(s) = \frac{s^2 R_a C_{dl} + s(R_o R_a C_{dl}) + R_o + R_a}{s R_a C_{dl} + 1}. \tag{3.12}$$

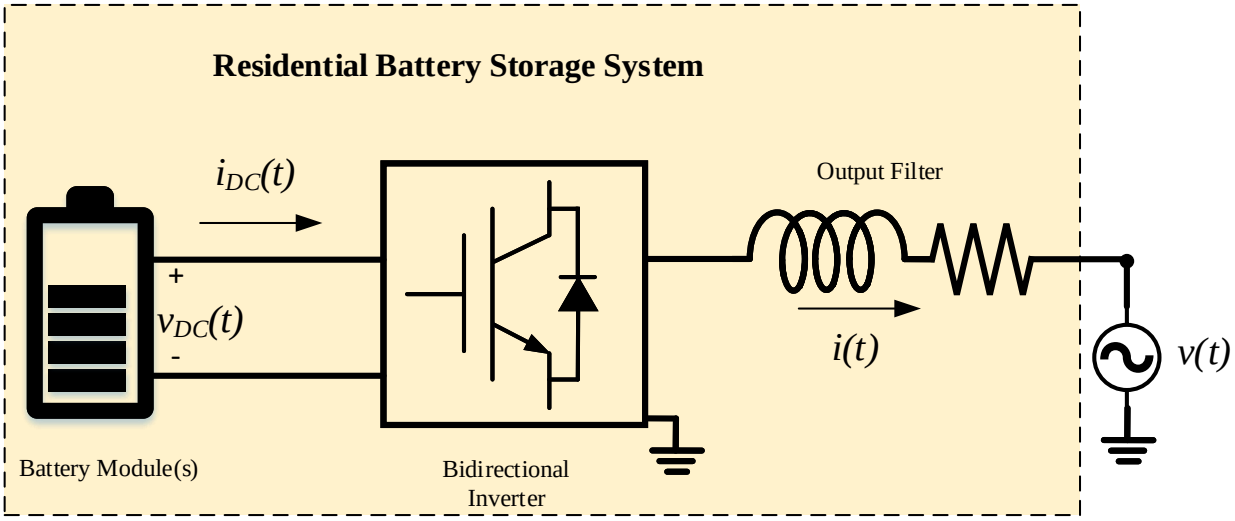

Figure 3.9: Power conversion in a battery energy storage system.

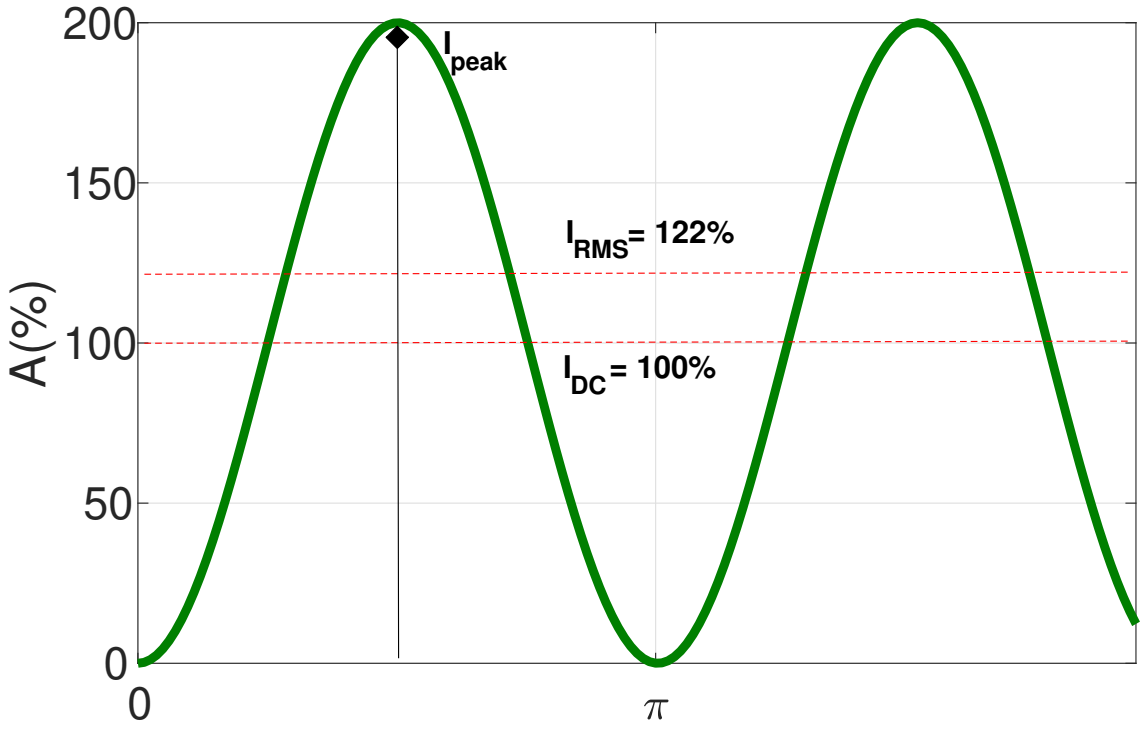

Figure 3.10: Battery current shape during the power conversion process. Reproduced with permission from (Salazar et al., 2018).

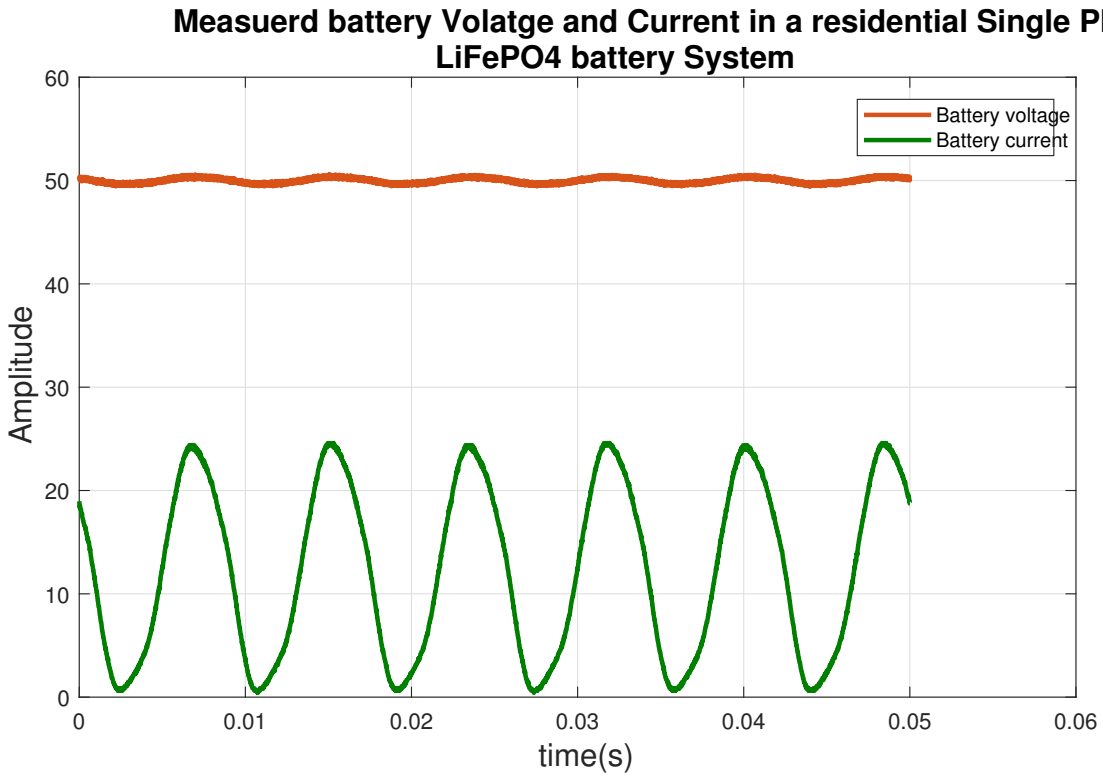

Figure 3.11: Battery current and voltage during the power conversion. Reproduced with permission from (Salazar et al., 2018)

During the DC/AC power conversion process, the battery's over potential voltage (V_{op}) at twice the grid frequency can be obtained by combining (3.12) and (3.11) as

$$V_{op} \equiv |Z_{ac}(2\omega_o)|\, I_{DC} \cos(2\omega_o t + \angle Z_{ac}(2\omega_o)), \tag{3.13}$$

where $\omega_o = 2\pi f_o$ and f_o is the frequency of the power grid.

The AC part of (3.13) represents the voltage ripple caused by the oscillatory behavior of the current at $2f_o$. It is possible to approximate the AC component of the voltage in the battery terminals by V_{op}, i.e., $\hat{V}_{batt} \equiv \hat{V}_{op}$. Then, the AC battery impedance at the frequency $2f_o$ can be expressed as

$$|Z_{ac}(2\omega_o)| = \frac{\mathscr{F}\{\hat{V}_{batt}(t)\}}{\mathscr{F}\{I_{DC} \cos(2\omega_o t + \angle Z(2\omega_o))\}}, \tag{3.14}$$

where $\mathscr{F}$ denotes the Fourier transform. *This shows that by only measuring the current flowing into the battery and the voltage in the battery terminals, an estimation of the internal AC impedance of the cells, for a specific grid frequency, can be achieved.* The proposed online method for battery impedance estimation

consists of sampling the voltage $v_{DC}(t)$ and current $i_{DC}(t)$ at the battery terminals, and then, obtaining the high frequency components by removing the DC components using a moving average filter. The following difference equation shows the recursive representation of this filter:

$$y(k) = ax(k) + y(k-1) + bx(k-N), \tag{3.15}$$

where $a = 1/N$, $b = -1/N$ and N is the number of samples. For the initialization of this filter, i.e., $k = 1$, it is required to store N elements in order to calculate $y(0) = M$, where M is determined by averaging the stored N samples as:

$$M = \frac{1}{N}\sum_{k=1}^{N} x(k).$$

Then, the filtered signal is passed through a second order Goertzel filter, which will allow the extraction of the signal magnitude at the desired frequency (Jaber & Massicotte, 2010). The transfer function of this filter is given by

$$H(z) = \frac{v(z)}{y(z)} = \frac{1 - w_N^{-\frac{2f_0N}{F_s}} z^{-1}}{1 - (2\cos\left(\frac{4\pi f_0}{F_s}\right))z^{-1} + z^{-2}}, \tag{3.16}$$

where F_s is the sampling frequency. With N samples, the filter output will give the signal Fourier transform at the frequency $2f_0$ as

$$\hat{V}(2f_0) = \cos\left(\frac{4\pi f_0}{F_s}\right)v(N-1) - v(N-2) + j\sin\left(\frac{4\pi f_0}{F_s}\right)v(N-1). \tag{3.17}$$

Finally the impedance of the battery at twice the grid frequency is obtained by dividing the real part of the processed battery voltage $\hat{V}_{batt}$ and battery current $\hat{I}_{batt}$ as

$$Z_{ac}(2f_0) = \frac{\mathcal{R}e(\hat{V}_{batt}(2fo))}{\mathcal{R}e(\hat{I}_{batt}(2fo))}. \tag{3.18}$$

3.4 Nonlinear DC/DC Control

The general basic structure of a synchronous buck-boost converter is shown in Figure 3.12. It is composed of two fully controlled switching elements (Q_1 and Q_2), two diodes (D_1 and D_2) and two passive elements (L and C). The voltage of the energy storage source (battery) is indicated by v_{in}. Typically, the converter

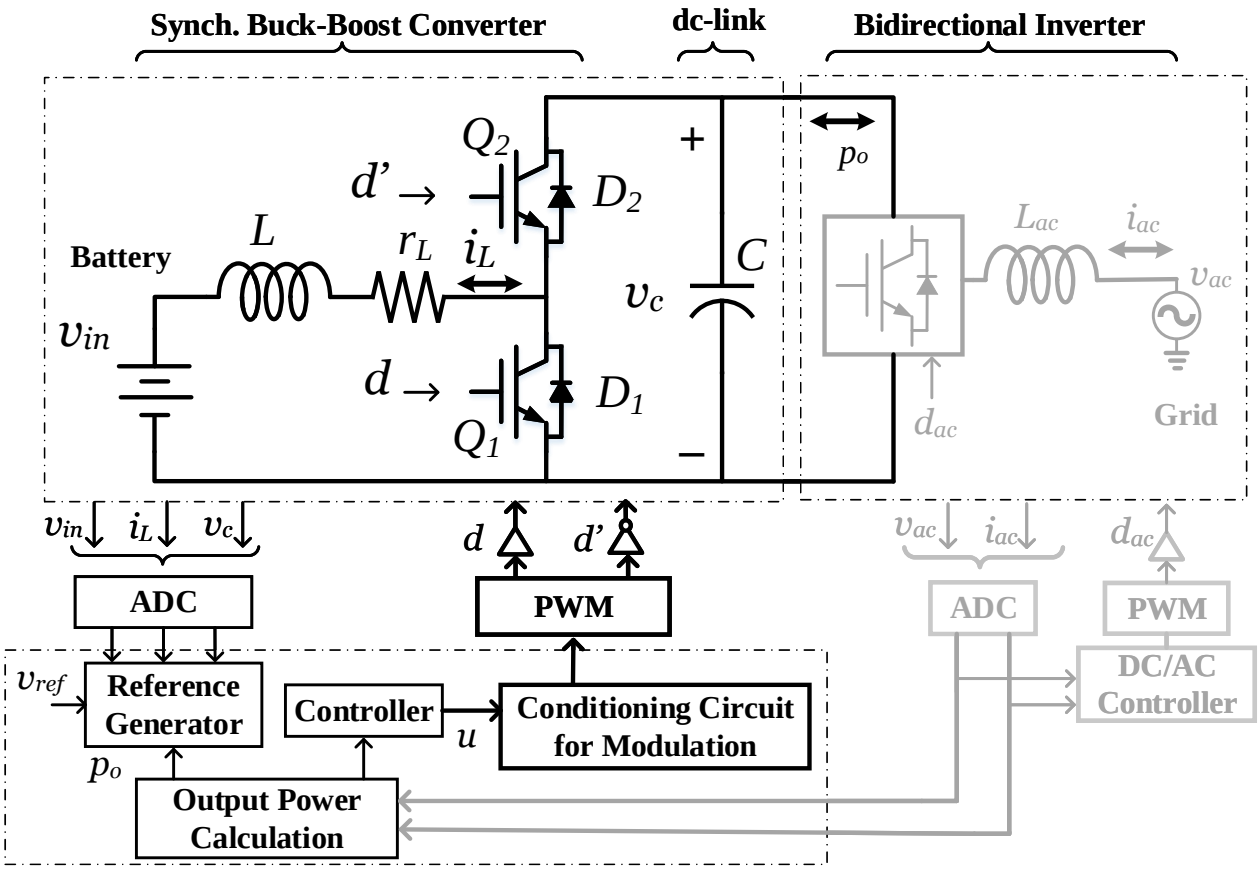

Figure 3.12: System diagram of the synchronous buck-boost converter with a nonlinear load. Copyright ©2019, IEEE

analysis is performed using a linear resistive element as the load; however, in this work, classical linear loads are replaced by a dynamic nonlinear load represented by the dc/ac converter which has bidirectional output power p_o. The winding copper losses in the inductor were also considered in the analysis and illustrated by r_L.

The converter dynamics are controlled by the switching gate signals Q_1 and Q_2. Both switches are synchronized: when Q_1 is turned on/off, then Q_2 is turned off/on. The converter operates as a boost and as a buck converter depending on two variables: the switching sequence and the current on the inductance L or the power flow. When the current i_L is positive (Fig. 3.12), the synchronous buck-boost converter behaves as a boost converter through Q_1 and D_2 and in this scenario, the energy is transferred from the battery to the dc-link and the ac side (load). On the other hand, when $i_L < 0$, the converter behaves as a buck converter through Q_2 and D_1. Under these circumstances, the energy flows from the dc-link to the battery. For this model, the output power flow is controlled by the bidirectional inverter. The following power flow conven-

tion was considered in the dynamic model presented in the following subsection, where if $p_o < 0$ the inverter is discharging to the grid, whereas if $p_o > 0$ the inverter is charging from the grid.

The main goal for the control is to regulate the output voltage or dc-link voltage (v_c) while keeping the energy flow stability between the battery and the dc-link, thus increasing the inverter's degree of freedom by releasing it from the dc-link control and allowing the natural charge/discharge of the battery driven by the power set point on the ac side.

Model Description

The converter dynamics can be modeled during one switching period (T_s) to obtain the converter nonlinear average model. When Q_1 is on (Q_2 is off), the output voltage (dc-link voltage) and inductor's current are given by:

$$\begin{aligned} \frac{\mathrm{d}i_L(t)}{\mathrm{d}t} &= \frac{1}{L}(v_{in}(t) - r_L i_L(t)), \\ \frac{\mathrm{d}v_c(t)}{\mathrm{d}t} &= \frac{p_o(t)}{C v_c(t)}. \end{aligned} \tag{3.19}$$

When Q_2 is on (Q_1 is off), the output voltage and inductor's current are given by:

$$\begin{aligned} \frac{\mathrm{d}i_L(t)}{\mathrm{d}t} &= \frac{1}{L}(v_{in}(t) - r_L i_L(t) - v_c(t)), \\ \frac{\mathrm{d}v_c(t)}{\mathrm{d}t} &= \frac{1}{C}(i_L(t) + \frac{p_o(t)}{v_c(t)}). \end{aligned} \tag{3.20}$$

The average model is then obtained by combining (3.19) and (3.20) Erickson and Maksimovic, 2001, where $d(t)$ represents the input signal (duty cycle) to the system which in the switched model will be the input of the pulse width modulation (PWM). The signal $d'(t)$ is the complement of $d(t)$ defined by $d'(t) = 1 - d(t)$. Then, the average nonlinear state-space representation of the system is given by:

$$\begin{aligned} \frac{\mathrm{d}\langle i_L(t)\rangle}{\mathrm{d}t} &= \frac{1}{L}(\langle v_{in}(t)\rangle - r_L\langle i_L(t)\rangle - (1 - \langle d(t)\rangle)\langle v_c(t)\rangle) \\ \frac{\mathrm{d}\langle v_c(t)\rangle}{\mathrm{d}t} &= \frac{1}{C}(\frac{\langle p_o(t)\rangle}{\langle v_c(t)\rangle} + (1 - \langle d(t)\rangle)\langle i_L(t)\rangle), \end{aligned} \tag{3.21}$$

where $\langle\rangle$ is the average operator.

Dropping the average operator and the time dependency, the model can be rewritten in the form of $\dot{x} = f(x) + g(x)u$, with $x_1 = i_L$, $x_2 = v_c$ and $u = d$, as:

$$\begin{aligned} \dot{x}_1 &= \frac{1}{L}(- r_L x_1 - x_2 + v_{in} + x_2 u), \\ \dot{x}_2 &= \frac{1}{C}(x_1 + \frac{p_o}{x_2} - x_1 u), \end{aligned} \tag{3.22}$$

where

$$f(x) = \begin{bmatrix} \frac{1}{L}(-r_L x_1 - x_2 + v_{in}) \\ \frac{1}{C}(x_1 + \frac{p_o}{x_2}) \end{bmatrix}, \quad g(x) = \begin{bmatrix} \frac{x_2}{L} \\ \frac{-x_1}{C} \end{bmatrix}.$$

3.4.1 Stability Analysis of the Open-loop System

The system equilibrium points are found by solving:

$$\begin{aligned} \dot{x}_1 &= \frac{1}{L}(-r_L \bar{x}_1 - \bar{x}_2 + \bar{v}_{in} + \bar{x}_2 \bar{u}) = 0, \\ \dot{x}_2 &= \frac{1}{C}(\bar{x}_1 + \frac{\bar{p}_o}{\bar{x}_2} - \bar{x}_1 \bar{u}) = 0, \end{aligned} \tag{3.23}$$

where $\bar{x}_1$ and $\bar{x}_2$ are the state variables at the equilibrium. The following relations are obtained:

$$\begin{aligned} \bar{u} &= 1 + \frac{r_L \bar{x}_1 - \bar{v}_{in}}{\bar{x}_2}, \\ \bar{x}_1 &= \frac{-\bar{p}_o}{(1 - \bar{u})\bar{x}_2}. \end{aligned} \tag{3.24}$$

Bifurcation Analysis

By linearizing the nonlinear system equations around the equilibrium points, Jacobian matrix (J) is obtained as

$$J = \begin{bmatrix} \frac{-r_L}{L} & \frac{\bar{u}-1}{L} \\ \frac{1-\bar{u}}{C} & \frac{-\bar{p}_o}{C\bar{x}_2^2} \end{bmatrix}. \tag{3.25}$$

Finding the eigenvalues of this matrix gives the conditions for stability of the open-loop system:

$$\lambda_{1,2} = -\frac{1}{2}(\frac{r_L}{L} + \frac{\bar{p}_o}{C\bar{x}_2^2})\frac{1}{2}\sqrt{(\frac{r_L}{L} + \frac{\bar{p}_o}{C\bar{x}_2^2})^2 - \frac{4}{LC}(\frac{r_L \bar{p}_o}{\bar{x}_2^2} + (1 - \bar{u})^2)}. \tag{3.26}$$

The system around the equilibrium point is a stable focus if $\bar{p}_o > 0$; however, it could become an unstable focus when $\bar{p}_o$ becomes negative, which means that while the system is discharging the batteries, it becomes unstable under open-loop operating conditions. The condition for stability of open-loop system is then given by $\bar{p}_o \leq \frac{Cr_L\bar{x}_2^2}{L}$. This condition becomes a design rule for the minimum dc-link capacitor (C_{min}) required under the absence of any feedback control action:

$$C_{min} \geq \frac{\bar{p}_{o_{max}} L}{r_L \bar{x}_2^2}, \tag{3.27}$$

where $\bar{p}_{omax}$ is the maximum power allowed for discharging in steady state under no feedback control.

Assuming the constant parameters given in Table 3.1 and setting the output power p_o as the changing parameter, a bifurcation diagram is obtained as shown in Figure 3.13. The phase portraits for two different power conditions are also plotted in figures 3.14 and 3.15. It is seen how for $p_o = -4000W$ the flux lines denote the behavior of an unstable focus as they are leaving the trajectory, while for $p_o = -1000W$ the flux lines are entering the trajectory (stable focus). This analysis complements the results obtained in the previous subsection.

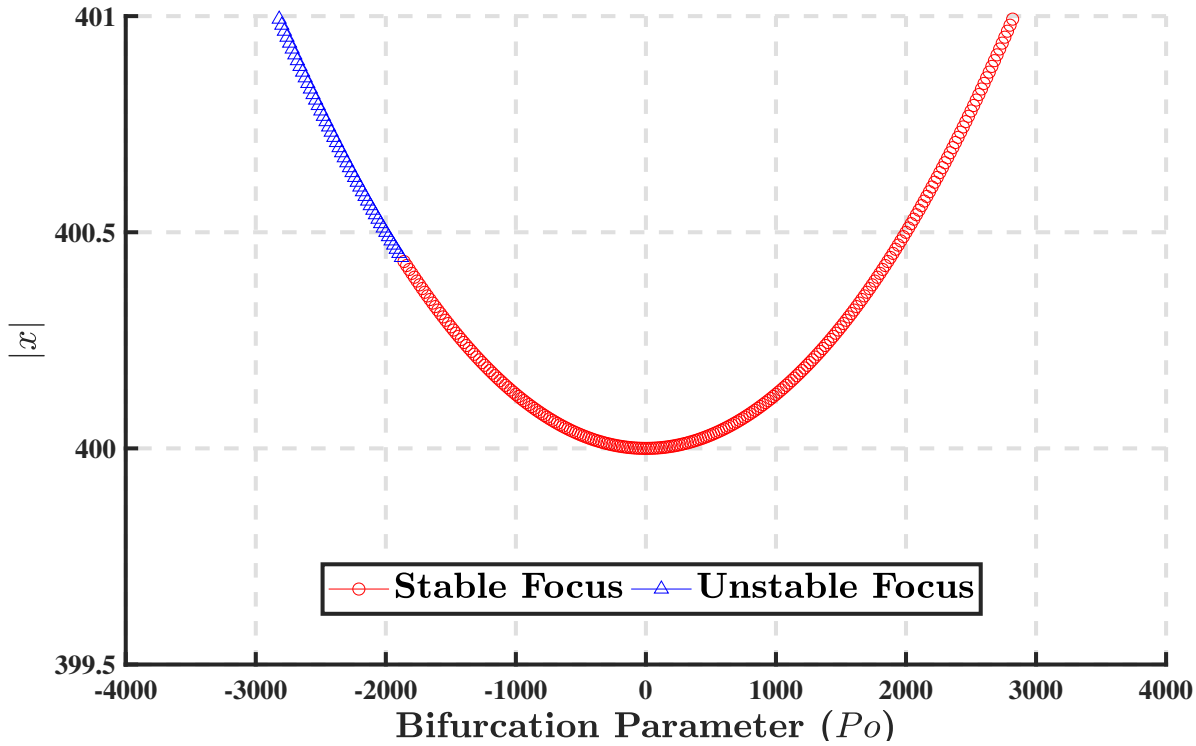

Figure 3.13: Bifurcation analysis. Copyright ©2019, IEEE.

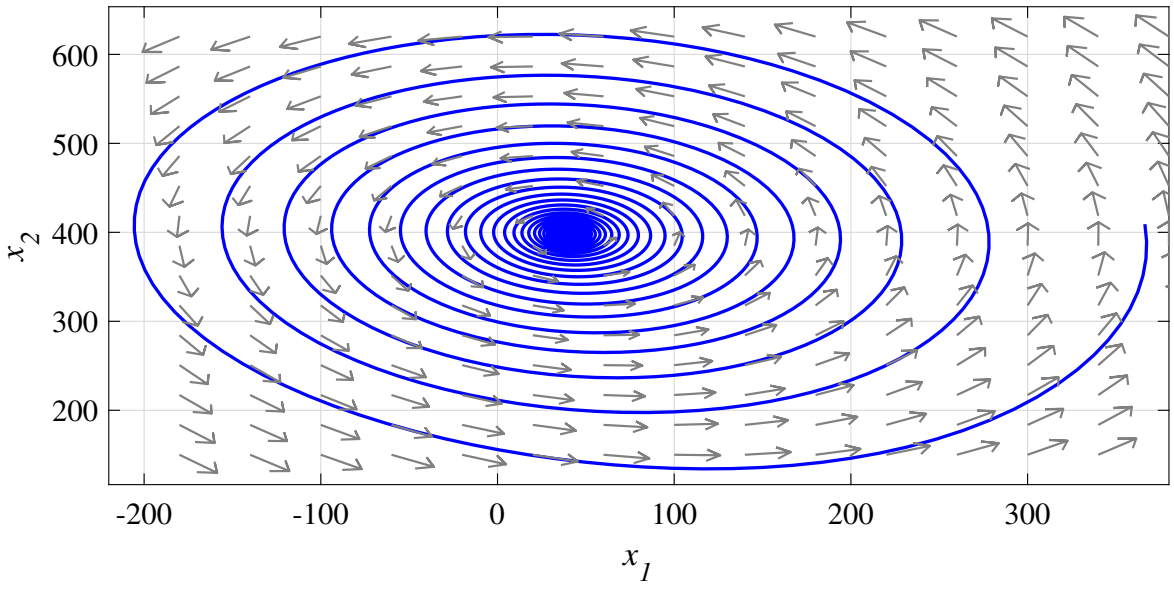

Figure 3.14: Phase portrait unstable focus for $p_o = -4000W$. Copyright ©2019, IEEE.

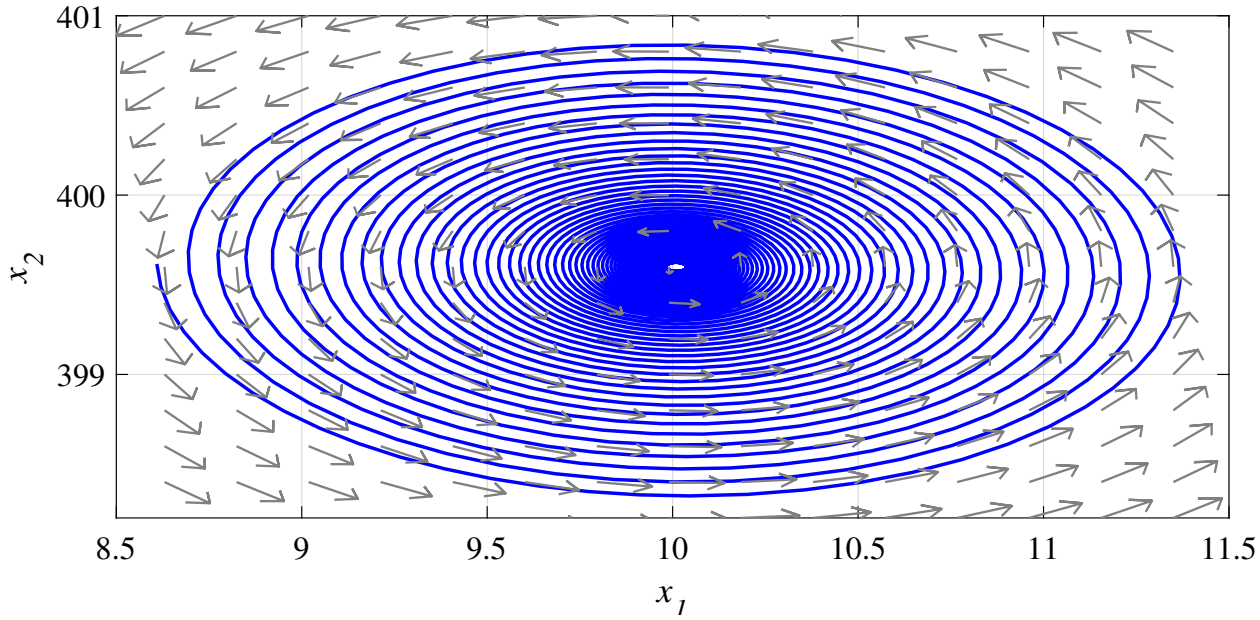

Figure 3.15: Phase portrait stable focus for $p_o = -1000W$. Copyright ©2019, IEEE.

3.4.2 Feedback Linearization Control

In this section, we describe the process of designing the controller based on feedback linearization.

Feedback Linearization

The main goal of the control is to maintain output voltage at a desired (reference) value, $\bar{x}_2 = v_{ref}$, while the inductor's current is stabilized at its equilibrium point ($\bar{x}_1$). Furthermore, the control action must provide a fast transient response considering the switching frequency of the converter. The control law is designed using the transformed system for which the equilibrium point is located at the origin with new state variables defined as $\zeta_1 = x_1 - \bar{x}_1$ and $\zeta_2 = x_2 - \bar{x}_2$.

The transformed state-space model derived from (3.22) is given by

$$\begin{aligned} \dot{\zeta_1} &= \frac{1}{L}(-r_L(\zeta_1 + \bar{x}_1) - (\zeta_2 + \bar{x}_2) + v_{in} + (\zeta_2 + \bar{x}_2)u), \\ \dot{\zeta_2} &= \frac{1}{C}(\zeta_1 + \bar{x}_1 + \frac{p_o}{\zeta_2 + \bar{x}_2} - (\zeta_1 + \bar{x}_1)u), \end{aligned} \tag{3.28}$$

which can further be represented as $\dot{\zeta} = \phi(\zeta) + \gamma(\zeta)u$ with

$$\dot{\zeta} = \begin{bmatrix} \frac{1}{L}(-r_L(\zeta_1 + \bar{x}_1) - (\zeta_2 + \bar{x}_2) + v_{in}) \\ \frac{1}{C}(\zeta_1 + \bar{x}_1 + \frac{p_o}{\zeta_2 + \bar{x}_2}) \end{bmatrix} + \begin{bmatrix} \frac{\zeta_2 + \bar{x}_2}{L} \\ \frac{-(\zeta_1 + \bar{x}_1)}{C} \end{bmatrix} u. \tag{3.29}$$

In order to know if the system (3.29) is feedback linearizable, the following theorem is employed Khalil, 2015.

Theorem 3 *The system $\dot{\zeta} = \phi(\zeta) + \gamma(\zeta)u$ is feedback linearizable if and only if there is a domain $D_0 \subset D$, such that:*

- *The matrix $\Lambda(\zeta) = [\gamma(\zeta), ad_\phi\gamma(\zeta), \cdots, ad_\phi^{n-1}\gamma(\zeta)]$ has rank n for $\forall\ \zeta \in D_0$.*
- *The distribution $D = span\left\{\gamma, ad_\phi\gamma, \cdots, ad_\phi^{n-2}\gamma\right\}$ is involutive in Do.*

In the above theorem, n denotes the system order and $ad_\phi\gamma(\zeta)$ denotes the Lie bracket of ϕ and γ, which is defined as $ad_\phi\gamma(\zeta) = \frac{\partial\gamma}{\partial\zeta}\phi(\zeta) - \frac{\partial\phi}{\partial\zeta}\gamma(\zeta)$.

The following equation shows matrix $\Lambda(\zeta)$ (in Theorem 1), whose rank was determined to be 2, and hence the first condition of Theorem 3 is satisfied:

$$\Lambda(\zeta) = \begin{bmatrix} \frac{\zeta_2 + \bar{x}_2}{L} & \frac{L^2 p_o - LCr_L(\zeta_2 + \bar{x}_2)^2}{L^3 C(\zeta_2 + \bar{x}_2)} \\ \frac{-(\zeta_1 + \bar{x}_1)}{C} & \frac{r_L(\zeta_1 + \bar{x}_1) - v_{in}}{LC} - \frac{p_o(\zeta_1 + \bar{x}_1)}{(C(\zeta_2 + \bar{x}_2))^2} \end{bmatrix}. \tag{3.30}$$

Finally, the second condition of Theorem 1 is satisfied since the *span* for the vector γ belongs to Λ. Therefore, the system described by (3.29) is feedback linearizable. Since the system is feedback linearizable, then there exists a diffeomorphism $T : D \rightarrow R^n$ such that the change of variables $z = T(\zeta)$ transforms the system into the form defined by

$$\dot{z} = Az + B\xi(\zeta)[u - \alpha(\zeta)]. \tag{3.31}$$

The system transformation can take place by using:

$$z = T(\zeta) = \begin{bmatrix} h(\zeta) \\ L_\phi h(\zeta) \end{bmatrix},$$

if and only if there exists a function $h(\zeta)$ that satisfies $L_\gamma h(\zeta) = 0$ subject to the condition $L_\gamma L_\phi h(\zeta) \neq 0$. The Lie derivative of h with respect to ϕ is denoted as $L_\phi h(\zeta)$ and defined as $L_\phi h(\zeta) = \frac{\partial h}{\partial \zeta}\phi(\zeta)$.

A candidate for the function $h(\zeta)$ that satisfies the above condition is:

$$h(\zeta) = L\zeta_1^2 + C\zeta_2^2 + 2L\zeta_1\bar{x}_1 + 2C\zeta_2\bar{x}_2. \tag{3.32}$$

Then,

$$L_\gamma h(\zeta) = \begin{bmatrix} 2L(\zeta_1 + \bar{x}_1) & 2C(\zeta_2 + \bar{x}_2) \end{bmatrix} \begin{bmatrix} \frac{\zeta_2 + \bar{x}_2}{L} \\ \frac{-(\zeta_1 + \bar{x}_1)}{C} \end{bmatrix} = 0.$$

Checking the condition $L_\gamma L_\phi h(\zeta) \neq 0$, it is found that $L_\gamma L_\phi h(\zeta) = \frac{\partial \psi}{\partial \zeta}\gamma(\zeta)$, where $\psi(\zeta) = \frac{\partial h}{\partial \zeta}\phi(\zeta)$. Then, the condition is satisfied:

$$L_\gamma L_\phi h(\zeta) = -((\bar{x}_2 + \zeta_2)(4r_L\zeta_1 - 2v_{in} + 4\bar{x}_1 r_L))/L \neq 0.$$

The diffeormorphism $T(\zeta)$ can then be found from

$$T(\zeta) = \begin{bmatrix} L\zeta_1^2 + C\zeta_2^2 + 2L\zeta_1\bar{x}_1 + 2C\zeta_2\bar{x}_2 \\ -2r_L\bar{x}_1^2 - 4r_L\bar{x}_1\zeta_1 + 2v_{in}\bar{x}_1 - 2r_L\zeta_1^2 + 2v_{in}\zeta_1 + 2p_o \end{bmatrix}. \tag{3.33}$$

The control input u to linearize the system (3.31) is found to be

$$u = \frac{-Kz}{\xi(\zeta)} + \alpha(\zeta), \tag{3.34}$$

where ξ and α are defined as

$$\xi(\zeta) = L_\gamma L_\phi h(\zeta), \qquad \alpha(\zeta) = \frac{L_\phi^2 h(\zeta)}{L_\gamma L_\phi h(\zeta)}, \tag{3.35}$$

which leads to the closed-loop system $\dot{z} = (A - BK)z$, where A and B are the matrices of the state-space model defined in (3.36) in canonical controller form. The closed-loop system is then described by:

$$\begin{bmatrix} \dot{z}_1 \\ \dot{z}_2 \end{bmatrix} = \left(\begin{bmatrix} 0 & 1 \\ 0 & 0 \end{bmatrix} - \begin{bmatrix} 0 \\ 1 \end{bmatrix} [k_1 \;\; k_2] \right) \begin{bmatrix} z_1 \\ z_2 \end{bmatrix}. \tag{3.36}$$

The feedback control gain K is selected using the linear quadratic regulator (LQR) method. The final control law is given by (3.37)

$$u = \frac{Lk_2 \left(r_L(-2\bar{x}_1^2 - 4\bar{x}_1\zeta_1 - 2{\zeta_1}^2) + 2v_{in}(\bar{x}_1 + \zeta_1) + 2p_o \right) + \rho(\zeta_1, \zeta_2)}{(\bar{x}_2 + \zeta_2)\,(4r_L\zeta_1 - 2v_{in} + 4\bar{x}_1 r_L)}, \tag{3.37}$$

where

$$\begin{aligned} \rho(\zeta_1, \zeta_2) = {} & Lk_1 \left(L\zeta_1(\zeta_1 + 2\bar{x}_1) + C\zeta_2(\zeta_2 + 2\bar{x}_2) \right) + \\ & (4r_L(\zeta_1 + 4\bar{x}_1) - 2v_{in})\,(\bar{x}_2 - v_{in} + \zeta_2 + r_L(\zeta_1 + \bar{x}_1))\,. \end{aligned}$$

Power Calculation

According to the signals depicted in Fig. 3.12, the active and reactive power expressions for the single-phase VSI can be written as: $p_o = V_{ac} I_{ac} \cos(\varphi_k)/2$, where φ_k is the displacement power factor angle. It is a common practice to convert the multiphase power system into the two-axis stationary ($\alpha\beta$) or rotary (dq) reference frames. These transformations bring tremendous simplification when determining the active and reactive powers in multi-phase power systems. Hence, the essence of the power computation for the single-phase system is to develop a virtual two-phase system. Then, the instantaneous power theory can be applied.

To generate the secondary orthogonal phase, which is necessary for realizing a virtual two-phase system, various methods have been proposed. In this work, the fictitious phase is obtained using the second order generalized integrator (SOGI) Monfared et al., 2012. Fig. 3.16 illustrates the basic scheme of the SOGI structure, in which $\mathbf{k_s}$ is the damping factor, and ω_k is the fundamental angular frequency. A great feature of SOGI is that depending on the selected damping factor $\mathbf{k_s}$, it provides some kind of filtering and can improve performance under distorted grid voltages. Analogous to

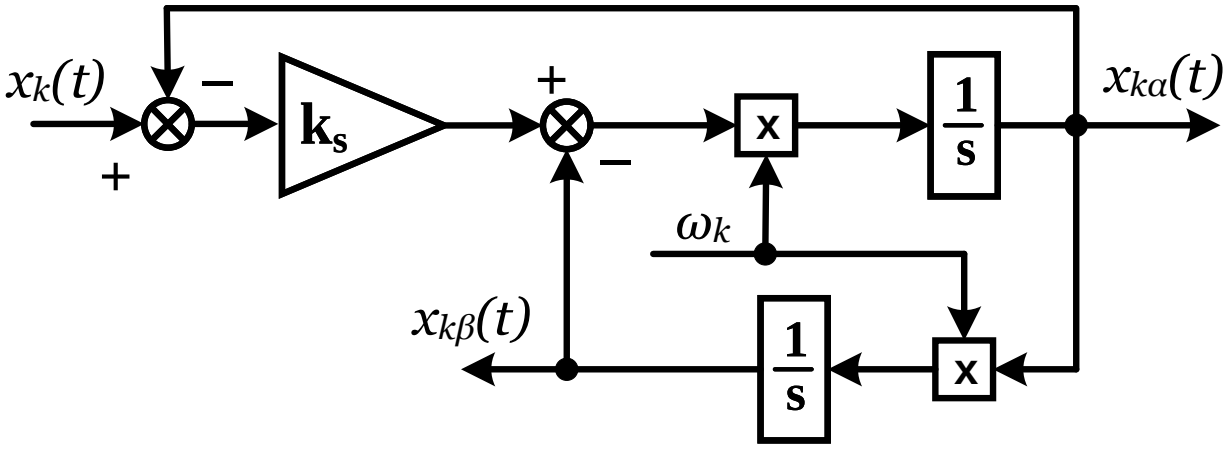

Figure 3.16: Basic configuration of the SOGI structure. Copyright ©2019, IEEE.

a three-phase system, the instantaneous active and reactive powers in the $\alpha\beta$ reference frame are defined as

$$p_o(t) = v_{ac_\alpha}(t)i_{ac_\alpha}(t) + v_{ac_\beta}(t)i_{ac_\beta}(t). \tag{3.38}$$

3.5 Numerical Analysis and Validation

3.5.1 DC Link Control

Feedback Linearization Control

-Simulation Results In order to validate the proposed control scheme, simulations of the synchronous buck-boost depicted in Fig. 3.12, using different levels of output power, were performed. The system parameters used for the simulations are given in Table 3.1.

The voltage reference for the dc-link voltage was kept constant at 400 V. Different output power levels were set after the inverter was connected to the grid. Fig. 3.17 demonstrates the controller ability to keep reference voltage at a constant mean value, while the dc current gets the sinusoidal ripple due to the power conversion process as it was shown in (3.7). Fig. 3.18 shows the output power (inverter's output) and input power (dc-dc converter's input power). Positive values mean that the batteries are being discharged while negative values implies that the batteries are charging. During the battery charging process, the control action tries to keep the input current and consequently input power as closely as possible to the reference output power.

One occasion in which the performance of the non-linear control law surpasses that of the linear control law is when the operating point starts shifting away from the linearization conditions. Following the same simulation setups

Table 3.1: Simulation and HIL Parameters.. Copyright ©2019, IEEE.

Parameter	Value
C	$700\mu F$
L	$600\mu H$
r_L	$10m\Omega$
v_{in}	$100V$
v_{ref}	$400V$

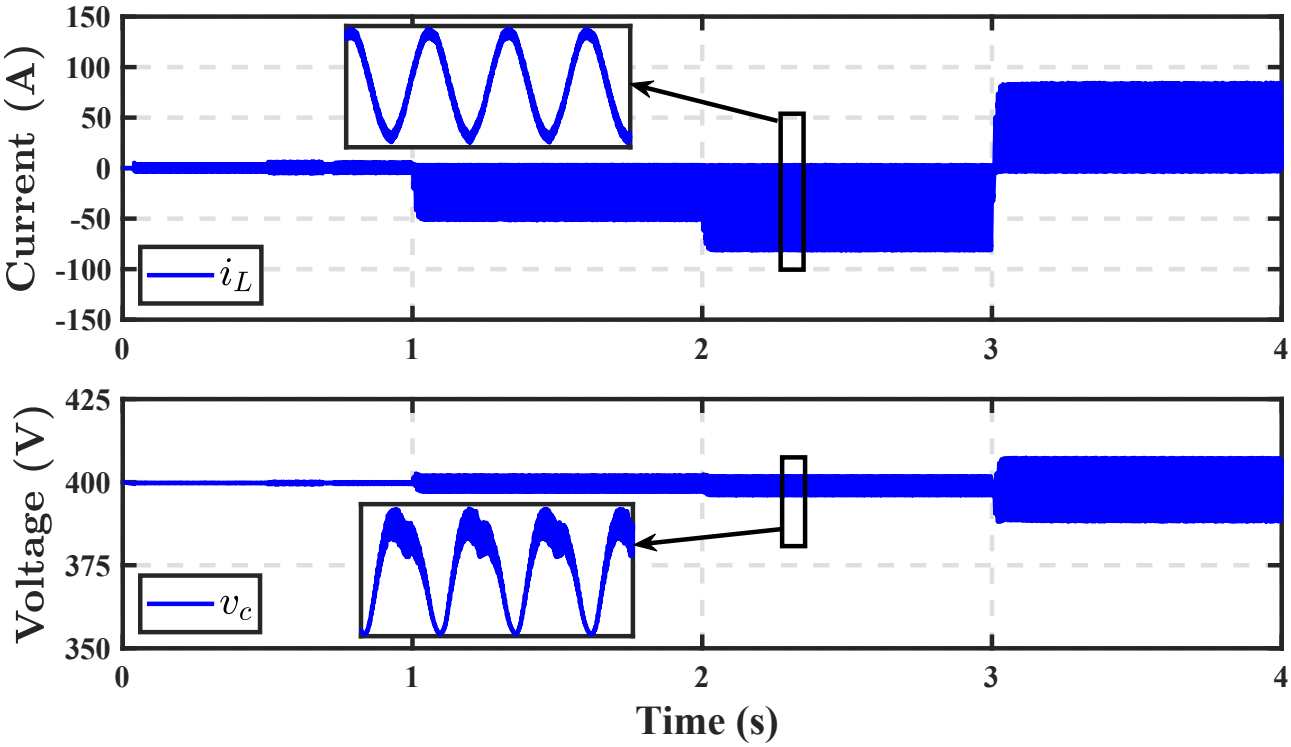

Figure 3.17: Synchronous buck-boost converter with a nonlinear load: (a) input current; (b) output voltage. Copyright ©2019, IEEE.

as before, we now compare two control laws: FBL and linear. The linear control law was found using a linearized model in (3.22) around $v_{in} = 100V$. The test is performed at $v_{in} = 200V$. Under this scenario, the capacitor voltage starts deviating from the stable point, and the ripple starts to increase and show a slower response than the one presented with the non-linear FBL control law (See Fig. 3.19).

-Implementation Results The implementation for the *FBL* controller was done using a digital signal processor (DSP) from Texas Instruments. The intention was to validate the dynamic performance of the controller for changes in the dc-link voltage set point. Initial results were obtained by implementing the power electronics elements in a real-time emulation environment such as a Hardware-in-the-loop (HIL) from OPAL-RT. Fig. 3.20 shows a picture of our experimental setup, and Fig. 3.21 represents the dynamic response of the system when a change in the set point is requested. As observed, the controller is able to track the reference in less than $20ms$.

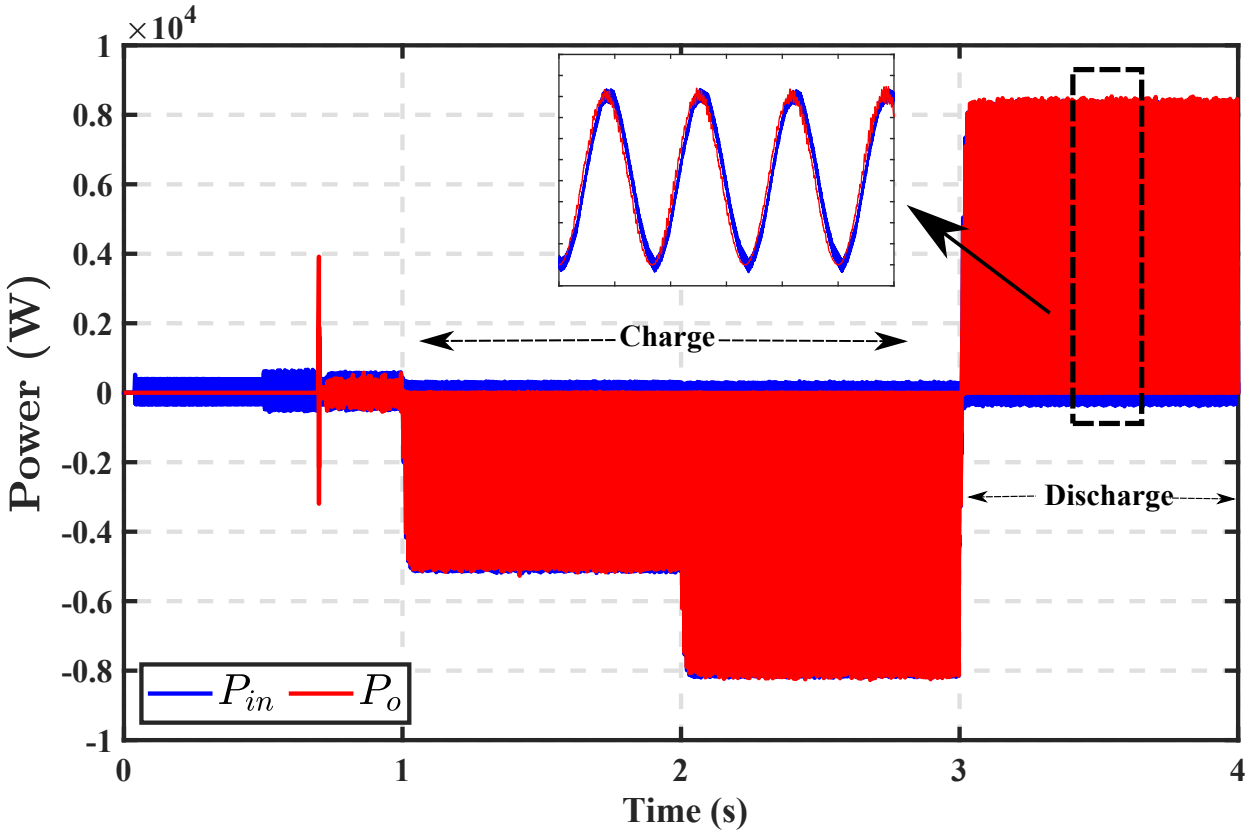

Figure 3.18: Input and output power signals of the synchronous buck-boost converter with a nonlinear load: battery charging and discharging. Copyright ©2019, IEEE.

3.5.2 Online Battery Impedance

The method described in the previous section is implemented in the main microprocessor of the DC/AC power converter as shown in Fig. 3.22. Fig. 3.23 depicts the block diagram for the different modules to be implemented in the firmware application. Different interrupt subroutines (ISR) levels are highlighted in the diagram, where ISR_0 indicates the highest priority ISR.

Generally speaking, the data sampling process occurs asynchronously but is started by the PWM period. ISR_0 starts at the end of the ADC conversion. The data is stored in a temporary RAM memory allocation and then a lower priority Interrupt (ISR_1) can transfer the data to a larger memory allocation in RAM or in Flash. Such larger memory allocation can vary depending on the sampling time (T_s) and the microprocessor data structure. For a floating point 32-bit unit, the allocation of memory can go from 2 KBytes to 5 KBytes for a typical inverter control application, where common sampling frequencies can go from 8kHz to 20kHz. This value can be found from

$$Memory = \frac{F_s N_{cycles} N}{2000 f_o}, \tag{3.39}$$

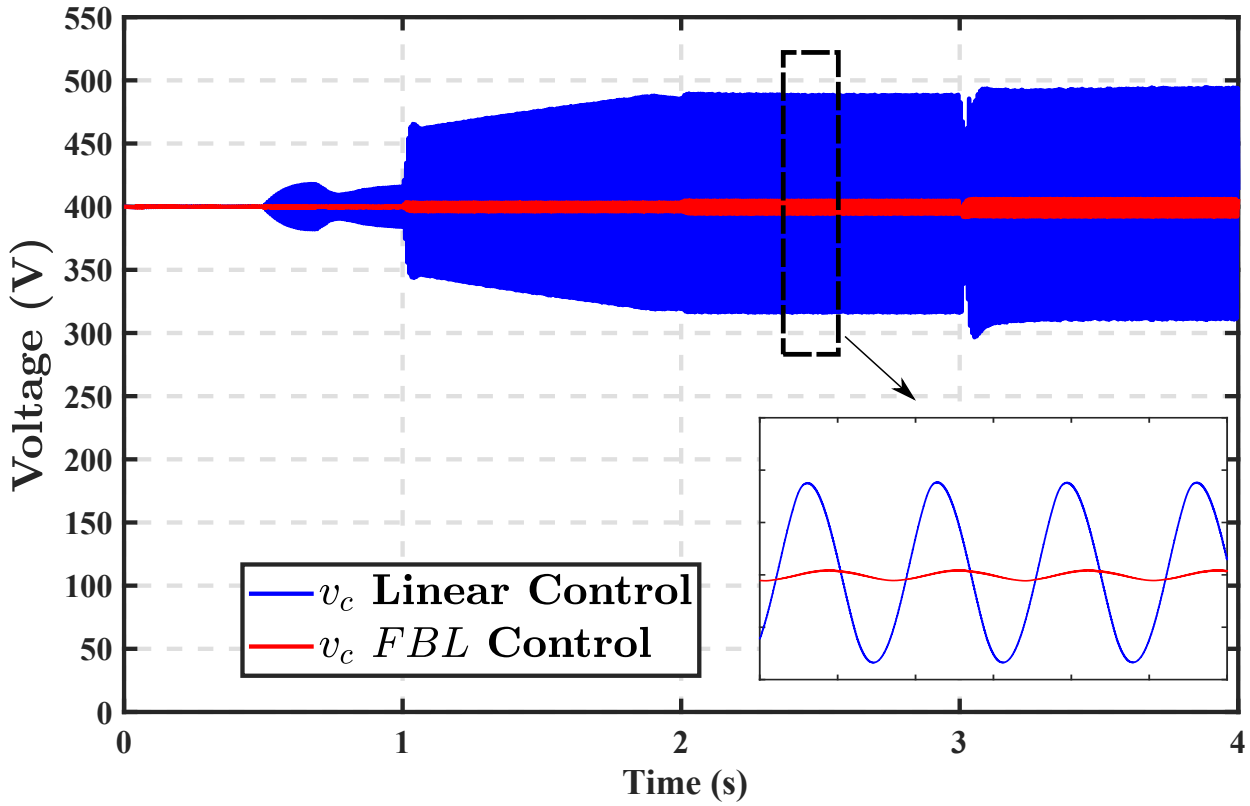

Figure 3.19: DC-link voltage comparison of the synchronous buck-boost converter with a nonlinear load: feedback linearization (FBL) versus linear control law. Copyright ©2019, IEEE.

where F_s is the sampling frequency in KHz, N_{cycles} is the number of cycles to store for the processing, N is the number of bytes in each sample, and f_o is the fundamental grid frequency in Hz. It is noted that in ISR_1, the signal processing modules are implemented as shown in Fig. 3.23. Here, $I_{DC'}(t)$ and $Vbatt'(t)$ represent the AC component of the sampled signals after they are filtered out.

It is noted that the lowest priority interruption subroutine calculates the battery impedance at the aforementioned frequency of $2f_o$. A simple buffer module is created in order to store the previous value of the calculated impedance. This value is then compared against the actual one and according to a decision feature given by k, a diagnostic about the health status of the battery can be made and transmitted to the BMS via serial communication.

The process is implemented in a Texas Instrument $C2000$ core microprocessor, running at a system clock speed of 150MHz. The batteries used for the testing purposes are a commercial type of $LiFePO_4$. They are enclosed in a module under a series and parallel arrangement with a capacity of 2kWh. The AC impedance (per data sheet) is $35m\Omega$ or less. A lab prototype bidirectional inverter of 4kW output is used for obtaining the initial results with main grid frequency of 60Hz, i.e., $f_o = 60Hz$. Estimation of the battery impedance is done at different SOC (State of Charge) levels, going from 7% to 75%. The battery charge and discharge is done continuously at approximately $0.35C$, where

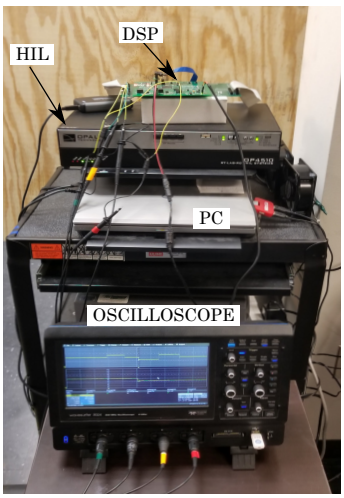

Figure 3.20: HIL experimental setup. Copyright ©2019, IEEE.

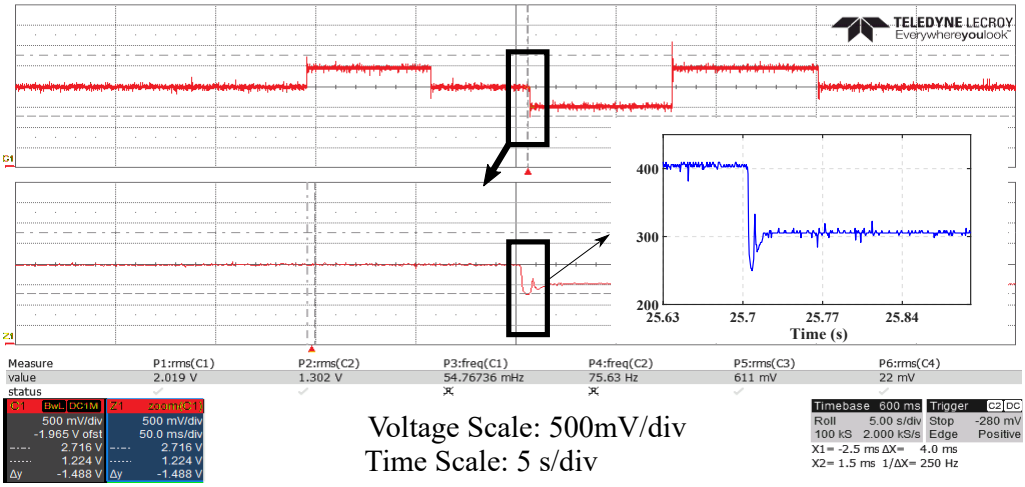

Figure 3.21: Output voltage step response. Copyright ©2019, IEEE.

C is the rate of charge or discharge relative to the capacity of the battery. In this case, $1C$ means that at the rated current, the batteries are discharged or charged in 1 hour. The maximum temperature of the battery module is also monitored with the BMS provided by the manufacturer. Fig. 3.24-b shows the current flowing into the batteries and the battery voltage AC component while the charging process takes place.

The continuous current flowing during the entire testing process increases the internal cell temperature but the external temperature is kept constant at $25°C$. This temperature increase was considered during the experiments and three scenarios were studied. The first is when the internal average temperature of the cells was $30.57°C$, the second is when the temperature was $37.29°C$, and the last one is for an average internal temperature of $39°C$. The same scenarios are run several times and the mean value (μ) of the calculated impedance is summarized in Table 3.2. This table also shows the variance (σ), and the coefficient of variation ($c_v = \sigma/\mu$) for the analyzed data.

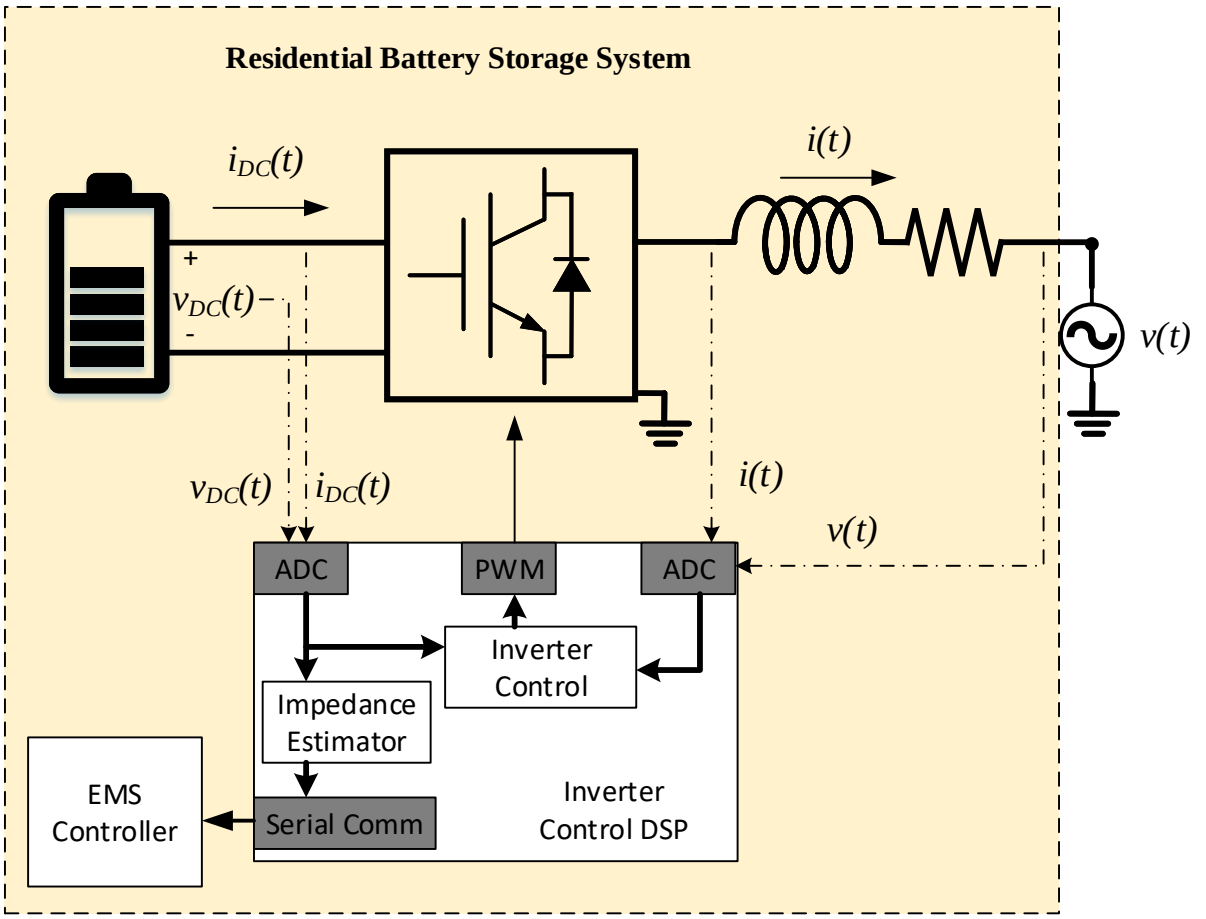

Figure 3.22: Implementation of the proposed method.

Fig. 3.25 illustrates the magnitude of the FFT for one of the mentioned scenarios. A variability in the obtained voltage and current is observed for different SOC levels, which led to variations in the calculated impedance value. However, from the analysis presented in Table 3.2, it can be inferred that the calculated impedance may be considered constant during the entire charge or discharge process and the SOC does not affect the AC impedance calculation at this frequency, which is consistent with the results obtained for a different type of $LiFePO_4$ batteries in (Stroe, Swierczynski, Stan, et al., 2014) and Furthermore, the observed dependency on the internal cell temperature is also consistent with the results presented in (Świerczyński et al., 2014), where spectroscopy analysis results are presented at different temperatures.

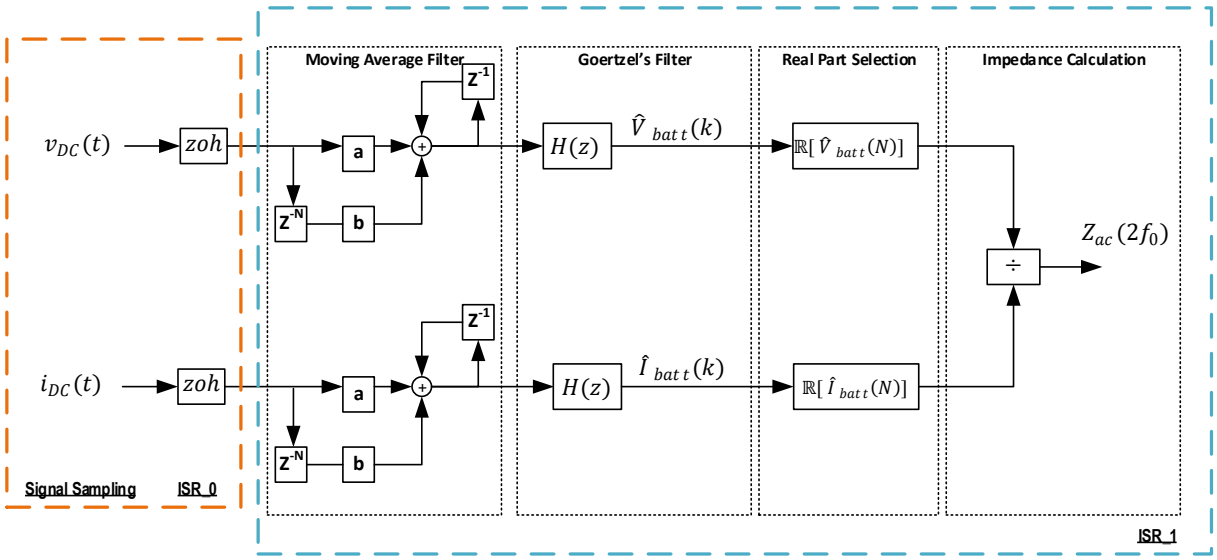

Figure 3.23: Block Diagram representation for implementation of the proposed method. Copyright ©2017, IEEE.

Table 3.2: Calculated impedances for different SOC and different internal battery temperatures. Copyright ©2017, IEEE.

$Z(f_o)$	$T = 30.57°C$	$T = 37.29°C$	$T = 39.02°C$
μ	$28.8m\Omega$	$27.2m\Omega$	$26.8m\Omega$
σ	2.81×10^{-7}	9.45×10^{-8}	3.20×10^{-8}
c_v	9.82×10^{-6}	3.47×10^{-6}	1.18×10^{-6}

Impedance estimation considering DC current ripple reduction

It is possible to reduce the 120Hz ripple magnitude by using a control structure as the one shown in Fig. 3.26. Here an external control loop, generally a PI controller act as a low pass filter for the current reference and an internal current controller loop with a higher bandwidth than the voltage controller is used to track the current reference from the PI output. We took advantage over the scheme already implemented on sonnenCore inverter to study the ability of proposed algorithm to estimate the battery module impedance. The sonnenCore is a 10kwh ESS produced by the company sonnen, Inc in Atlanta GA.

Figure 3.27 shows the input battery current during a full discharge scenario, i.e., 4.8KW. In Fig. 3.27-a the ESS inverter uses a ripple reduction control scheme, whereas in Fig. 3.27-b no ripple reduction control was used. By using the ripple reduction technique, a reduction over 70% was obtained. By observing the internal Battery management system (BMS) information, we determine that the temperature increase was only of 1 degree Celsius, $26°C$ with ripple reduction vs $27°C$ vs no ripple reduction.

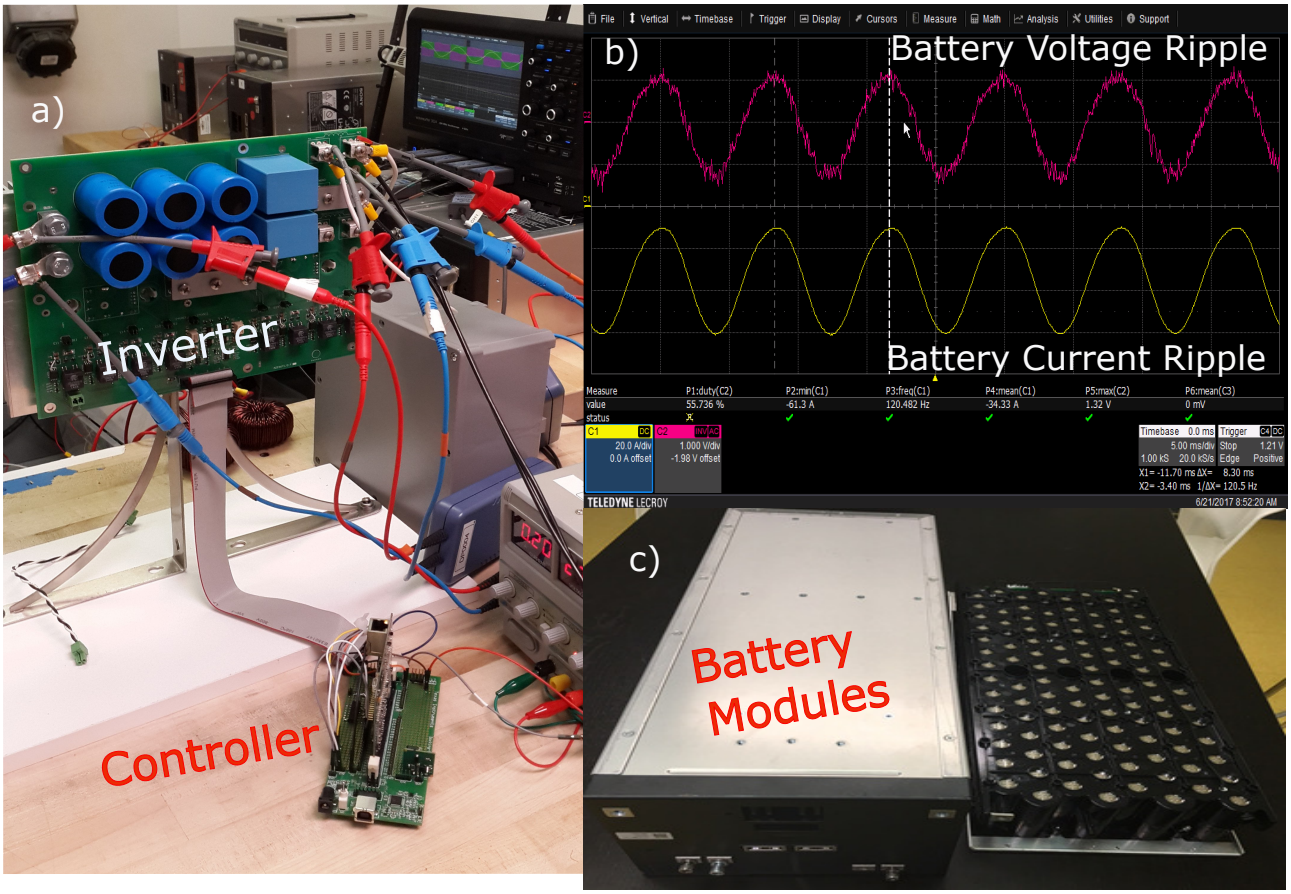

Figure 3.24: Implementation set-up. Reproduced with permission from (Salazar et al., 2018)

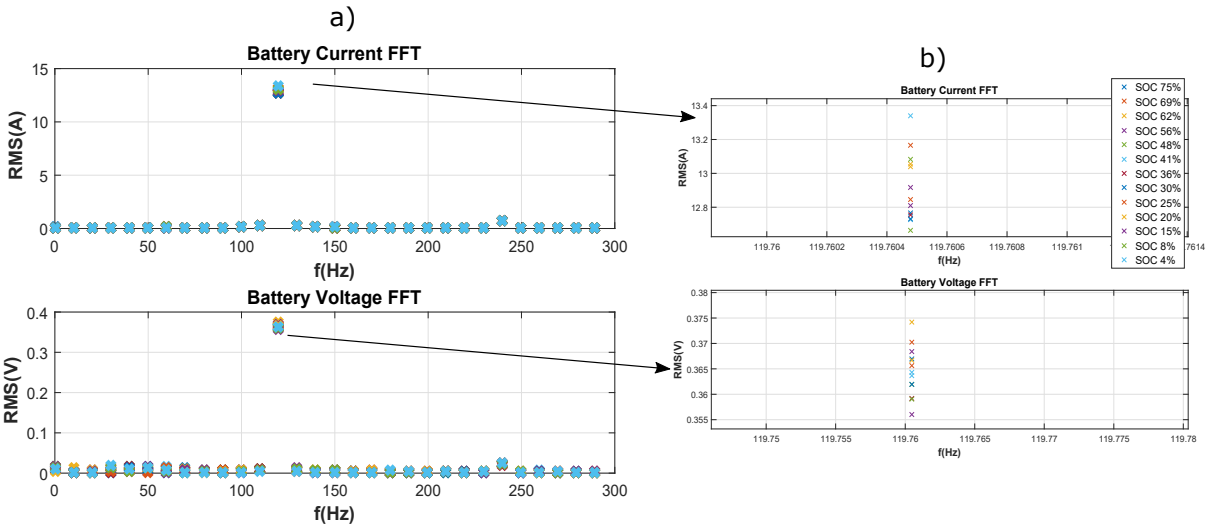

Figure 3.25: FFT of the battery voltage and current at average internal cell temperature of 30°C. a) FFT up to 300 Hz. b) FFT zoom at 120 Hz. Reproduced with permission from (Salazar et al., 2018)

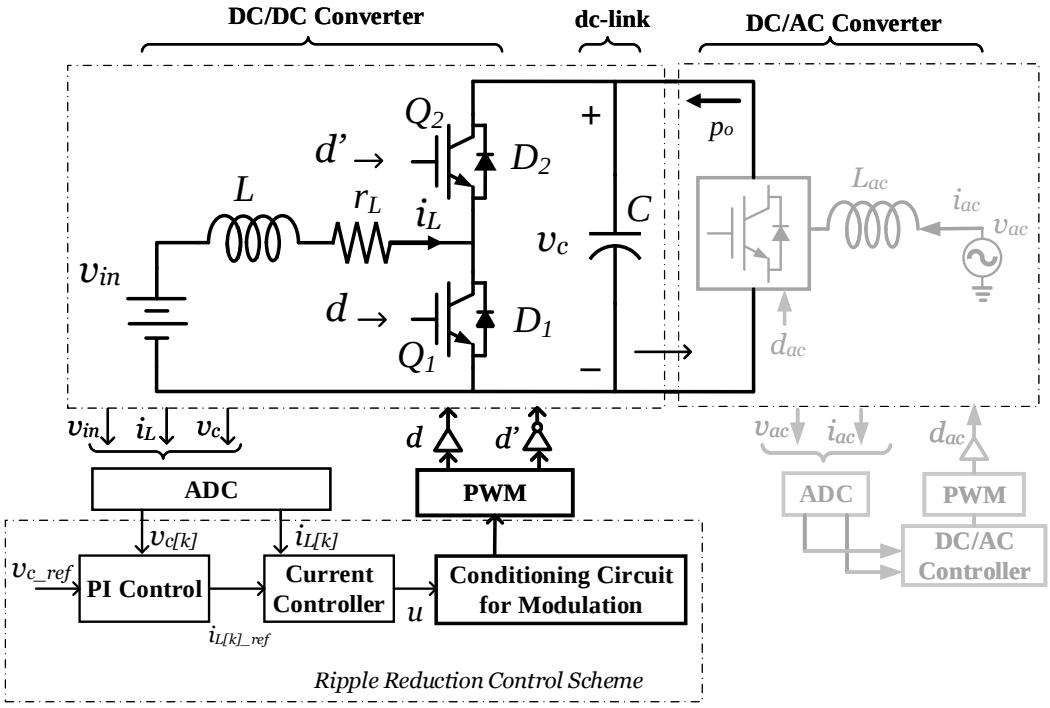

Figure 3.26: Battery current ripple reduction control scheme.

The sonnenCore ESS uses two $LiFePO_4$ battery modules in series of 100V nominal each. The Battery module manufacturer has specified an internal impedance at no charge and at the beginning of life of less than $32m\Omega$, however no measured data was provided or obtained during this experiment. By sampling the battery current and voltage information at the same frequency than the controller does and applying the proposed impedance estimation scheme, we obtained the results presented in Table 3.3. These results are consistent with the battery impedance information provided by the manufacturer considering the effect of aging on the used batteries.

Table 3.3: Estimated battery modules Impedance with Ripple reduction control scheme

SOC	Test Condition	Estimated battery impedance
60 %	Charging - 4.8kW	39.18 $m\Omega$
60 %	Discharging - 4.8kW	39.75 $m\Omega$

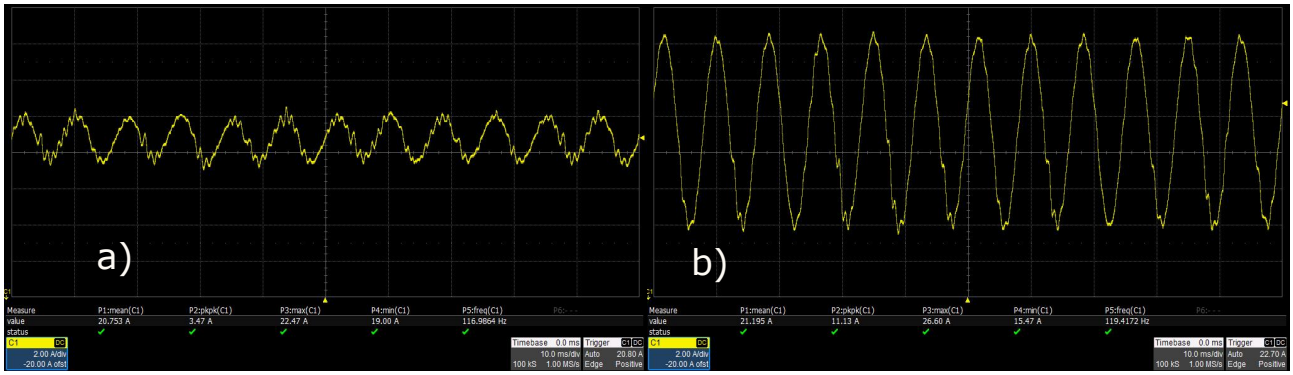

Figure 3.27: Input Battery DC Current at Full discharge scenario of 4.8KW. a) Ripple Reduction used. b) No ripple reduction was used.

Chapter 4

Energy Management of Residential AC Nanogrids

The full content of this chapter has been published in the IEEE Transactions on Industry Applications [1]

4.1 Introduction

In a residential nanogrid, the energy management system (EMS) is responsible for maintaining the balance between the power generated and demands during the islanded periods of operation, avoiding the complete discharge of the ESS by charging them with available RES and/or fuel generator energy (Dawoud et al., 2018; Liu et al., 2018). EMS optimization in NGs and MGs has particularly gained interest due to the stochastic behavior of RES and loads, especially in residential systems.

Dynamic programming (DP)-based methods have been recently employed in (Shuai et al., 2018), in which authors used a Monte Carlo simulation method to cope with uncertainties of the RES generation, electricity pricing and load demand for a grid-tied MG. In (Wei et al., 2017), authors developed an adaptive dynamic programming (ADP) algorithm to solve the optimal battery energy management and control problem in smart residential NGs; however, stochasticity was not considered in the latter work. Comparisons between DP and a rule-based scheduling algorithm for photovoltaic (PV)/generator/batteries nanogrids were presented in (Barnes et al., 2015; Sheng et al., 2015). In (Sheng et al., 2015), a deterministic approach was considered, while in (Barnes et al., 2015) a semi-Markov model was used to forecast the PV generation. References (Barnes et al., 2015; Sheng et al., 2015) both assume a linear process model in the DP problem formulation. A multi-stage stochastic programming structure was proposed in (Bhattacharya et al., 2018),

[1] A. Salazar, A. Berzoy, W. Song and J. M. Velni, "Energy Management of Islanded Nanogrids Through Nonlinear Optimization Using Stochastic Dynamic Programming," in IEEE Transactions on Industry Applications, vol. 56, no. 3, pp. 2129-2137, May-June 2020, doi: 10.1109/TIA.2020.2980731. Copyright ©2020, IEEE.

where uncertainties in supply, demand and pricing were considered for a grid-tied MG. Stochasticity in the DERs has been studied in (Craparo et al., 2017) by employing ensemble weather forecasts and a robust linear program for optimizing a generator's fuel cost; this structure, however, only considered uncertainty in the data obtained by the forecast models. Markov chains for modeling uncertainty in the RES generation have been used in (Belloni et al., 2016), where a Stochastic Dynamic Programming (SDP) algorithm was proposed to optimize the cost of the electric grid energy consumption in wind powered NGs with ESS. In (Belloni et al., 2016), a linear optimization problem was considered and only simulation results were provided.

SDP has also been used for the energy management of residential nanogrids with electric vehicles (EVs), where several authors have focused on proposing solutions to the underlying optimization problem by considering stochasticity in the behavior of the EV, i.e., mobility patterns and home loads. In (Donadee & Ilić, 2014), stochastic models of plug-in and plug-out behavior, energy required for transportation, and electricity pricing were used to minimize electric energy charging costs. A more recent study in (Wu et al., 2018) proposed an SDP-based method for a smart home, where a stochastic model was used for the load demand and for the arrival and departure time of the pluggable electric vehicles (PEVs). A Markov chain was used in (Wu et al., 2018) to model the PEV plug-state. None of the aforementioned references considered the use of renewable sources (and of course stochasticity in the renewable energy generation). Authors in (Wu et al., 2016) use an SDP-based optimization method in a residential photovoltaic application, where the stochasticity is only related to the EV trip time. The authors further proposed the use of Neural Networks (NN) to provide a day-ahead forecast for the PV generation. In our case, a simplified stochastic model based on Markov chains is employed in the proposed SDP-based energy management system.

There exist the opportunity to study the optimal power scheduling of an autonomous NG, considering the stochastic behavior in the renewable energy generation and the non linear behavior of the battery discharging process. In such study, a scheme based on stochastic dynamic programming can be used and its appropriate use could be demonstrated.

This chapter examines the scheduling of an autonomous hybrid (PV and fuel generation) NG. The goal is to supply the demand through optimal scheduling of the NG's available local resources. A stochastic dynamic programming (SDP) optimization problem over a rolling horizon is formulated for real-time control of the battery state of charge (SOC). This paper is based on an early publication in (Salazar, Berzoy, Mohammadpour Velni, et al., 2019). The contributions of this chapter are:

- Developing a simplified time-variant Markov model for the photovoltaic (PV) power generation.
- Proposing a SDP optimization framework for energy management of a hybrid NG in a rolling time horizon, using the Markov model of PV generation.

- Defining a new multi-objective optimization problem to achieve the least cost operation, where the problem is formulated to minimize the generation cost and maximize the availability of energy stored in the battery at the beginning of next operating cycle.
- Formulate a nonlinear optimization problem, where nonlinearities in the discharging process of the batteries are considered.
- Conducting a comparative study between the proposed SDP framework and a rule-based method.

4.2 Optimal Operation of Islanded Residential Nanogrid

4.2.1 System Description

The residential NG used in this work is illustrated in Fig. 4.1. The ESS is an integrated solution of a bidirectional inverter and a set of battery modules. The PV system is composed of an arrangement of PV panels and a solar inverter that always operate at maximum power point tracking (MPPT). The fuel-based generator is a typical gas or liquid propane. The EMS inside of the ESS receives information about the PV production and load demand using external power meters. The goal for the EMS is to minimize the generator's fuel consumption. Red arrows indicate the power flow in the system. Models for each component are described as follows.

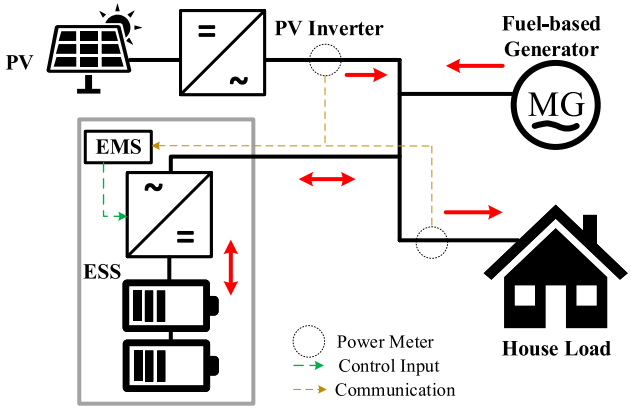

Figure 4.1: Configuration of the nanogrid considered in this work. Copyright ©2020, IEEE.

PV Energy Generation Model

The PV output is connected to a dc/ac converter that only operates when an ac voltage is present at its output. The energy produced by a grid-tied PV system, E_{PV}, can be estimated by

$$E_{PV}[k] = (\eta_{pv}\eta_{inv})(A_{PV}I_0[k]), \tag{4.1}$$

where k is the discrete time index, and the time horizon is divided into N equal intervals. Also, η_{pv} is the PV module efficiency, I_0 is the solar irradiance measured in Watts per square meter (W/m^2), A_{PV} is the effective area, and η_{inv} is the inverter efficiency, which is around 97%.

ESS Model

Energy storage systems in residential ac coupled NGs are usually composed of a set of batteries and a bidirectional converter. The energy capacity and density of the system depend on the cells technology. The efficiency in the energy conversion process is generally between 95% and 97% during charging and discharging, respectively. The equations of battery SOC and the energy stored in the battery E_B can be used interchangeably to describe the charging and discharging behavior and the current and future state of ESS operation by the following nonlinear equation

$$SOC[k] = \frac{1}{C_B} \sum_{k=1}^{N} (I_B[k])\Delta t + SOC_0, \tag{4.2}$$

where I_B is the battery current, which is positive during charging and negative during a discharging period, C_B denotes the battery storage capacity, SOC_0 denotes the initial battery SOC. The energy stored in the battery can be defined by

$$E_B[k+1] = E_B[k] + (P_B[k])\Delta t, \tag{4.3}$$

where $P_B[k]$ is the charge or discharge power assumed to be constant over the time period between $[k\Delta t, (k+1)\Delta t)$, which is positive during charging and negative during a discharging period. We note that (4.3) holds true while the battery is charging. However, during discharging period, the process becomes nonlinear following Peukert's effect. According to Peukert's law, the battery discharge time (L_t) can be approximated by

$$L_t = \frac{C_b}{\hat{I}_B}, \tag{4.4}$$

where

$$\hat{I}_B = (I_{B_{dis}})^{\phi}, \tag{4.5}$$

with $I_{B_{dis}}$ being the battery current during discharge and $\phi \geq 1$ an exponent which describes the exponential nonlinearity of the discharging process in the battery. If we select the parameter as $\phi = 1$, (4.4) turns into a linear model which fails to represent the inherent nonlinearity at high discharge currents. The exponential nonlinear relation reveals that higher discharge currents lead to an exponentially smaller effective capacity (Akyurek & Rosing, 2017). For a real battery, the exponent ϕ is greater than unity. For a lead–acid battery, ϕ is typically between 1.1 and 1.3, whereas for a lithium-ion battery, this constant can vary from 1 to 1.09 (Omar et al., 2012). The effect can be also translated into the

battery power discharge and define a nonlinear term for the energy stored in the battery based on (4.3) as

$$E_B[k+1] = E_B[k] + (\hat{P}_B[k])\Delta t. \tag{4.6}$$

Let us define the battery discharge power as:

$$\hat{P}_B = V_B \hat{I}_B, \tag{4.7}$$

$$\hat{P}_B = V_B (I_{B_{dis}})^{\phi}, \tag{4.8}$$

$$P_{B_{dis}} = V_B I_{B_{dis}}, \tag{4.9}$$

$$\hat{P}_B = V_B (\frac{P_{B_{dis}}}{V_B})^{\phi}. \tag{4.10}$$

For a Lithium-ion battery, it can be assumed that the battery voltage is constant inside the linear operation region. Therefore

$$\hat{P}_B \approx \alpha_v (P_{B_{dis}})^{\phi}, \tag{4.11}$$

where α_v is a constant that could vary from 0.5 to 0.7 for nominal battery voltage between 50V and 400V, which is typically acceptable for commercially available battery storage systems. Then, the nonlinear model for the energy stored in the battery is given by

$$E_B[k+1] = \begin{cases} E_B[k] + \alpha_v (P_B[k])^{\phi} \Delta t, & \forall P_B < 0 \\ E_B[k] + (P_B[k])\Delta t, & \forall P_B \geq 0 \end{cases} \tag{4.12}$$

Constraints imposed on the NG by ESS are given by

$$E_B^{\min} \leq E_B[k] \leq E_B^{\max}, \tag{4.13}$$

$$E_B^{\min} \leq E_B[k+1] \leq E_B^{\max}, \tag{4.14}$$

$$-P_{B-\text{discharge}}^{\max} \leq P_B[k] \leq P_{B-\text{charge}}^{\max}. \tag{4.15}$$

Constraints (4.13) and (4.14) impose allowable SOC limits while (4.15) enforces charging and discharging power limits.

Demand Model

using historic energy consumption data, behavior of the load (E_L) can be forecast. The load in residential applications is seasonal and depends on different factors such as weather, resident standard power usage habit, household size, number of electrical appliances and usage. Generally, auto-regressive moving average (ARMA) models have been used to forecast the load (Pappas et al., 2008). In this work, the load (hourly data) forecast is based on a typical household usage in Atlanta, GA.

Generator Model

A gas generator with the following quadratic cost function is considered

$$C_k(E_G[k]) = \alpha_1 E_G^2[k] + \alpha_2 E_G[k] + \alpha_3, \tag{4.16}$$

where E_G is the energy generated, and α_1, α_2 and α_3 are coefficients obtained from generator's power curve vs. the amount of fuel consumed. The constraint imposed on the NG by generator is defined by the generator maximum and minimum power limits as

$$P_G^{\min} \leq P_G[k] \leq P_G^{\max}. \tag{4.17}$$

Another constraint imposed on the NG comes from the power balance, where the generated energy (sum of PV and gas generator) must be equal to the consumed energy (sum of load and the battery energy discharged). The generator energy required for cost calculations is then

$$E_G[k] = E_L[k] + P_B[k]\Delta t - E_{PV}[k] \geq 0, \tag{4.18}$$

where $P_B[k]$ can be positive or negative, where negative power corresponds to battery discharge.

4.2.2 NG's General EMS Operating Rules

A classical approach to the energy management (EM) on off-grid NGs is based on a rule-based heuristic method, in which the PV generated power is considered to be deterministic and the actual values of PV generation and SOC are utilized to determine the control policy for charging or discharging the batteries. The control policy determines the relation between P_B as the control input and E_B as the system state. A rule-based EM algorithm of the NG under consideration is shown in Algorithm 1. Note that whenever the SOC reaches a predefined minimum level (SOC^{min}), the controller starts charging the battery at a fixed, predetermined power, $P_{B_{\text{fixed}}}$, which is generally set to a low value

to minimize the fuel consumption. This algorithm is executed every time step after the battery charging /discharging process occurs.

Algorithm 1 Rule-based EM algorithm. Copyright ©2020, IEEE.

procedure GENERATOR OFF
  if $SOC[k] > SOC^{\min}$ & $SOC[k] < SOC^{\max}$ **then**
    $P_B[k] = P_{PV}[k] - P_L[k]$
  if $SOC[k] \geq SOC^{\max}$ **then**
    $P_B[k] = -P_L[k]$
  $P_G[k] \leftarrow 0$
  if $SOC[k] = SOC^{\min}$ **then**
    goto **procedure** GENERATOR ON.
procedure GENERATOR ON
  $P_B[k] = P_{B_{\text{fixed}}}$
  $P_G[k] \leftarrow P_L[k] + P_B[k]$
  if $SOC[k] = SOC^{\max}$ **then**
    goto **procedure** GENERATOR OFF.

4.3 Nanogrid Optimal Energy Management

4.3.1 Formulation of Nonlinear Optimization Problem

To achieve an optimal EM, the generation cost (4.16) has to be minimized by finding the battery charging schedule $P_B[k]$ while satisfying power balance equation and all aforementioned operational constraints over the entire operating time horizon T. The EM problem is formulated as a finite horizon constrained quadratic problem. However, the computational complexity increases exponentially with T. Also, in practice, accurate values of inputs (e.g., load profile and PV power) are not available for the whole operating horizon in advance. Therefore, the solution to the original finite time horizon problem can be approximated with that of the corresponding receding time horizon (RTH) optimization problem. To ensure a continuous optimal operation, an additional optimization objective is added to the performance index function J, which is the terminal cost to avoid depleting battery at the end of the optimization

horizon. The battery optimal scheduling for k^{th} time step (for any $k \in \{0, ..., N-1\}$) can be represented by

$$\begin{aligned}
&\min_{P_B[k]} \quad J = \sum_{k=k_0}^{k_f-1} C_k(E_G[k]) + \gamma(E_B^{\max} - E_B[k_f]), \\
&\text{s.t.} \quad E_B[k+1] = \begin{cases} E_B[k] + \alpha_v(P_B[k])^{\phi}\Delta t, & \forall P_B < 0 \\ E_B[k] + (P_B[k])\Delta t, & \forall P_B \geq 0 \end{cases} \\
&E_B^{\min} \leq E_B[k] \leq E_B^{\max}, \\
&E_G^{\min} \leq E_G[k] \leq E_G^{\max}, \\
&P_B^{\min} \leq P_B[k] \leq P_B^{\max}, \\
&E_G[k] \geq 0,
\end{aligned} \tag{4.19}$$

where k_0 is the current time step, $k_f = N + k_0 - 1$ and γ is a weight factor. The above optimization problem is solved at every time step with updated inputs, and the first battery charge/discharge (control action) is implemented as the optimal control policy. More details about the RTH optimization and its applications in EMS can be found in (Bertsekas, 2005) and (Rafiee Sandgani & Sirouspour, 2018). It is noted that the above optimization problem is nonlinear due to the battery dynamics appeared in the constraints.

4.3.2 Stochastic Optimal Energy Management

In practice, power output shows stochasticity due to unpredictable behavior of solar and weather variations. The PV generated power is first modeled as a time-variant Markov process, and then the optimal EM problem is formulated as an RTH quadratic program and solved using SDP.

A.1: PV Power Density Forecast using Markov Models

First-step Discrete-time Markov Model: This is a probabilistic model, in which the transitions from one state to another are directed by discrete probabilities obtained from the statistics of real historical data. The transition matrix (TM) $\boldsymbol{M} = [m_{\epsilon\lambda}] \in \mathbb{R}^{n\times n}$ serves as a probability model that describes the transitions between states on the finite state space $S = \{s_1, ..., s_n\}$, and whose entries are defined as

$$m_{\epsilon\lambda} = \text{Prob}(E_{PV_{k+1}} = s_\lambda | E_{PV_k} = s_\epsilon), \tag{4.20}$$

where s_ϵ is the state of $E_{PV_k} = E_{PV}[k]$ at the time instant k and s_λ is the state of $E_{PV_{k+1}}$ at $(k+1)^{\text{th}}$ time instant. A TM with rows $\boldsymbol{m}_1, .., \boldsymbol{m}_n$ meets the following properties (Puterman, 2014):

$$\begin{cases} \sum_{\lambda=1}^{n} m_{\epsilon\lambda} = 1 \quad \forall \epsilon \in \{1, ..., n\}, \\ m_{\epsilon\lambda} \geq 0, \qquad \forall \epsilon, \lambda \in \{1, ..., n\}. \end{cases} \tag{4.21}$$

The probability that after the k^{th} transition, the state is $x_k = s_\lambda$, given that the initial state is $E_{PV_0} = s_\epsilon$, is defined by

$$\text{Prob}(E_{PV_k} = s_\lambda | E_{PV_0} = s_\epsilon) = m_{\epsilon\lambda}^k, \tag{4.22}$$

where there is a time-variant Markov model with one TM for each time instant.

Let π_k^ϵ be the probability distribution of E_{PV_k} such that

$$\pi_k^\epsilon = \text{Prob}(E_{PV_k} = s_\epsilon). \tag{4.23}$$

In a Markov process, an initial probability distribution can be propagated in time. Then, the propagation of the distribution for future time instants is given by

$$\pi_k = \sum_{\epsilon=1}^{n} (\pi_0^\epsilon \prod_{k=1}^{N} \boldsymbol{M_k}), \tag{4.24}$$

where $\boldsymbol{M_k}$ is the TM of the k^{th} time instant state transition.

Markov Chain for Predicting Hourly Solar Radiation: Markov properties of the solar radiation have been studied in (P. Poggi & Louche, 2000). Here, a discrete time-variant Markov model is used for estimating the hourly clear index and generating the daily shape of solar radiation on a monthly basis. The proposed Markov model is a simplified version of that in (Chamola & Sikdar, 2015). We leverage the nature of solar radiation (i.e., an average rising behavior in the morning, an average falling behavior in the afternoon, and a smooth behavior around noon) to extract a time-variant TM for estimating the radiation in transition between states for a 24-hour time horizon ($N = 24$). The simplified Markov model proposed here obtains the daily probability distribution of the radiation by dividing the day into four different time zones, one for the sun rising (zone T_1), one for the mid day (zone T_2), one for the sun falling (zone T_3), and finally one for the absence of sun (zone T_0). This is depicted in Fig. 4.2. For zone T_0, the TM $\boldsymbol{M}_{T_0} = 0_{n,n}$ is used. Due to a zero or a very low level of solar energy for this zone, a null power generation is assumed. The zones T_1, T_2 and T_3 are respectively denoted by the TMs $\boldsymbol{M}_{T_1}$, $\boldsymbol{M}_{T_2}$ and $\boldsymbol{M}_{T_3}$. The TM of each zone is determined separately using

the historical data related to that part of the day assumed to be independent of the TMs of other zones. This results in radiation transitions that may not infringe the statistics of other transition frequencies.

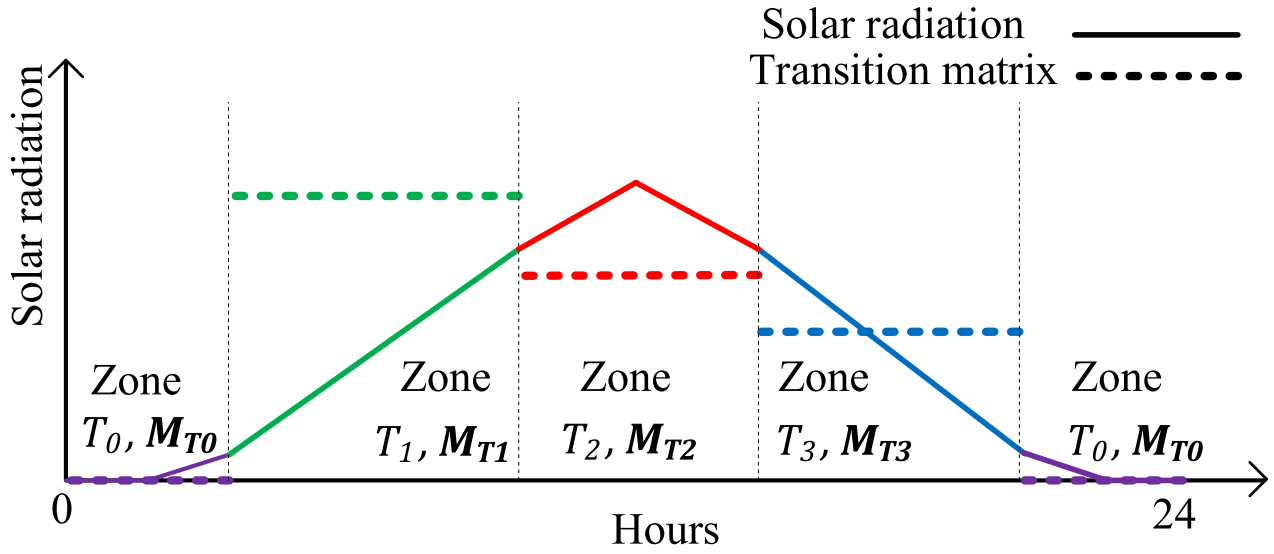

Figure 4.2: Four zones of operation considered in obtaining the probability distribution of daily solar radiation. Copyright ©2020, IEEE.

In order to obtain the TM for the solar energy generation, the generated energy ($\mathrm{Wh/m^2}$) is discretized in n states each representing a region of occurrence, i.e.,

$$\begin{aligned} s_1: \quad & 0 \leq E_{PV}[k] \leq \frac{E_{PV}^{\max}}{n}, \\ & \vdots \\ s_n: \quad & \frac{(n-1)\times E_{PV}^{\max}}{n} < E_{PV}[k] \leq E_{PV}^{\max}, \end{aligned} \tag{4.25}$$

where $E_{PV}^{\max}$ is the maximum hourly radiation level, and the number of states, n, is determined based on $E_{PV}^{\max}$.

From a set of historical hourly solar radiation data in one month, the frequency of transitions from state ϵ to λ, $f_{\epsilon,\lambda}$, is found. Subsequently, the frequencies are converted into probabilities

$$m_{\epsilon\lambda} = \frac{f_{\epsilon,\lambda}}{N_{f_{\epsilon,\lambda}}}, \tag{4.26}$$

where $N_{f_{\epsilon,\lambda}}$ is the total transitions. At each time zone T_l, where $l \in \{0, 1, 2, 3\}$, the same procedure is employed to determine TM.

A.2: Optimal Energy Management using SDP

In this section, the proposed time-variant Markov model for PV prediction is employed in NG's EM problem formulated as a stochastic time-varying optimal control problem. using the proposed stochastic EM approach, expected cost of NG operation is minimized over the operating horizon. The stationary TMs are described as before.

Using the Markov model of the PV generation, considering the battery energy and PV generation as the system states, i.e., $\mathbf{x_k} = [x_1, x_2]^T = [E_B, E_{PV}]^T$, and by assuming $\mathbf{u_k} = [u_1] = [P_B]$ as the input vector and $\mathbf{d_k} = [d_1] = [E_L]$ as the load vector, the NG state-space model becomes:

$$\mathbf{x_{k+1}} = \begin{cases} \begin{bmatrix} x_1[k+1] \\ x_2[k+1] \end{bmatrix} = \begin{bmatrix} x_1[k] + (u_1[k])^{\phi}\Delta t \\ h_k(x_2[k], w_k) \end{bmatrix}, & \forall u_1[k] < 0 \\ \\ \begin{bmatrix} x_1[k+1] \\ x_2[k+1] \end{bmatrix} = \begin{bmatrix} x_1[k] + (u_1[k])\Delta t \\ h_k(x_2[k], w_k) \end{bmatrix}, & \forall u_1[k] \geq 0 \end{cases} \tag{4.27}$$

where w_k is a random variable with independent samples and h_k is the probability density that satisfies

$$\text{Prob}\{h_k(s_i, w_k = s_j)\} = m_{ij}^k. \tag{4.28}$$

To minimize the NG operational cost, sum of the gas generator cost over the optimization horizon should be minimized; therefore, we consider the generation cost at time step k as the stage cost g_k defined by

$$g_k = C_k(-x_2[k] + d_1[k] + u_1[k]\Delta t). \tag{4.29}$$

Furthermore, the terminal cost g_N is considered as

$$g_N = \omega_1(E_B^{\max} - x_1[N]), \tag{4.30}$$

where ω_1 is a weight on terminal cost. The terminal cost enforces battery to stay sufficiently charged. With the stage cost g_k as the fuel generator cost, the expected performance index function J_s becomes $J_s = \mathbf{E}(\sum_{k=0}^{N-1} g_k + g_N)$, in which $\mathbf{E}(\cdot)$ denotes the expected value of the associated random process. To minimize the NG operational cost, the expected performance index function has to be minimized over the control input u_2 subject to state-space equations (4.27) and physical constraints represented by (4.19). By applying Bellman operator, the stochastic optimization problem is divided into a recursive single step optimization

$$\mu_k^*(\mathbf{x_k}) = \arg\min_{u_{1_k}}(\mathbf{E_{gf}})$$
$$\mathbf{E_{gf}} = \mathbf{E}(g_k) + \mathbf{E}(V_{k+1}^*(\mathbf{x_{k+1}})) \tag{4.31a}$$

$$V_k^*(\mathbf{x_k}) = \mathbf{E}(g_k) + \mathbf{E}(V_{k+1}^*(\mathbf{x_{k+1}})). \tag{4.31b}$$

The above problems need be solved backward in time. By solving the above time-varying SDP, the battery charge/discharge policy is calculated and the first step control input is implemented. Summary of the SDP algorithm is shown in Algorithm 2.

Algorithm 2 Stochastic DP algorithm. Copyright ©2020, IEEE.

procedure FUNCTION ASSIGNMENT
  $g_k \leftarrow C_k(E_G[k])$
  $g_N \leftarrow \omega_1(E_B^{\max} - E_{B_N})$
  $V_N^* := g_N$
  $\mathbf{u_k} = [P_B]$
  $\mathbf{x_k} = [x_1, x_2]^T = [E_B, E_{PV}]^T$
procedure MINIMIZATION
  for $k = N - 1 : 0$ **do**
    Solve (4.31a) for $\mu_k^*(\mathbf{x_k})$
    Update $V_k^*(\mathbf{x_k})$ using (4.31b)
  $u_{2_0} \leftarrow \mu_0^*$

A.3: Real-Time SDP Implementation

The practical implementation and programming of the optimization algorithm based on SDP is presented in the flowchart diagram depicted in Fig. 4.4. Before proceeding with the description of the flowchart, it is worth mentioning that the SDP algorithm needs to have information about the discrete state values and the control input as defined in Algorithm 2. The following definitions are made and corresponding information is fed into the algorithm initially:

$$x_1(\cdot) \in \mathbb{R}^{n_1}, x_2(\cdot) \in \mathbb{R}^n, d_1(\cdot) \in \mathbb{R}^N, u_1(\cdot) \in \mathbb{R}^{n_2}.$$

$$\mathbf{g_N}(\cdot) : dim[\mathbf{g_N}(\cdot)] = n_1 \times n$$

$$\mathbf{M_{k_t}}(\cdot) : dim[\mathbf{M_{k_t}}(\cdot)] = n \times n$$

The algorithm is initialized at every control decision step (k). The time horizon (N) is assigned to a variable k which is going to keep track of the rolling horizon iteration. For the first iteration, a matrix $\mathbf{J_{togo}}$ is filled with the coefficients corresponding to the final cost that is desired to be achieved from each one of the initial states. Depending on the current time step in the optimization rolling horizon (k), the transition matrix is copied into a variable $\mathbf{P}$, following the procedure described in section A.1. Three nested loops are used to calculate the cost to go matrix for the current time horizon step (k). A temporary cost vector $J_o \in \mathbb{R}^{n_2}$ is calculated using (4.31b). Here the value of the next state for $x_1(k+1)$ is calculated according to (4.3). This value is then used to obtain the index (idx), which is the argument of the vector x_1 for the calculated value. f is a temporary variable used in the expected value calculation. After all of the discrete values for the input are considered, the minimum cost is stored in the corresponding coefficient for the cost to go matrix and an additional matrix $\mathbf{U}^*$ is used to store the argument or index for which this minimum is achieved. The iterations are completed for all the possible states, and the cost to go matrix is used for the following k_{th} iteration. The beginning of the time horizon is reached, and the current states are checked by assigning their arguments to the variables $idx1$ and $idx2$, which are the indexes to determine optimum value for the input from matrix $\mathbf{U}^*$.

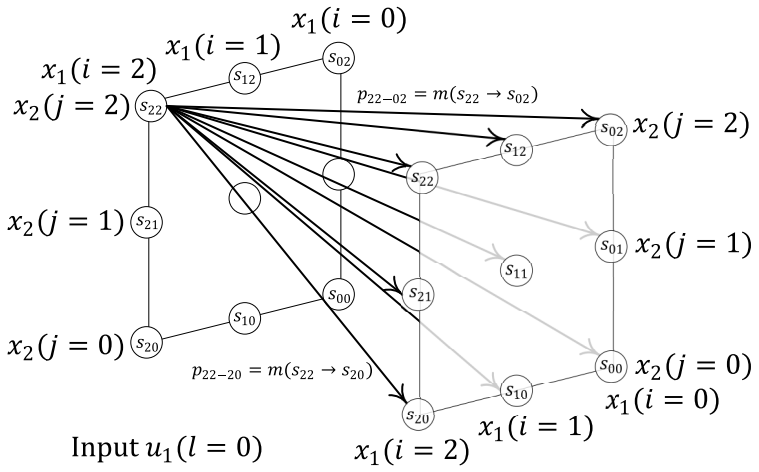

Figure 4.3: An illustrative example for $n_1 = 3$ and $n = 3$ at $l = 0$. Transition probability diagram for different values of the PV is shown here. Copyright ©2020, IEEE.

As an illustrative example, consider the diagram with only few states shown in Fig. 4.3. An example of the transition probability for the dynamic programming algorithm when $n_1 = 3$ and $n = 3$ is shown. Notice that the two states x_1 and x_2 form a 3×3 matrix with all the states options on the time step k. The transition between states would have as many options as admissible inputs are allowed by the transition probability matrix; however, the total case of transitions could vary depending on the system behavior. For this example, all the transitions are possible which give 9 per state, in total would be as many as 81 possible transitions (not

drawn in Fig. 4.3). In the figure, the 9 cases of transitions for the state $[x_1(i = 2), x_2(j = 2)]$ are defined by the arrows, and two of them are specified. If the system is in the state $[x_1(i = 2), x_2(j = 2)]$, then PV probability distribution is defined as $\text{Prob}(s_{22} \rightarrow s_{02}) = m_{22\rightarrow 02}$ which indicates the probability that the system will be in the state $[x_1(i = 2), x_2(j = 0)]$ at the next discrete time $k + 1$ moment.

4.4 Simulation and HIL Test Results

For the purpose of verification and comparison of the proposed optimal EM algorithm, simulation and real-time hardware-in-the-loop (HIL) tests are performed in MATLAB/Simulink environment and OPAL RT, respectively. The main parameters of the NG (as shown in Fig. 4.1) are given in Table 4.1. The parameters are chosen based on an available commercial prototype for residential applications. Simulations of the NG

Table 4.1: Nanogrid parameters. Copyright ©2020, IEEE.

Parameter	Value	Parameter	Value
E_B^{max}	$6k$Wh	ω_1	7×10^8
E_B^{min}	300Wh	I_0^{max}	$1.018 \frac{k\text{Wh}}{\text{m}^2}$
$P_{B-charge}^{max}$	$4k$W	η_{pv}	0.19
$P_{B-discharge}^{max}$	$3.5k$W	η_{inv}	0.98
P_G^{max}	$8k$W	A_{PV}	18m^2
P_G^{min}	$0k$W	T	24 hours
P_{PV}^{max}	$5k$W	Δt	1 hour
α_1	1.2898×10^{-9}	N	24
α_2	1.3609×10^{-4}	n	22
α_3	0.9117×10^{-16}	ϕ	1.09
n_1	120	n_2	115
α_v	0.6	G_{price}	$0.5 \frac{USD}{thm}$

energy management start from the same initial condition, i.e., $E_B(0) = E_B^{\max}$. In addition, the daily PV generation profile is taken from the solar radiation data from *NREL* database ((NREL)., n.d.).

4.4.1 Results for the Simulated NG System

Evaluation of the Markov Model

In order to validate the proposed model, 15-year solar radiation data of the month of July of a site located in Elizabeth City, North Carolina, extracted from the *NREL* database is used. The model is learned using 13 years of data and validated on the other two years data. The maximum hourly radiation of the site is

$I_0^{max} = 1.018\ k\text{Wh/m}^2$, and the number of Markov model states is considered to be $n = 22$ with the states taking values as $s_i \in \{0, 1, ..., 21\}$ for $\forall i \in \{1, ..., 22\}$.

In order to evaluate the performance of the proposed time-variant Markov model, data from the average day of the two years is selected. The results of the Markov model for each hour have a probability distribution; the expected value of each probability distribution is used for the evaluation of the results. The PV output predicted by the proposed model for the subsequent 24 hours is compared with the time-invariant Markov model and the real data in Fig. 4.5. As observed, the model is able to follow the real mean profile, while closely approximating the standard deviation for the obtained data. In order to show the improvements achieved by the proposed model compared to the time-invariant model, the relative root mean square error ($RRMSE$) is used to quantify the total estimation error.

$RRMSE$ value achieved by the proposed model is 9.14%, whereas the error with the stationary (time-invariant) model is 31.3%. using the proposed model, *the error considerably decreases while the computational complexity nearly remains the same*. Next, simulation results using SDP are compared against those obtained from the rule-based algorithm.

Comparative Assessment of Rule-based EM and SDP-based Approach

Two cases are simulated considering different solar irradiance levels over a period of 72 hours. The first one is shown in Fig. 4.6, where three consecutive days with good irradiance are presented. The comparison between battery SOC for rule-based ($SOC_{B_{rule}}$) and SDP-based ($SOC_{B_{sdp}}$) methods is shown in the third subplot. Generation power for both algorithms is also shown in this figure. With the SDP approach, the EMS is able to consume less generator power over the three days and finish each day with a higher battery SOC index. The rule-based algorithm charges the battery whenever the energy stored in the battery is below 2 kWh. On the other hand, the underlying optimization problem for the SDP method is solved on a rolling horizon basis. The prediction horizon is assumed to be 24 hours, and at each hour, it determines the optimal policy for the next 24 hours. The control policy for this case is the battery charge/discharge power (control input) as a function of battery stored energy and PV generated energy (which are the system states). Table 4.2 shows the cost of operating the generator each day and the availability index in Wh, which is the battery SOC at the end of each day. Results showed that after the third day of operation, the user could save up to 20% of the generator's cost if the SDP method is employed. Fig. 4.7 shows the system behavior assuming that the second day irradiance is proportionally lower than the other two days. In this case, the total saving for operating the NG could be up to 7% if the SDP algorithm is used.

Table 4.2: Three days performance comparison using rule-based and stochastic DP methods. Copyright ©2020, IEEE.

Generator fuel cost ($/*day*)			Battery availability index (Wh)	
Day	Rule-based	SDP	Rule-based	SDP
1	0.9291	0.8705	1,944	3,350
2	1.3936	0.9713	4,650	4,650
3	0.9291	0.7638	1,872	3,950

4.4.2 Real-time HIL Simulation Results

Performance of the two proposed methods (rule-based and SDP) is evaluated using OPAL-RT Model-In-the-Loop real-time experiments. The NG is implemented in the OPAL-RT unit using dynamic models for the inverters, batteries, PV panels and generator. The interface RT-lab is executed in Laptop 1 of Fig. 4.8. The EMS is developed in Python and implemented in a *RaspberyPi*4 which receives the measurement data and sends the control input via Modbus TCP/IP. An overview of the experimental platform is shown in the bottom half of Fig. 4.8. The HIL simulation results of the generated power, consumption and the battery energy for the two proposed energy management algorithms are illustrated in Fig. 4.9 for a period of 72 hour. During this experiment, nonlinear SDP algorithm uses a ϕ value of 1.09. At the end of the first day, the SDP method exhibits better Battery Availability Index than the rule-based method; however, in the second day, it fails in obtaining a superior index than the rule-based method. The situation is over ruled by the third day when the SDP implementation is able to show better performance. In general, the total generator operating cost (for generator fuel consumption) using the rule-based approach was *US*$3.5537, whereas the total cost for the generator usage under the SDP-based method was *US*$2.8493, representing a saving of 19%.

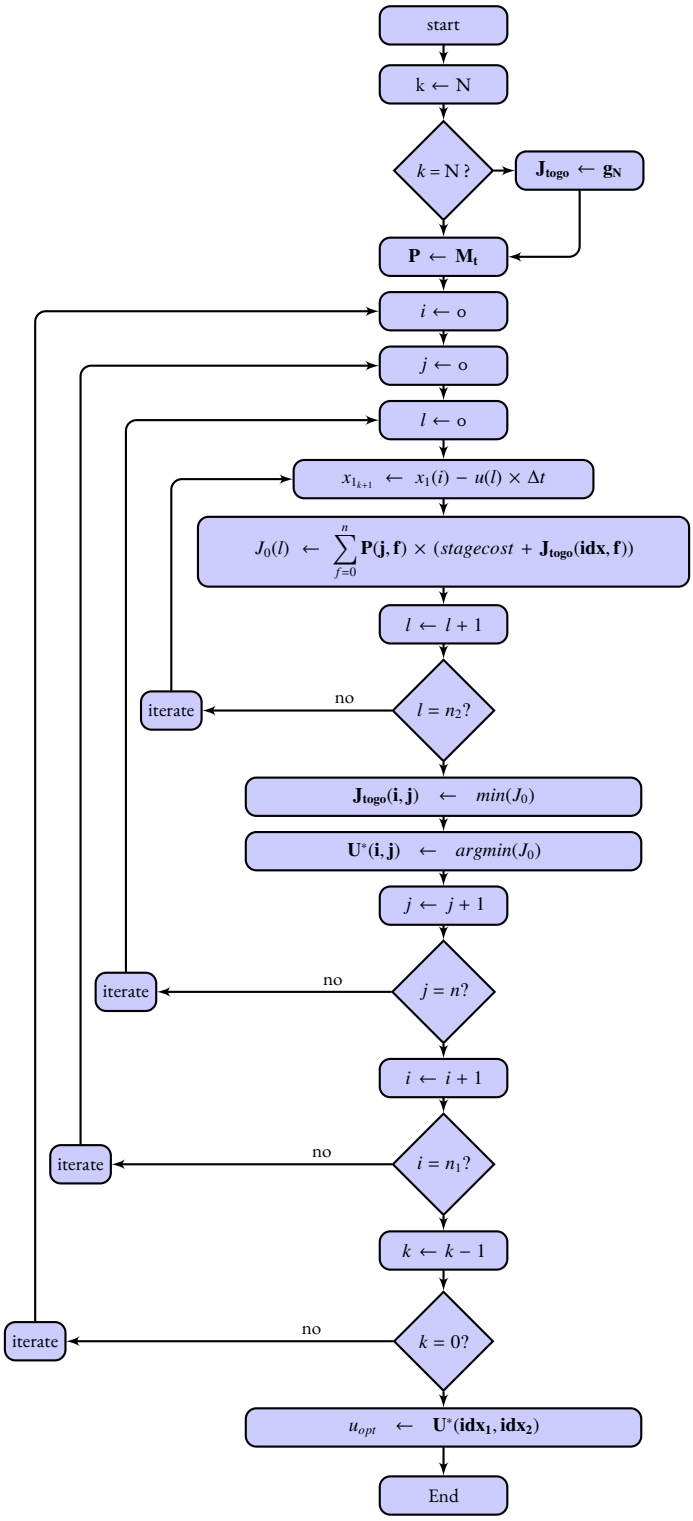

Figure 4.4: Flowchart diagram of the SDP algorithm. Copyright ©2020, IEEE.

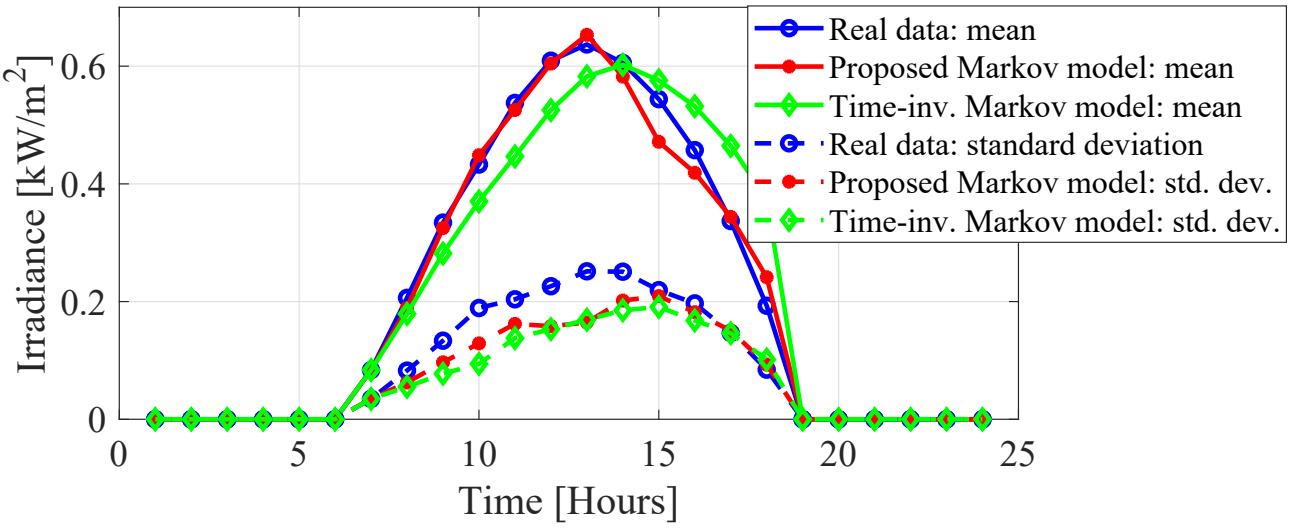

Figure 4.5: Comparison of hourly mean and standard deviation between proposed time-variant Markov model and the real data. Copyright ©2020, IEEE.

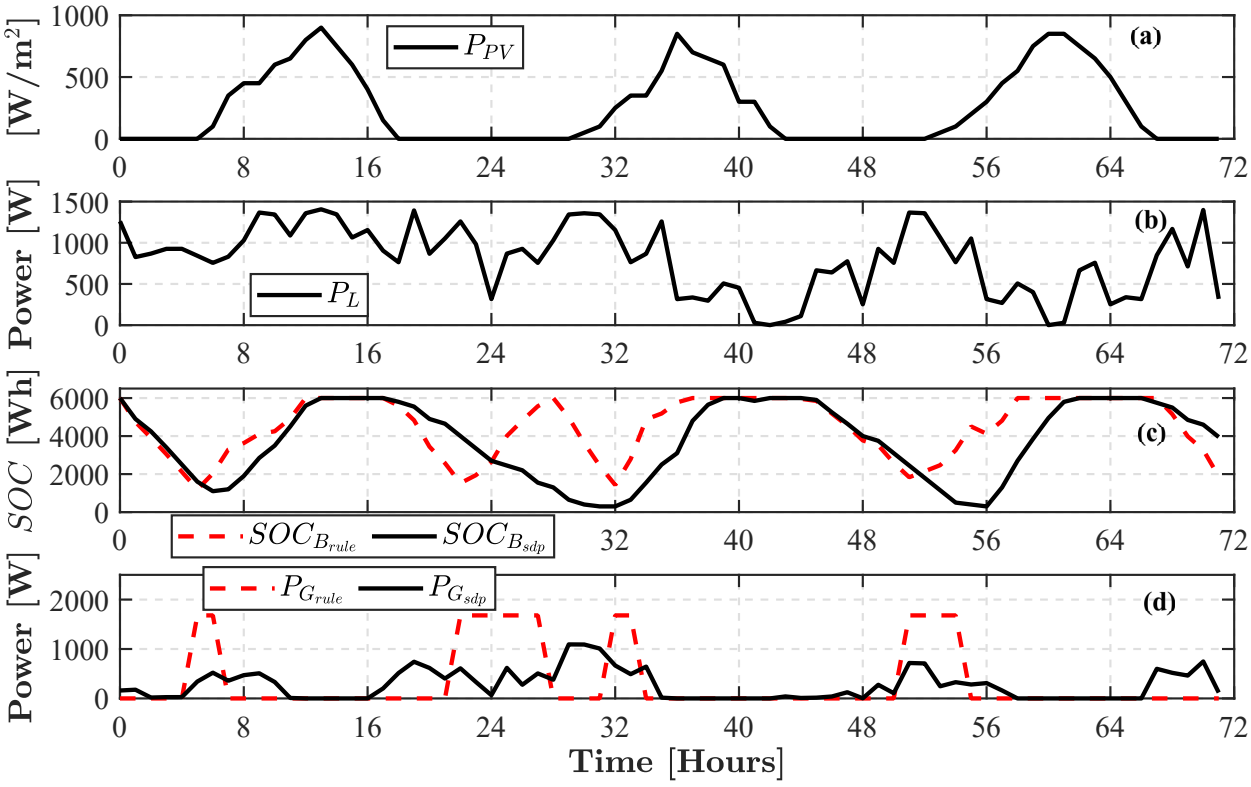

Figure 4.6: Simulation results for three consecutive days with good irradiance levels. (a) P_{PV} (PV available power), (b) P_L (load power), (c) battery SOC, and (d) P_G (fuel generator power). Copyright ©2020, IEEE.

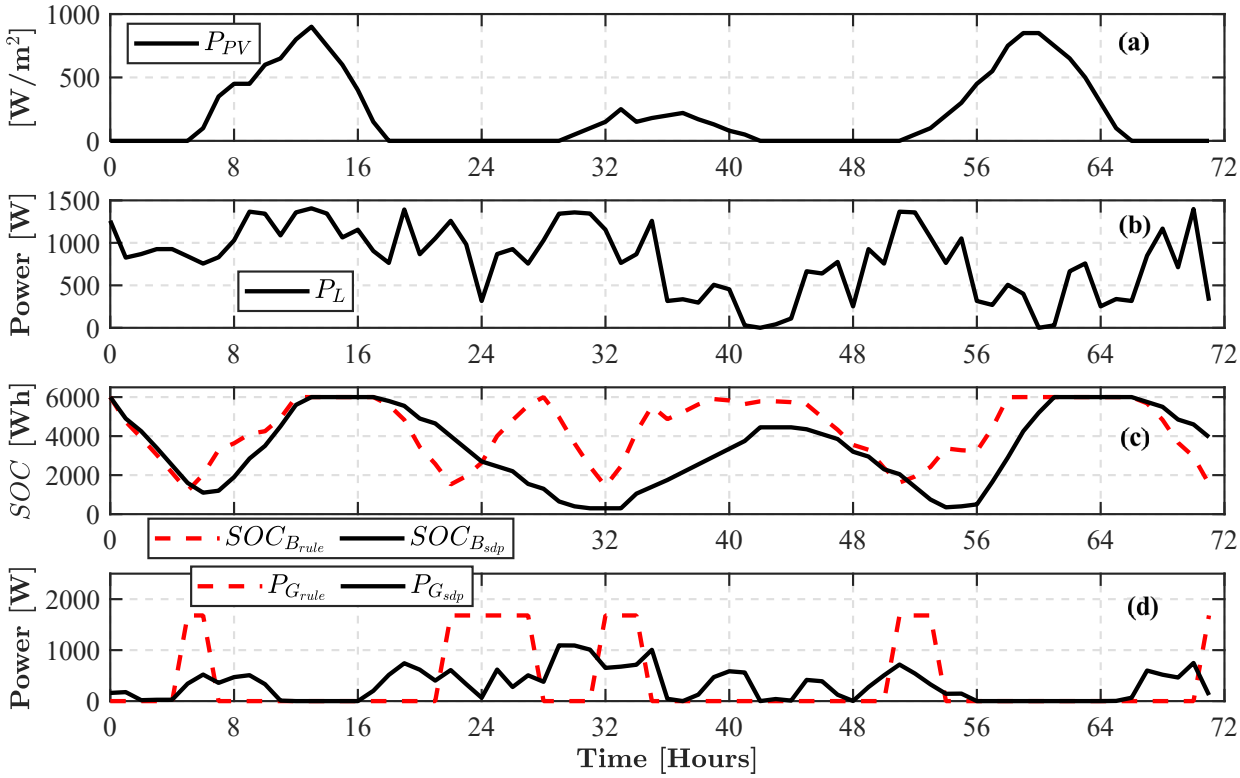

Figure 4.7: Simulation results for three consecutive days, assuming that the second day has a lower irradiance level. (a) P_{PV} (PV available power), (b) P_L (load power), (c) battery SOC, and (d) P_G (fuel generator power). Copyright ©2020, IEEE.

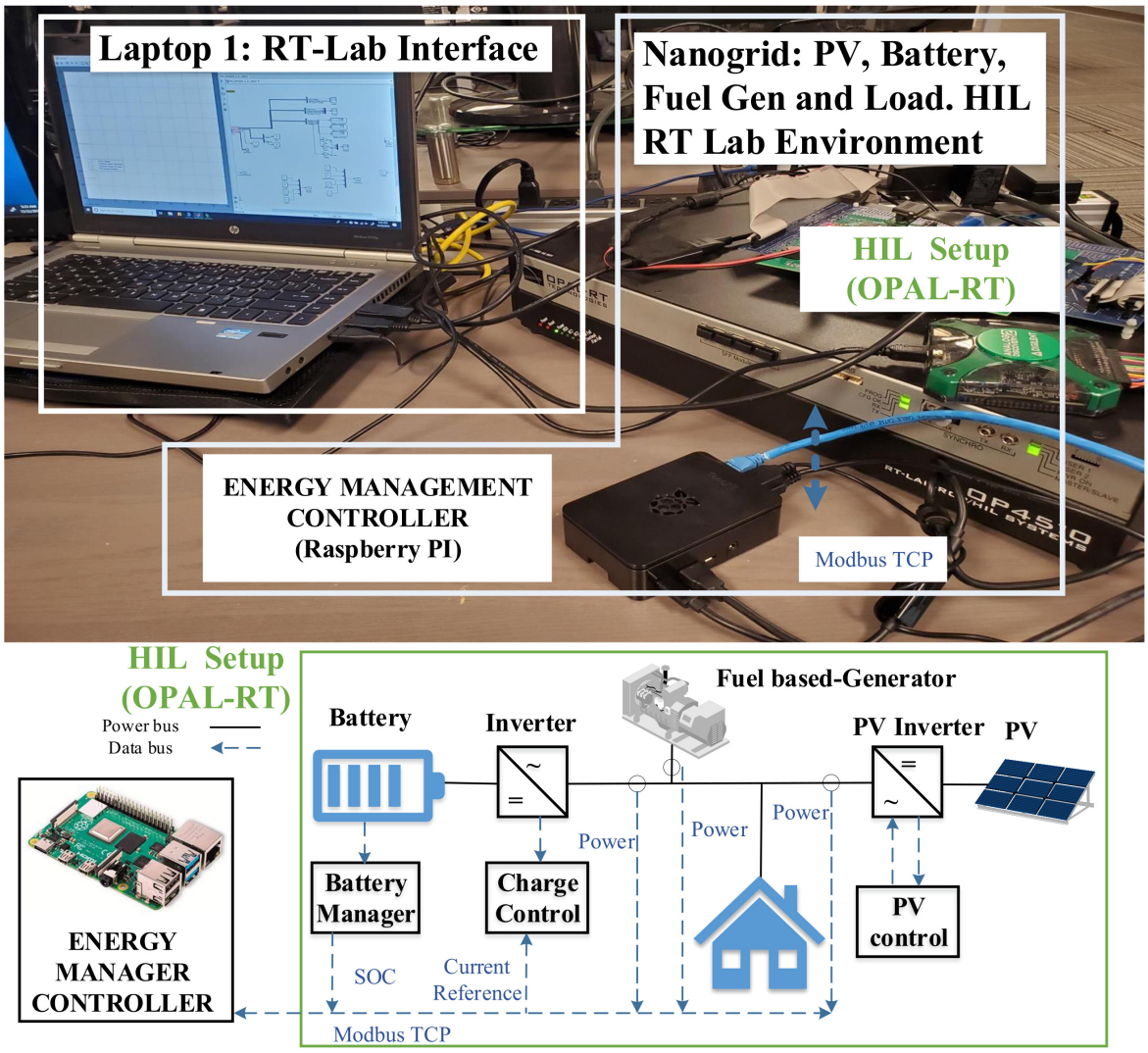

Figure 4.8: Setup for the real-time Hardware-in-the-Loop. Copyright ©2020, IEEE.

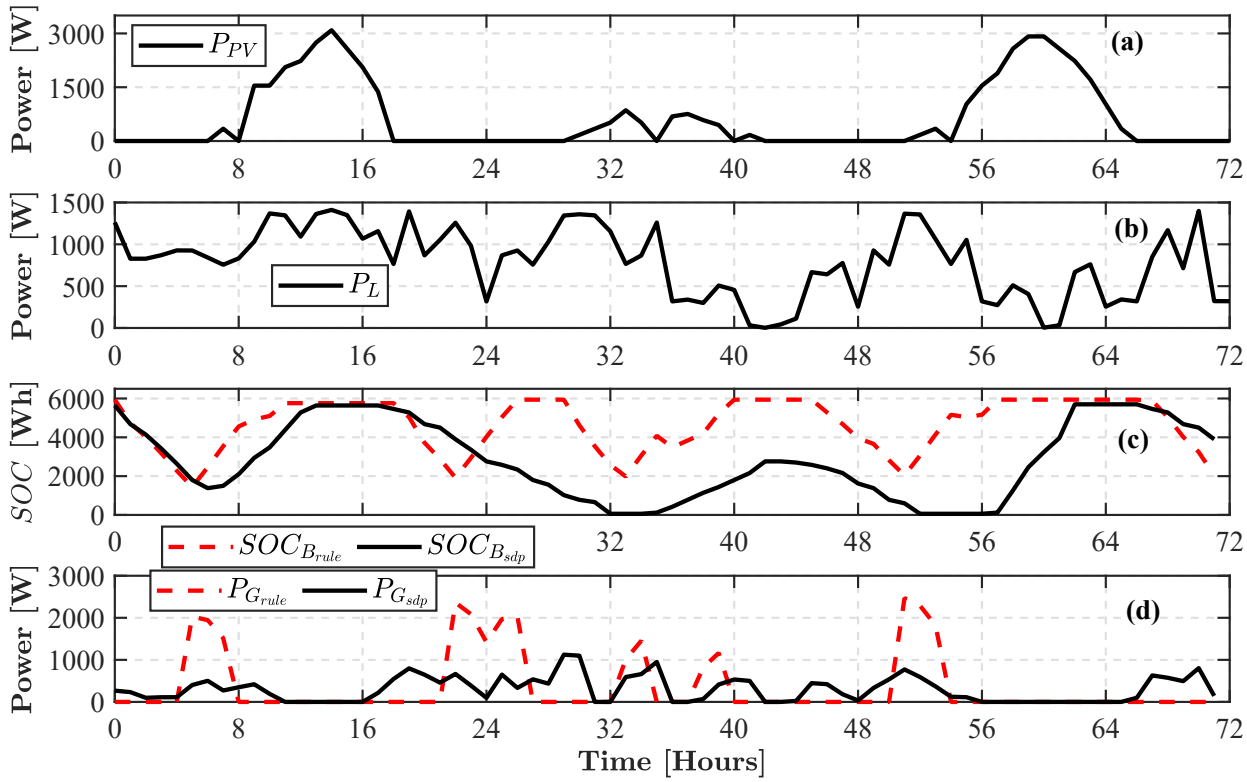

Figure 4.9: HIL results of 72 hours. (a) P_{PV} (PV available power), (b) P_L (load power), (c) battery SOC, and (d) P_G (fuel generator power). Copyright ©2020, IEEE.

Chapter 5

Conclusion and Future work

A study over the implementation of a nonlinear droop controller with virtual impedance in residential AC nanogrids was presented in chapter 1. This study allowed to understand the dynamic behavior of the system by developing a closed-loop model using time-varying phasor or dynamic phasor theory. The developed model was employed for the stability analysis using contraction theory. The analysis showed the role of the virtual impedance in the closed-loop control stability even if both systems share the same parameters and are perfectly synchronized. It also showed that during reactive power sharing, the use of a virtual impedance with a resistive behavior is sufficient for guaranteeing exponential convergence of any trajectory around the system equilibrium point. Experimental and simulation results demonstrated the efficacy of the proposed model, as well as the validation of the stability analysis. The mathematical tools developed in Chapter 1 can allow further analysis in the design of virtual impedance and nonlinear droop controllers for islanded nanogrid operation, where multiple ESS are employed to increase the system power output, as well as the system energy storage capacity.

Chapter 2 examined the power conversion process in a single phase residential battery storage system. It is demonstrated that the pulsating power transfer characteristics in these systems leads to a quadratic sinusoidal current waveform flowing through the Li-Ion batteries, where the fundamental frequency of the AC component of the battery current is twice the power grid frequency. By having this information, we have shown how to obtain an expression for the estimation of the AC battery impedance at this frequency. The implementation of the proposed methodology for online estimation of the battery impedance is described with the presented results supporting the accuracy and reliability of the proposed method. The proposed method can further allow the online assessment of the health degradation of Li-Ion battery impedance, and

hence constitutes the first step in the analysis of online SOH estimation of Li-Ion batteries when they are used in residential single phase applications.

Chapter 2 also presented the design of a feedback linearization-based control law for a synchronous buck-boost converter used in residential BSS. The challenges of the double grid frequency pulsating power in the dc side were studied and it was shown how the implemented control law could support the system efficiency by tracking the desired power transfer, while, at the same time tracking the dc-link reference. A comparison against a linear control law implementation was shown. The performance found for the FBL was superior than the one presented by linear control law. Implementation results further validated the system dynamic performance in a real-time application. Finally, the stability analysis of the converter led to a design constraint that can be used to correctly select the output capacitance value based on the output power demand while supporting system stability.

Two algorithms were devised in chapter 4 aiming at scheduling the battery charge and discharge in an NG supplied by both traditional and renewable sources while considering operational constraints to yield maximum financial and operational benefits. SDP was employed to achieve an optimal EM, in which a nonlinear optimization problem was formulated over a finite number of stages and on a rolling horizon basis. The use of a time-variant Markov model was also proposed in this paper. The simulation and HIL results confirmed that the stochastic EM strategy was able to effectively cope with the economical requirements much better than the rule-based approach in an autonomous mode. Furthermore, the stochastic approach could also cope with modeling and capturing uncertainties in PV generation. The SDP-based approach guaranteed the minimum operating cost by minimizing the fuel generator operating times during each cycle, and simultaneously improving the availability of battery in the next cycle by elevating its SOC at the end of each cycle.

5.1 Future research

Simulating multiple ESS connected in parallel for understanding the impact of linear and non-linear droop control schemes can be achieved by following the results and mathematical tools presented in chapter 2. Even more, the stability analysis proposed in chapter 2 could allow a proper design of a virtual impedance parameter without the need for iterations through extensive simulations. Further research could use the presented results to develop a closed control loop, including the inner current and voltage control loop for the power converter. The closed and open-loop tvp models derived in this work can be expanded to analyze the deviation

of multiple parameters in a residential nanogrids. Such approach could allow to develop mathematical tools to analyze the impact of failures in the power network, and not desired perturbations in the inverters control loop parameters.

Chapter 3 results has been presented in (Salazar, Berzoy, & Velni, 2019), (Salazar et al., 2017) and (Salazar et al., 2018). Prognosis of Li-Ion batteries used in residential ESS can be studied by using the proposed tools presented in this work. Feedback linearization controller used in this type of applications can be further studied to increase the robustness. The results and analysis presented in chapter 3 could implement a non-linear control law using feedback linearization for reducing the battery current ripple. Even thought the presented results showed no major ESS performance differences between no ripple reduction and ripple reduction control schemes, further analysis should be developed to establish a possible correlation with round trip efficiency and/or DC link capacitors' life expectancy.

Finally, the results and analysis presented in chapter 4 allowed the understanding of an energy management optimization approach assuming non-linearities in the battery charge/discharge dynamics. Such results were published in (Salazar et al., 2020). Further research could help to evaluate the performance of the proposed algorithm under a complete ESS scenario. Simultaneously, the stochastic Markov model proposed in this work could be improved to adapt itself based on real time measured data dynamically. The introduction of additional constraints such as load demand can also be investigated. The proposed stochastic DP framework can be used to evaluate different load demand forecasting models. These results also encourage exploring the implementation and further adaptation of the proposed framework to an ADP approach.

Bibliography

Abouloifa, A., & Giri, F. (2004). Nonlinear control of buck-boost AC/DC converters: output voltage regulation & power factor correction. *Proceedings of the 2004 American Control Conference*, *1*, 168–173 vol.1. https://doi.org/10.23919/ACC.2004.1383598

Administration, U. E. I. (2020). *Annual Energy Outlook 2020 with projections to 2050* (tech. rep.). https://www.eia.gov/outlooks/aeo/pdf/AEO2020%20Full%20Report.pdf

Akyurek, A. S., & Rosing, T. S. (2017). Optimal Distributed Nonlinear Battery Control. *IEEE Journal of Emerging and Selected Topics in Power Electronics*, *5*(3), 1045–1054. https://doi.org/10.1109/JESTPE.2016.2645480

Ardani, K., O'Shaughnessy, E., Fu, R., McClurg, C., Huneycutt, J., & Margolis, R. (2016). *Installed Cost-Benchmarksand Deployment Barriers for Residential Solar Photovoltaics with Energy Storage: Q1 2016* (tech. rep.).

Barnes, A. K., Balda, J. C., & Escobar-Mejía, A. (2015). A semi-markov model for control of energy storage in utility grids and microgrids with pv generation. *IEEE Transactions on Sustainable Energy*, *6*(2), 546–556. https://doi.org/10.1109/TSTE.2015.2393353

Batteries, H. O. F., Library, D. E., & Companies, T. M.-h. (2004). *Handbook of Batteries*. McGraw-Hill handbooks. https://doi.org/10.1016/0378-7753(86)80059-3

Belloni, A., Piroddi, L., & Prandini, M. (2016). A stochastic optimal control solution to the energy management of a microgrid with storage and renewables. *Proceedings of the American Control Conference*, *2016-July*, 2340–2345. https://doi.org/10.1109/ACC.2016.7525267

Benadero, L., Cristiano, R., Pagano, D. J., & Ponce, E. (2015). Nonlinear Analysis of Interconnected Power Converters: A Case Study. *IEEE Journal on Emerging and Selected Topics in Circuits and Systems*, *5*(3), 326–335. https://doi.org/10.1109/JETCAS.2015.2462017

Bertsekas, D. P. (2005). *Dynamic programming and optimal control* (Vol. 1). Athena scientific Belmont.

Berzoy, A., Salazar, A., Khalizheli, F., Restrepo, C., & Velni, J. M. (2019). Non-linear droop control of parallel split-phase inverters for residential nanogrids. *2019 IEEE Applied Power Electronics Conference and Exposition (APEC)*, 1150–1156. https://doi.org/10.1109/APEC.2019.8721932

Bhattacharya, A., Kharoufeh, J. P., & Zeng, B. (2018). Managing energy storage in microgrids: A multistage stochastic programming approach. *IEEE Transactions on Smart Grid*, *9*(1), 483–496. https://doi.org/10.1109/TSG.2016.2618621

Bidram, A., Member, S., & Davoudi, A. (2012). Hierarchical Structure ofMicrogrids Control System. *3*(4), 1963–1976. https://doi.org/10.1109/TSG.2012.2197425

Bidram, A., Nasirian, V., Davoudi, A., & Lewis, F. (2017). *Cooperative synchronization in distributed microgrid control*. https://doi.org/10.1007/978-3-319-50808-5

Callegaro, L., Ciobotaru, M., Pagano, D. J., & Fletcher, J. E. (2018). Feedback Linearization Control in Photovoltaic Module Integrated Converters. *IEEE Transactions on Power Electronics*, *PP*(100), 1–1. https://doi.org/10.1109/TPEL.2018.2872677

Chamola, V., & Sikdar, B. (2015). A Multistate Markov Model for Dimensioning Solar Powered Cellular Base Stations. *IEEE Transactions on Sustainable Energy*, *6*(4), 1650–1652. https://doi.org/10.1109/TSTE.2015.2454434

Chatterji, E., & Bazilian, M. D. (2020). Battery storage for resilient homes. *IEEE Access*, *8*, 184497–184511. https://doi.org/10.1109/ACCESS.2020.3029989

Cho, S. Y., Lee, I. O., Baek, J. I., & Moon, G. W. (2016). Battery Impedance Analysis Considering DC Component in Sinusoidal Ripple-Current Charging. *IEEE Transactions on Industrial Electronics*, *63*(3), 1561–1573. https://doi.org/10.1109/TIE.2015.2497661

Craparo, E., Karatas, M., & Singham, D. I. (2017). A robust optimization approach to hybrid microgrid operation using ensemble weather forecasts. *Applied Energy*, *201*(5), 135–147. https://doi.org/10.1016/j.apenergy.2017.05.068

Dawoud, S. M., Lin, X., & Okba, M. I. (2018). Hybrid renewable microgrid optimization techniques: A review. *Renewable and Sustainable Energy Reviews*, *82*(May 2017), 2039–2052. https://doi.org/10.1016/j.rser.2017.08.007

Donadee, J., & Ilić, M. D. (2014). Stochastic optimization of grid to vehicle frequency regulation capacity bids. *IEEE Transactions on Smart Grid*, *5*(2), 1061–1069. https://doi.org/10.1109/TSG.2013.2290971

Erickson, R., & Maksimovic, D. (2001). *Fundamental of power electronics*. https://doi.org/10.1007/b100747

Fadil, H. E., Giri, F., & Guerrero, J. M. (2012). Grid-connected of photovoltaic module using nonlinear control. *Proceedings - 2012 3rd IEEE International Symposium on Power Electronics for Distributed Generation Systems, PEDG 2012*, (1), 119–124. https://doi.org/10.1109/PEDG.2012.6253989

Fu., R., Remo, T., & Margolis, R. (2018). *2018 U.S. Utility-Scale Photovoltaics-Plus-Energy Storage System Costs Benchmark* (tech. rep.). National Laboratory of the U.S. Department of Energy (NREL). https://www.nrel.gov/docs/fy19osti/71714.pdf

Fujisawa, A. Y. K. S. T. N. (1989). Secondary battery.

Ginart, A., Salazar, A., & Liou, R. (2016). Transformerless Bidirectional Inverter for Residential Battery Storage Systems. *IEEE Green Technologies Conference*, *2016-April*, 18–23. https://doi.org/10.1109/GreenTech.2016.11

Guerrero, J. M., de Vicuna, L., Matas, J., Castilla, M., & Miret, J. (2005). Output impedance design of parallel-connected UPS inverters with wireless load-sharing control. *IEEE Trans. Ind. Electron.*, *52*(4), 1126–1135. https://doi.org/10.1109/TIE.2005.851634

Guerrero, J. M., Vasquez, J. C., Matas, J., De Vicuña, L. G., & Castilla, M. (2011). Hierarchical control of droop-controlled AC and DC microgrids - A general approach toward standardization. *IEEE Transactions on Industrial Electronics*, *58*(1), 158–172. https://doi.org/10.1109/TIE.2010.2066534

Hamzeh, M., Mokhtari, H., & Karimi, H. (2013). A decentralized self-adjusting control strategy for reactive power management in an islanded multi-bus MV microgrid. *Canadian Journal of Electrical and Computer Engineering*, *36*(1), 18–25. https://doi.org/10.1109/CJECE.2013.6544468

Howey, D. A., Mitcheson, P. D., Member, S., Yufit, V., Offer, G. J., & Brandon, N. P. (2014). Online measurement of battery impedance using motor controller excitation. *IEEE Transaction on Vehicular Technology*, *63*(6), 2557–2566. https://doi.org/10.1109/TVT.2013.2293597

Huang, W., & Qahouq, J. A. (2014). An online battery impedance measurement method using DC-DC power converter control. *IEEE Transactions on Industrial Electronics*, *61*(11), 5987–5995. https://doi.org/10.1109/TIE.2014.2311389

Jaber, M. A., & Massicotte, D. (2010). Fast method to detect specific frequencies in monitored signal. *Final Program and Abstract Book - 4th International Symposium on Communications, Control, and Signal Processing, ISCCSP 2010*. https://doi.org/10.1109/ISCCSP.2010.5463480

Khalil, H. K. (2015). *Nonlinear control*. Pearson New York.

Li, Y. W., & Kao, C. N. (2009). An accurate power control strategy for power-electronics-interfaced distributed generation units operating in a low-voltage multibus microgrid. *IEEE Transactions on Power Electronics*, *24*(12), 2977–2988. https://doi.org/10.1109/TPEL.2009.2022828

Liu, N., Yu, X., Fan, W., Hu, C., Rui, T., Chen, Q., & Zhang, J. (2018). Online energy sharing for nanogrid clusters: A lyapunov optimization approach. *IEEE Transactions on Smart Grid*, *9*(5), 4624–4636. https://doi.org/10.1109/TSG.2017.2665634

LOHMILLER, W., & SLOTINE, J.-J. E. (1998). On contraction analysis for non-linear systems. *Automatica*, *34*(6), 683–696. https://doi.org/https://doi.org/10.1016/S0005-1098(98)00019-3

Mackenzie, W. (2020). *U.S. energy storage monitor.2019 year in review executive summary* (tech. rep.). Wood Mackenzie Power & Renewables. https://energystorage.org/resources/industry-resources/us-energy-storage-monitor/

Mahmud, M. A., Hossain, M. J., Pota, H. R., & Roy, N. K. (2014). Nonlinear distributed controller design for maintaining power balance in Islanded microgrids. *IEEE Power and Energy Society General Meeting*, *2014-Octob*(October), 893–903. https://doi.org/10.1109/PESGM.2014.6939024

Mariani, V., & Vasca, F. (2013). Stability analysis of droop controlled inverters via dynamic phasors and contraction theory. *2013 European Control Conference (ECC)*, 1505–1510. https://doi.org/10.23919/ECC.2013.6669325

Matas, J., Castilla, M., d. Vicuña, L. G., Miret, J., & Vasquez, J. C. (2010). Virtual impedance loop for droop-controlled single-phase parallel inverters using a second-order general-integrator scheme. *IEEE Transactions on Power Electronics*, *25*(12), 2993–3002. https://doi.org/10.1109/TPEL.2010.2082003

Micea, M., & Ungurean, L. (2011). Online State-of-Health Assessment for Battery Management Systems. *IEEE Transactions on Instrumentation and Measurement*, *60*(6), 1997–2006. https://doi.org/10.1109/TIM.2011.2115630

Mingant, R., Bernard, J., & Sauvant-Moynot, V. (2016). Novel state-of-health diagnostic method for Li-ion battery in service. *Applied Energy*, *183*, 390–398. https://doi.org/10.1016/j.apenergy.2016.08.118

Monfared, M., Sanatkar, M., & Golestan, S. (2012). Direct active and reactive power control of single-phase grid-tie converters. *IET Power Electronics*, *5*(8), 1544. https://doi.org/10.1049/iet-pel.2012.0131

Moslemi, R., & Mohammadpour, J. (2015). Accurate reactive power control of autonomous microgrids using an adaptive virtual inductance loop. *Electric Power Systems Research*, *129*, 142–149. https://doi.org/https://doi.org/10.1016/j.epsr.2015.08.001

Nordman, B., & Christensen, K. (2013). Local power distribution with nanogrids. *2013 International Green Computing Conference Proceedings*, 1–8. https://doi.org/10.1109/IGCC.2013.6604464

Nordman, B., Christensen, K., & Meier, A. (2012). Think globally, distribute power locally: The promise of nanogrids. *Computer*, *45*(9), 89–91. https://doi.org/10.1109/MC.2012.323

(NREL)., N. R. E. L. (n.d.). Monthly data files & reports. $http://rredc.nrel.gov/solar/new_data/confrrm/ec/$

Omar, N., Daowd, M., Van den Bossche, P., Hegazy, O., Smekens, J., Coosemans, T., & Van Mierlo, J. (2012). Rechargeable energy storage systems for plug-in hybrid electric vehicles—assessment of electrical characteristics. *5*, 2952–2988.

O'Neill-Carrillo, E., & Irizarry-Rivera, A. (2019). How to harden puerto rico's grid against hurricanes. *IEEE Spectrum*, *56*(11), 42–48. https://doi.org/10.1109/MSPEC.2019.8889972

P. Poggi, M. M., G. Notton, & Louche, A. (2000). Stochastic study of hourly total solar radiation in Corsica using a Markov model. *International journal of climatology*, *20*(14), 1843–1860.

Padhi, A. K. (1997). Phospho-olivines as Positive-Electrode Materials for Rechargeable Lithium Batteries. *Journal of The Electrochemical Society*, *144*(4), 1188. https://doi.org/10.1149/1.1837571

Pappas, S. S., Ekonomou, L., Karamousantas, D. C., Chatzarakis, G. E., Katsikas, S. K., & Liatsis, P. (2008). Electricity demand loads modeling using autoregressive moving average (ARMA) models. *Energy*, *33*(9), 1353–1360.

Peng, Y., Shuai, Z., Liu, X., Li, Z., Guerrero, J. M., & Shen, Z. J. (2020). Modeling and stability analysis of inverter-based microgrid under harmonic conditions. *IEEE Transactions on Smart Grid*, *11*(2), 1330–1342. https://doi.org/10.1109/TSG.2019.2936041

Perez, F., Iovine, A., Damm, G., & Ribeiro, P. (2018). DC microgrid voltage stability by dynamic feedback linearization. *Proceedings of the IEEE International Conference on Industrial Technology*, *2018-Febru*, 129–134. https://doi.org/10.1109/ICIT.2018.8352164

Pistoia, G. (2013). *Lithium-Ion Batteries: Advances and Applications*.

Puterman, M. L. (2014). *Markov decision processes: Discrete stochastic dynamic programming*. John Wiley & Sons.

Qahouq, J. A. (2016). Online battery impedance spectrum measurement method. *Conference Proceedings - IEEE Applied Power Electronics Conference and Exposition - APEC*, *2016-May*, 3611–3615. https://doi.org/10.1109/APEC.2016.7468388

Rafiee Sandgani, M., & Sirouspour, S. (2018). Energy management in a network of grid-connected microgrids/nanogrids using compromise programming. *IEEE Transactions on Smart Grid*, *9*(3), 2180–2191. https://doi.org/10.1109/TSG.2016.2608281

Restrepo, C., Salazar, A., Schweizer, H., & Ginart, A. (2015). Residential battery storage: Is the timing right? *IEEE Electrification Magazine*, *3*(3), 14–21. https://doi.org/10.1109/MELE.2015.2447951

Salazar, A., Berzoy, A., Mohammadpour Velni, J., & Song, W. (2019). Optimum energy management of islanded nanogrids through nonlinear stochastic dynamic programming. *2019 IEEE Industry Applications Society Annual Meeting (IAS)*, 1–8.

Salazar, A., Berzoy, A., Song, W., & Velni, J. M. (2020). Energy management of islanded nanogrids through nonlinear optimization using stochastic dynamic programming. *IEEE Transactions on Industry Applications*, *56*(3), 2129–2137. https://doi.org/10.1109/TIA.2020.2980731

Salazar, A., Berzoy, A., & Velni, J. M. (2019). Nonlinear control design for bidirectional synchronous buck-boost converters used in residential battery storage systems. *2019 IEEE Energy Conversion Congress and Exposition (ECCE)*, 2485–2490. https://doi.org/10.1109/ECCE.2019.8912221

Salazar, A., Restrepo, C., Gao, Y., Velni, J. M., & Ginart, A. (2017). An online lifepo4 battery impedance estimation method for grid-tied residential energy storage systems. *2017 IEEE Energy Conversion Congress and Exposition (ECCE)*, 980–986. https://doi.org/10.1109/ECCE.2017.8095892

Salazar, A., Ginart, A., & Mohammadpour-Velni, J. (2018). Battery storage. In A. Ginart (Ed.), *Fault diagnosis for robust inverter power drives* (pp. 253–270). Institution of Engineering; Technology. https://doi.org/10.1049/PBPO120E_ch7

Schlasza, C., Ostertag, P., Chrenko, D., Kriesten, R., & Bouquain, D. (2014). Review on the aging mechanisms in Li-ion batteries for electric vehicles based on the FMEA method. *2014 IEEE Transportation Electrification Conference and Expo (ITEC)*, 1–6. https://doi.org/10.1109/ITEC.2014.6861811

Sheng, S., Li, P., Tsu, C., & Lehman, B. (2015). Optimal power flow management in a photovoltaic nanogrid with batteries. *2015 IEEE Energy Conversion Congress and Exposition (ECCE)*, 4222–4228. https://doi.org/10.1109/ECCE.2015.7310256

Shuai, H., Fang, J., Ai, X., Tang, Y., Wen, J., & He, H. (2018). Stochastic optimization of economic dispatch for microgrid based on approximate dynamic programming. *IEEE Transactions on Smart Grid*, *3053*(100), 1–13. https://doi.org/10.1109/TSG.2018.2798039

Simpson-Porco, J. W., Dorfler, F., & Bullo, F. (2013). Synchronization and power sharing for droop-controlled inverters in islanded microgrids. *Automatica*, *49*(9), 2603–2611. https://doi.org/10.1016/j.automatica.2013.05.018

Simpson-Porco, J. W., Dörfler, F., & Bullo, F. (2017). Voltage Stabilization in Microgrids via Quadratic Droop Control. *IEEE Transactions on Automatic Control*, *62*(3), 1239–1253. https://doi.org/10.1109/TAC.2016.2585094

Solsona, J. A., Jorge, S. G., & Busada, C. A. (2015). Nonlinear Control of a Buck Converter Which Feeds a Constant Power Load. *IEEE Transactions on Power Electronics*, *30*(12), 7193–7201. https://doi.org/10.1109/TPEL.2015.2392371

Sood, V. K. (2020). *Nanogrids: Good practices and challenges in the projects in colombia*. https://doi.org/10.1049/PBPO160E_ch16

Stroe, D. I., Swierczynski, M., Stan, A. I., Knap, V., Teodorescu, R., & Andreasen, S. J. (2014). Diagnosis of lithium-ion batteries state-of-health based on electrochemical impedance spectroscopy technique. *2014 IEEE Energy Conversion Congress and Exposition (ECCE)*, 4576–4582. https://doi.org/10.1109/ECCE.2014.6954027

Stroe, D. I., Swierczynski, M., Stan, a. I., Knap, V., Teodorescu, R., & Andreasen, S. J. (2014). Diagnosis of lithium-ion batteries state-of-health based on electrochemical impedance spectroscopy technique. *Energy Conversion Congress and Exposition (ECCE), 2014 IEEE*, 4576–4582. https://doi.org/10.1109/ECCE.2014.6954027

Świerczyński, M., Stroe, D. I., Stan, A. I., Teodorescu, R., & Sauer, D. U. (2014). Selection and performance-degradation. *IEEE Transactions on Sustainable Energy*, *5*(1), 90–101. https://doi.org/10.1109/TSTE.2013.2273989

Tang, X., Mao, X., Lin, J., & Koch, B. (2011). Li-ion battery parameter estimation for state of charge. *American Control Conference (ACC), 2011*, 941–946. https://doi.org/10.1109/ACC.2011.5990963

Thackeray, M. M., David, W. I., Bruce, P. G., & Goodenough, J. B. (1983). Lithium insertion into manganese spinels. *Materials Research Bulletin*, *18*(4), 461–472. https://doi.org/10.1016/0025-5408(83)90138-1

Venkatasubramanian, V. (1994). Tools for dynamic analysis of the general large power system using time-varying phasors. *International Journal of Electrical Power '|&" Energy Systems*, *16*(6), 365–376. https://doi.org/https://doi.org/10.1016/0142-0615(94)90023-X

Wakihara, M., Yamamoto, O., & Wakihara, M; Yamamoto, O. (1998). *Lithium Ion Batteries Fundamentals and Performance*. Wiley. https://doi.org/10.1177/019262337300100402

Wang, Y. X., Qin, F. F., & Kim, Y. B. (2014). Bidirectional DC-DC converter design and implementation for lithium-ion battery application. *Asia-Pacific Power and Energy Engineering Conference, APPEEC*, *2015-March*(March), 1–5. https://doi.org/10.1109/APPEEC.2014.7066140

Wei, Q., Liu, D., Lewis, F. L., Liu, Y., & Zhang, J. (2017). Mixed iterative adaptive dynamic programming for optimal battery energy control in smart residential microgrids. *IEEE Transactions on Industrial Electronics*, *64*(5), 4110–4120. https://doi.org/10.1109/TIE.2017.2650872

Werth, A., Kitamura, N., & Tanaka, K. (2015). Conceptual study for open energy systems: Distributed energy network using interconnected DC nanogrids. *IEEE Transactions on Smart Grid*, *6*(4), 1621–1630.

Wu, X., Hu, X., Moura, S., Yin, X., & Pickert, V. (2016). Stochastic control of smart home energy management with plug-in electric vehicle battery energy storage and photovoltaic array. *Journal of Power Sources*, *333*(October), 203–212. https://doi.org/10.1016/j.jpowsour.2016.09.157

Wu, X., Hu, X., Yin, X., & Moura, S. J. (2018). Stochastic optimal energy management of smart home with PEV energy storage. *IEEE Transactions on Smart Grid*, *9*(3), 2065–2075. https://doi.org/10.1109/TSG.2016.2606442

Zheng, H., & Shuai, D. (2012). Nonlinear control of boost converter by state feedback exact linearization. *Proceedings of the 2012 24th Chinese Control and Decision Conference, CCDC 2012*, 3502–3506. https://doi.org/10.1109/CCDC.2012.6244559

Zhong, Q. (2013). Robust Droop Controller for Accurate Proportional Load Sharing Among Inverters Operated in Parallel. *IEEE Transactions on Industrial Electronics*, *60*(4), 1281–1290. https://doi.org/10.1109/TIE.2011.2146221

Zhong, Q.-C., & Tomas, H. (n.d.). *Control of Power Inverters in Renewable Energy and Smart Grid Integration in Renewable Energy*.

Nomenclature

Chapter 2

α, β, a, b Coefficients

$\bar{\omega}$ Angular frequency reference at no load

$\bar{U}$ Output voltage reference at no load

$\boldsymbol{\zeta}$, $\boldsymbol{x}$ State space vector

$\boldsymbol{\Omega}$, $\boldsymbol{E}$, Ψ, Υ, Λ, Γ Functions from $\mathbb{R}$ onto $\mathbb{R}$

δ Phase difference between two power sources

δ_y Phase of sinusoidal signal

$\hat{f}$, $\hat{g}$, f Function from $\mathbb{R}^n$ onto $\mathbb{R}^n$

$\hat{y}(t)$ Time varying phasor of $y(t)$

$\omega(t)$ Instantaneous angular frequency

ω_o Nominal angular frequency

$\theta(t)$ Instantaneous phase shift between signals

Υ Function from $\mathbb{R}^2$ onto $\mathbb{R}$

ζ, x State-space variable

G_P Non-linear droop gain

L Inductance

m Active power droop gain

n Reactive power droop gain

P Average active power

$p(t)$ Instantaneous active power

Q Average reactive power

$q(t)$ Instantaneous reactive power

R Resistance

S Average complex power

$s(t)$ Instantaneous complex power

X Reactance

$Y(t)$ Instantaneous RMS of signal $y(t)$

$y(t)$ Instantaneous time varying signal with all harmonics content, transient and steady state. e.g. $u(t)$ and $i(t)$

Z Impedance

Chapter 3

f, g Function from $\mathbb{R}^n$ onto $\mathbb{R}^n$

$\boldsymbol{x}, \boldsymbol{\zeta}, \boldsymbol{z}$ State space vector

η Efficiency

ω Angular frequency

ω_o Nominal power grid angular frequency

a, b Parameter

C Capacitance

F_s Sampling frequency

I Frequency content of current signal

i Time-varying current signal

I_{DC} DC component of current

I_{RMS} RMS Current value

L Inductance

p Time-varying power signal

$R\,r$ Resistance

s complex number frequency parameter

SOC State of Charge

SOH State of Health

V Frequency content of voltage signal

v Time-varying voltage signal

V_{RMS} RMS Voltage value

x, y General difference equations

Z Impedance

Chapter 4

α, ϕ, Energy Storage capacity

$\boldsymbol{E}$ Expected value function

$\boldsymbol{x}$ State space vector

A Area function

E Discrete energy function

P Discrete Power function

SOC State of Charge